PROBING THE PHOTOCHEMISTRY OF RHODOPSIN THROUGH POPULATION DYNAMICS SIMULATIONS

Xuchun Yang

A Dissertation

Submitted to the Graduate College of Bowling Green
State University in partial fulfillment of
the requirements for the degree of

DOCTOR OF PHILOSOPHY

August 2019

Committee:

Massimo Olivucci, Advisor

Andrew Gregory
Graduate Faculty Representative

Hong Lu

Alexey Zayak

ABSTRACT

Massimo Olivucci, Advisor

The primary event in vision is induced by the ultrafast photoisomerization of rhodopsin, the dim-light visual pigment of vertebrates. While spectroscopic and theoretical studies have identified certain vibrationally coherent atomic motions to promote the rhodopsin photoisomerization, how exactly and to what degree such coherence is biologically related with its isomerizing efficiency (i.e. the photoisomerization quantum yield) remains unknown. In fact, in the past, the computational cost limited the simulation of the rhodopsin photoisomerization dynamics, which could be carried out only for a single molecule or a small set of molecules, therefore lacking the necessary statistical description of a molecular population motion.

In this Dissertation I apply a hybrid quantum mechanics/molecular mechanics (QM/MM) models of bovine rhodopsin, the verterbrate visual pigment, to tackle the basic issues mentioned above. Accordingly, my work has been developing along three different lines comprising the development, testing and application of new tools for population dynamics simulation: (I) Development of a suitable protocol to investigate the excited state population dynamics of rhodopsins at room temperature. (II) A correlation between the phase of a hydrogen-out-of-plane (HOOP) motion at the decay point and the outcome of the rhodopsin photoisomerization. (III) A population "splitting" mechanism adopted by the protein to maximize its quantum yield and, therefore, light sensitivity.

In conclusion, my Dissertation reports, for the first time, a connection between the initial coherent motion of a population of rhodopsin molecules and the quantum efficiency of their isomerization. The photoisomerization efficiency is ultimately determined by the way in which the degree of coherence of the excited state population motion is modulated by the protein sequence and conformation.

ACKNOWLEDGMENTS

I would like to thank:

Prof. Massimo Olivucci. This work would not exist without his guidance and patience. I am appreciating to have him as my academic advisor, who not only taught me a lot about photochemical science but the way of being a motivated researcher. I am grateful for everything that I have learned from him.

Prof. H. Peter Lu, Prof. Alexey T. Zayak and Prof. Andrew J. Gregory, for their time and help as my committee members.

My former and current lab mates in BGSU and Siena for their friendship and support. In particular, Dr. Hoi Ling Luk, who trained me about computational chemistry during my early stage of PhD study. Dr. Alessio Valentini, you are awesome that helped me solving all kinds of technical problems! Dr. Madushanka Sugath, Dr. Samer Gozem, Dr. Yoelvis Orozoco Gonzalez, Dr. Samira Gholami, Alejandro Gonzalez, Dr. Luca De Vicoand and Laura Pedraza González for their great friendship.

Our collaborators, in particular Dr. Roland Lindh, Dr. Nicolas Ferré, Dr, Alexander Granovsky, Dr. Christoph Schnedermann and Dr. Ignacio Fernández Galván, who provided much advice and help towards my PhD projects.

My friends, Zhang Peng, Xu Peng, Yang Jiawen, Ma Chonghuai and Wang Penghao, for encouraging me to get through all difficult times.

TABLE OF CONTENTS

Page

LIST OF FIGURES

Figure Page

LIST OF TABLES

CHAPTER I. INTRODUCTION

Rhodoposins are membrane proteins that are capable of sensing and responding to light to achieve various biological functions[1]. Rhodopsins found in microorganisms (termed type I, microbial rhodopsin) are employed, for instance, in ion-channeling or ion-pumping activities while in vertebrates and invertebrates, rhodopsins (termed type II, animal rhodopsin) typically display functions in visual light-sensing or maintenance of the circadian clock[2,3]. Despite various biological functions and primary structures, both type I and II rhodopsins are found to present a common architecture where the protein pocket is formed by seven interconnected α-helices and hosts a retinal protonated Schiff base (rPSB) chromophore[2,4]. In both type of rhodopsins, the ability of transducing light energy is primarily induced by the photoisomerization of the rPSB chromophore at one of its C=C double bond[5]. A molecular level mechanistic interpretation of such photoisomerization of rhodopsins, especially of vertebrate visual rhodopsins, is critical in the biological and medical fields due to their fundamental role in vision.

Due to availability of its x-ray crystallographic structure, bovine rhodopsin (Rh) has been the subject of the majority of studies reported on the biological function of vertebrate visual rhodopsins[6]. It is found in the outer segment of cattle rod visual cells and is in charge of dim-light vision. As shown in Figure 1.1a, Rh features a 11-*cis* rPSB chromophore (rPBS11) bound to the pocket of opsin through a lysine residue (Lys296) belonging to the 7th helix[7]. Absorption of a photon induces the photoisomerization of the $C_{11}=C_{12}$ double bond to its all-*trans* isomer (rPSBAT) to produce the first spectroscopically detectable, but not isolable, intermediate photorhodopsin (photoRh)[8]. The photoRh formed after the photoisomerization converts to the first isolable intermediate bathorodopsin (bathoRh) through thermal relaxation on a picosecond timescale. The photon energy stored in bathRh promotes subsequent conformational changes in the opsin, ultimately producing metarhodopsin II (Meta II), which is the photocycle intermediate that activates the G protein transducing (Figure 1.1b)[9].

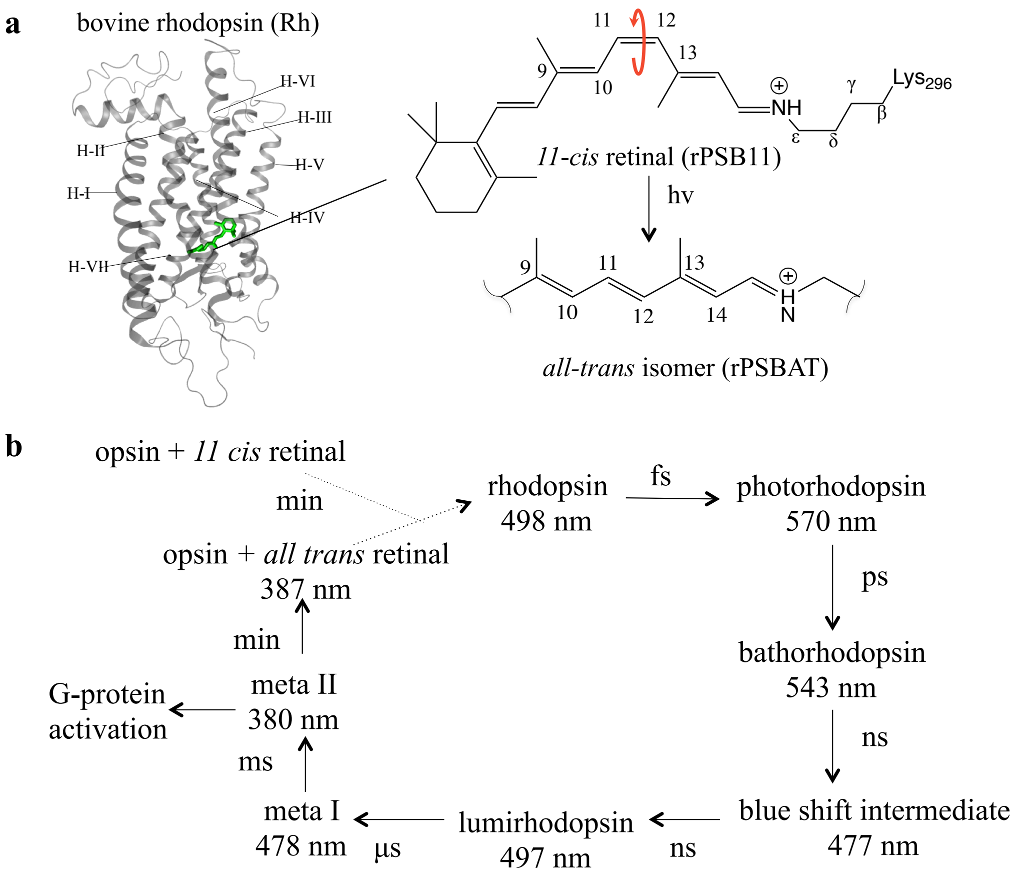

Figure 1.1 Structure, photoisomerization and photocycle of Rh. **a.** Structure of Rh molecule. The transmembrane protein structure (gray and ribbon representation) featuring seven α-helices (H-I to H-VII) hosts the rPSB11 chromophore (green and licorice representation) that undergoes a *cis* to *trans* photoisomerization upon light absorption. Such isomerization produces rPSBAT chromophore. **b.** The light absorption maximum and formation timescale of Rh photocycle intermediates.

The Rh photocycle steps leading to the formation of bathoRh is defined as the "primary event in vision"[10] and the nature of such photochemical process has been studied extensively. Past experimental evidence has shown that the photoisomerization in Rh occurs on an sub-200 fs timescale[11] with high (0.67) photoproduct (rPSBAT) formation quantum yield[12] and low (1.2×10^{-5}) fluorescence quantum yield[13] contributing to the pigment extreme light sensitivity. Spectroscopic studies have shown that such reaction is not only ultrafast but also vibrationally coherent[14,15]. Three vibrational modes have been identified to be involved in the photoisomereization of Rh[14]. These are the counterclockwise torsional twisting motion of the isomerizing C_{10}-C_{11}=C_{12}-C_{13} bond (α), the hydrogen wagging motion of the H_{11}-C_{11}=C_{12}-H_{12} hydrogens (β) and the stretching motion along the conjugated backbone (i.e., the skeletal single/double bond length alternation, BLA)[16] (Figure 1.2a). For convenience, we introduce a "hydrogen-out-of-plane" (HOOP, δ_{op}) coordinate, which is a linear combination of α and β as defined in Figure 1.2b, that has been used in previous studies[17,18]. The photoisomerization of Rh is described as the non-adiabatic transition of the rPSB11 decaying from the first excited state (S_1) to the ground state (S_0) via a conical intersection (CI) (Figure 1.2c). At CI the excited state molecule, which features a ca. -90 degree twisted C_{11}=C_{12} bond, would either proceed along the counterclockwise twisting described by the α mode to form the rPSBAT photoproduct or invert the direction of such twisting motion back to the rPSB11 reactant[19]. Notice that the thermal isomerization transition state (TS) is high in energy with respect to the S_0 dark state structure and the corresponding energy barrier (ΔE_a^T) modulates the rate of thermal isomerization. It has been reported that such thermal process competes with the photoisomerization process thus lowering the visual sensitivity by creating a background noise also called "dark noise"[20].

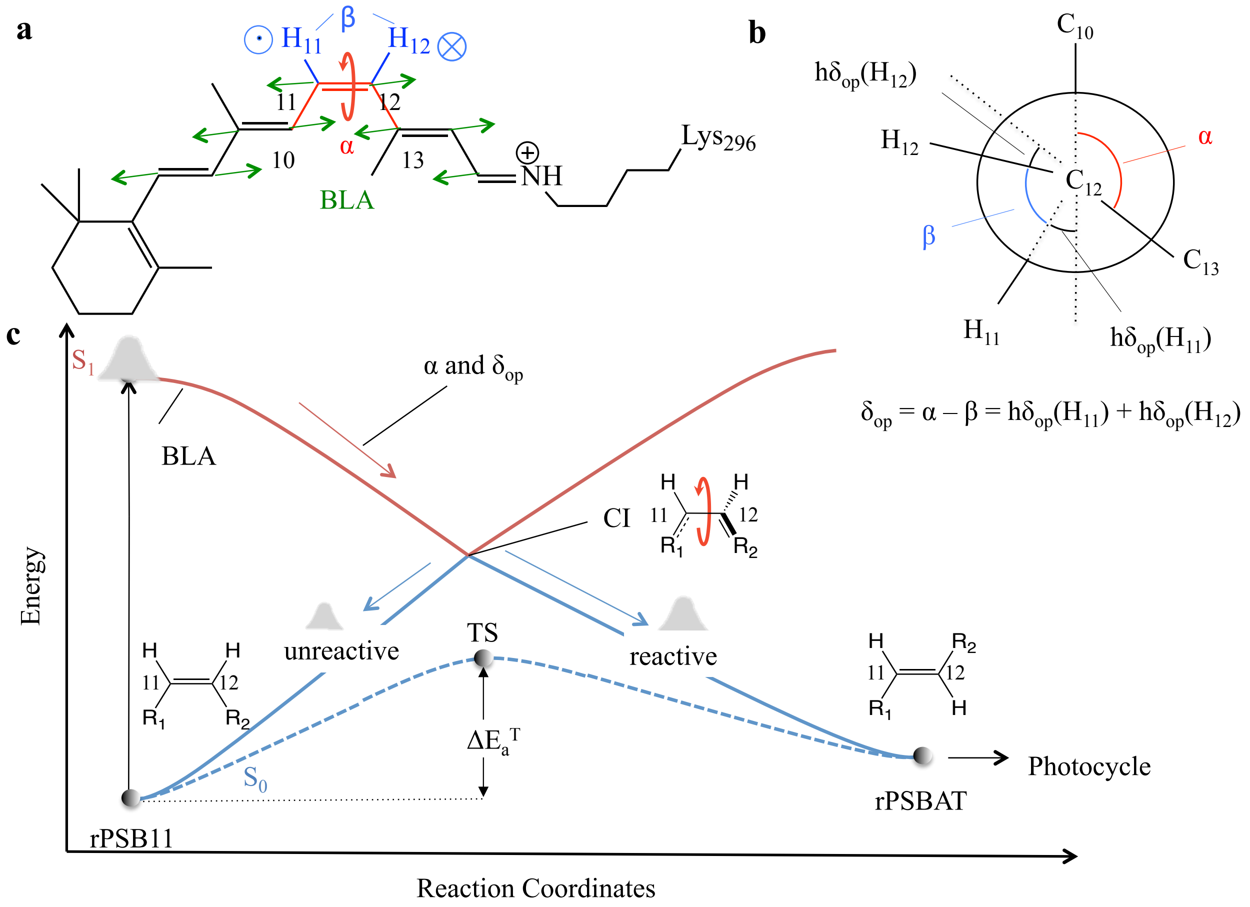

Figure 1.2 The Rh photoisomerization. **a**. The photoisomerization coordinate is composed of α (in red), β (in blue) and BLA (in green). **b.** Definition of δ_{op} coordinates. **c.** Schematic representation of the evolution of the Rh population on the S_1 and then S_0 potential energy surfaces.

Nature has developed Rh to be extremely sensitive to light, and thus enables vision on dim-light conditions. Such extreme light sensitivity is achieved primarily by the efficiency of the photoisomerization of rPSB11. To enhance such high efficiency, it is important to minimize all possible competing/background processes. In other words, the thermal isomerization activation energy ΔE_a^T must be maximized to prevent the S_0 thermal isomerization and the photoisomerization timescale must be minimized to reduce the possibility of fluorescence, which is usually observed to take place on the pico to nanosecond time scale[21]. Meanwhile it is critical to maximize the photoisomerization quantum yield to produce sufficient bathoRh to proceed the photocycle.

Over past few decades, theoretical efforts have provided a mechanistic interpretation of how the optimal properties described above can be achieved. The S_0 TS structure whose energy determines ΔE_a^T and, as described in a recent report[22], the Rh thermal stability can be computed by searching for a TS located along the S_0 potentail energy surface (PES). In the same report the author provided a correlation between the maximum absorption wavelength ($\lambda^a{}_{max}$) and the ΔE_a^T by indicating the same type of charge-transfer electronic structure is shared by the S_0 TS structure and the vertical excited structure.

The development of computer hardware and software in the early 2000s allowed 200 fs semi-classical trajectory simulation of Rh whose results provided the basis for proposing a two-state three-mode mechanism for the Rh photoisomerization[16]. In such mechanism, the rPSB11 is promoted to vertical excited region of its S_1 PES by the absorpted photon energy. The S_1 presents a ionic (charge-transfer) electronic configuration. As shown in Figure 1.3, the positive charge is spread towards the β-ionone moiety. Then the rPSB11 undergoes a counterclockwise twisting about its $C_{11}=C_{12}$ double bond and transfers the S_1 population to S_0 at CI[23]. The skeletal bond stretching relaxation motion BLA is promoted by the charge-transfer S_1 electron structure and dominates the early stage of the photoisomerization. Then the δ_{op} and α motions are active, transferring the excited state molecule towards CI on sub-100 fs timescale[17,24–27]. The time evolution of BLA, α and δ_{op} motion is obtained with a single Franck Condon (FC) trajectory (i.e., releasing the molecule from the vertical excited region with zero initial velocity) and plotted in Figure 1.3.

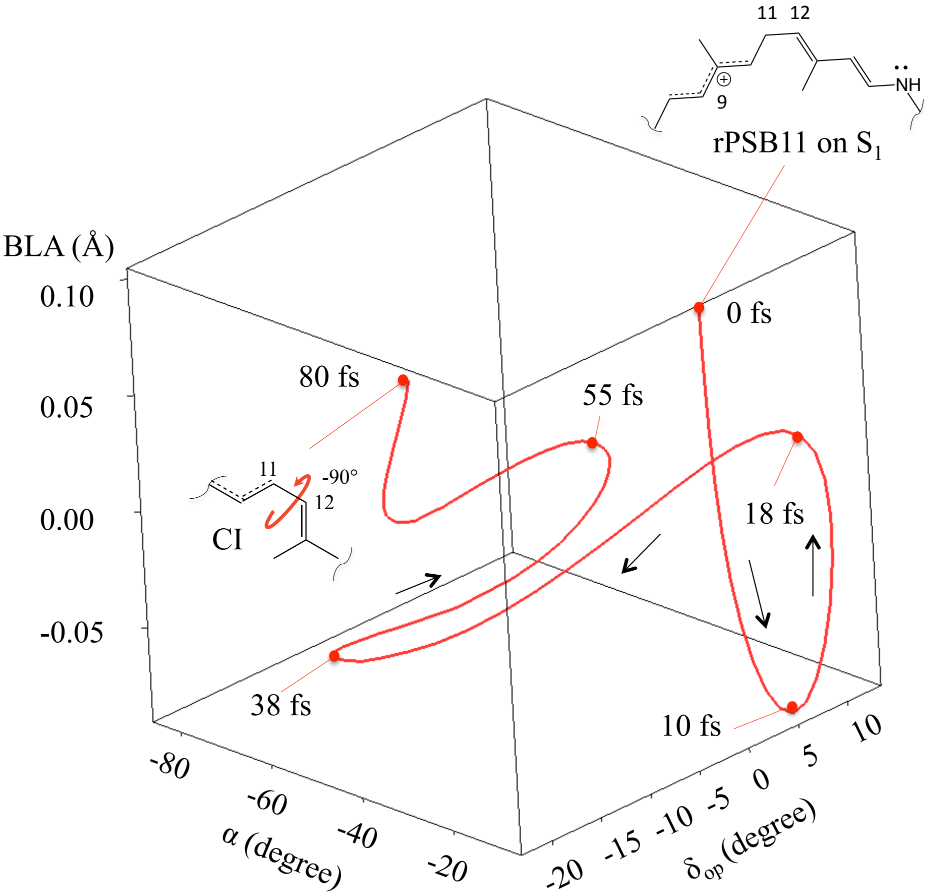

Figure 1.3 Reaction coordinates of Rh FC trajectory. The FC trajectory is initially dominated by the BLA motion, which is induced by the charge-transfer electronic configuration of the excited state molecule. The δ_{op} and α motions are active after 18 fs timescale, transfer the excited state rPSB11 towards CI with the C_{11}=C_{12} bond twisted of ca. -90 degree at 80 fs. The corresponding FC trajectory is reported in chapter V.

Despite experimental and theoretical achievements mentioned above, a single FC trajectory is not capable of providing the statistical converged S_1 lifetime and quantum yield of an entire Rh population directly. Moreover, it is unclear if and at what extent the observed vibrationally coherent motions, i.e. the coordinated and phased vibrational motion of all molecules belonging to the entire population, have a biological significance. Currently, no direct information on the role or impact of vibrational coherence on Rh photoisomerization has been reported.

An accurate description of the excited state Rh population has been computationally unaffordable until recent times, which have witnessed a dramatic development of computer hardware and suitable applicative software. Accordingly, in the present work we simulate and study the room-temperature population dynamics of Rh with a set of few hundreds semi-classical (also called “non-adiabatic”) trajectories. Such calculations start with initial conditions (geometries and velocities) at dark and then release them on S_1 with the same initial geometries and velocities. The simulated S_1 lifetime can be obtained by simply averaging the decay time of all trajectories or fitting with suitable mathematic equations[28]. The percent of trajectories reaching the rPSBAT product out of the total trajectories that decay to S_0 can be taken as the computed quantum yield[29]. In the following chapters, we document the impact of vibrational coherence on the Rh photoisomerization lifetime and quantum yield via the described population dynamics simulation.

More specifically, in Chapter II, we briefly introduce and explain the theoretical and computational methods applied in the presented Dissertation. In Chapter III we discuss a benchmarking study of the employed protocol for population dynamics simulation. In particular, we describe an original approach to generate a room temperature Boltzmann-like population and how we have benchmarked it using a 3 double-bond rPSB model of Anabaena sensory rhodopsin[28] to reduce the computational cost. In Chapter IV, we apply the benchmarked protocol to Rh, but still using a reduced 5 double-bond rPSB model. The reduced model is employed to show the impact of a specific phase relationship between the α and δ_{op} modes at the S_1 to S_0 decay point and the successful (i.e. proceeds to rPSBAT) or unsuccessful (i.e. gets back to rPSB11) isomerization outcome. We will see how such α/δ_{op} phase relationship also provides a theoretical explanation of a novel kind of isotopic effect on the rPSB11 quantum yield reported by our experimental collaborators[18]. In Chapter V we repeat the population dynamics simulation using a more realistic Rh model featuring a full rPSB11 chromophore. After showing that the simulated S_1 lifetime and quantum yield are consistent with the experimentally observation, we observe a contained, and somehow structured, decoherent process along the α mode, which is: (i) induced by the protein environment, (ii) splits the initially coherent excited state population into several subpopulations which decay at various decay timescale. Finally, we show that a maximized quantum yield and, therefore, extreme light sensitivity of Rh population can only be achieved if each subpopulation decaying to S_0 with a specific α/δ_{op} phase that favors photoproduct formation.

In summary, the theoretical work presented in this Dissertation provide a rather complete view of how vibrationally coherence can impact the efficiency of light-induced photoisomerization of Rh by modulating the subpopulations S_1 lifetime and quantum yield.

1.1 References

(1) Spudich, J. L.; Yang, C.-S.; Jung, K.-H.; Spudich, E. N. *Annu. Rev. Cell Dev. Biol.* **2000**, *16* (1), 365–392.

(2) Ernst, O. P.; Lodowski, D. T.; Elstner, M.; Hegemann, P.; Brown, L. S.; Kandori, H. *Chem. Rev.* **2014**, *114* (1), 126–163.

(3) Luk, H. L.; Melaccio, F.; Rinaldi, S.; Gozem, S.; Olivucci, M. *Proc. Natl. Acad. Sci.* **2015**, *112* (50), 15297–15302.

(4) Palczewski, K. *Annu. Rev. Biochem.* **2006**, *75* (1), 743–767.

(5) Luk, H. L.; Melaccio, F.; Rinaldi, S.; Gozem, S.; Olivucci, M. *Proc. Natl. Acad. Sci.* **2015**, *112* (50), 15297–15302.

(6) Blankenship, E.; Lodowski, D. T. In *Rhodopsin: Methods and Protocols*; 2015; Vol. 1271, pp 21–38.

(7) Kandori, H.; Shichida, Y.; Yoshizawa, T. *Biochem.* **2001**, *66* (11), 1197–1209.

(8) Yoshizawa, T.; Shichida, Y.; Matuoka, S. *Vision Res.* **1984**, *24* (11), 1455–1463.

(9) Fung, B. K.; Hurley, J. B.; Stryer, L. *Proc. Natl. Acad. Sci. U. S. A.* **1981**, *78* (1), 152–156.

(10) Doukas, A. G.; Junnarkar, M. R.; Alfano, R. R.; Callender, R. H.; Balogh-Nair, V. *Biophys. J.* **1985**, *47* (6), 795–798.

(11) Schoenlein, R. W.; Peteanu, L. A.; Wang, Q.; Mathies, R. A.; Shank, C. V. *J. Phys. Chem.* **1993**, *97* (46), 12087–12092.

(12) Dartnall, H. J. A. *Vision Res.* **1968**, *8* (4), 339–358.

(13) Doukas, A. G.; Junnarkar, M. R.; Alfano, R. R.; Callender, R. H.; Kakitani, T.; Honig, B. *Proc. Natl. Acad. Sci.* **1984**, *81* (15), 4790–4794.

(14) Mathies, R. A. *Nat. Chem.* **2015**, *7* (12), 945–947.

(15) Johnson, P. J. M.; Halpin, A.; Morizumi, T.; Prokhorenko, V. I.; Ernst, O. P.; Miller, R. J. D. *Nat. Chem.* **2015**, *7* (12), 980–986.

(16) Gozem, S.; Luk, H. L.; Schapiro, I.; Olivucci, M. *Chem. Rev.* **2017**, *117* (22), 13502–13565.

(17) Schapiro, I.; Ryazantsev, M. N.; Frutos, L. M.; Ferré, N.; Lindh, R.; Olivucci, M. *J. Am. Chem. Soc.* **2011**, *133* (10), 3354–3364.

(18) Schnedermann, C.; Yang, X.; Liebel, M.; Spillane, K. M.; Lugtenburg, J.; Fernández, I.; Valentini, A.; Schapiro, I.; Olivucci, M.; Kukura, P.; et al. *Nat. Chem.* **2018**, *10* (4), 449–455.

(19) Polli, D.; Altoè, P.; Weingart, O.; Spillane, K. M.; Manzoni, C.; Brida, D.; Tomasello, G.; Orlandi, G.; Kukura, P.; Mathies, R. A.; et al. *Nature* **2010**, *467* (7314), 440–443.

(20) Luo, D.-G. G.; Yue, W. W. S.; Ala-Laurila, P.; Yau, K.-W. W. *Science (80-.).* **2011**, *332* (6035), 1307–1312.

(21) Alexiev, U.; Farrens, D. L. *Biochim Biophys Acta* **2014**, *1837* (5), 694–709.

(22) Gozem, S.; Schapiro, I.; Ferre, N.; Olivucci, M. *Science (80-.).* **2012**, *337* (6099), 1225–1228.

(23) Garavelli, M.; Celani, P.; Bernardi, F.; Robb, M. A.; Olivucci, M. *J. Am. Chem. Soc.* **1997**, *119* (29), 6891–6901.

(24) Virshup, A. M.; Punwong, C.; Pogorelov, T. V.; Lindquist, B. A.; Ko, C.; Martínez, T. J. *J. Phys. Chem. B* **2009**, *113* (11), 3280–3291.

(25) Weingart, O.; Migani, A.; Olivucci, M.; Robb, M. A.; Buss, V.; Hunt, P. *J. Phys. Chem. A* **2004**, *108* (21), 4685–4693.

(26) Hayashi, S.; Taikhorshid, E.; Schulten, K. *Biophys. J.* **2009**, *96* (2), 403–416.

(27) Frutos, L. M.; Andruniow, T.; Santoro, F.; Ferre, N.; Olivucci, M. *Proc. Natl. Acad. Sci.*

2007, *104* (19), 7764–7769.

(28) Manathunga, M.; Yang, X.; Luk, H. L.; Gozem, S.; Frutos, L. M.; Valentini, A.; Ferrè, N.; Olivucci, M. *J. Chem. Theory Comput.* **2016**, *12* (2), 839–850.

(29) Polli, D.; Weingart, O.; Brida, D.; Poli, E.; Maiuri, M.; Spillane, K. M.; Bottoni, A.; Kukura, P.; Mathies, R. A.; Cerullo, G.; et al. *Angew. Chemie Int. Ed.* **2014**, *53* (9), 2504–2507.

CHAPTER II. METHODS

As mentioned in Chapter I, the photoisomerization of Rh occurs at an ultrafast timescale. Experimental approaches for probing such ultrafast reaction could be complex and expensive but also cannot provide direct, atomic-level mechanistic descriptions of the reaction dynamics and mechanism. Computational approaches capable of simulating the key photo-induced dynamics of a reacting molecule, on the other hand, provide a more affordable tool. In fact, computational quantum chemistry methods have been widely used in the investigatation of absorption spectra, photochemical and dynamical properties of Rh[1]. In this Dissertation, we use suitable computer model of Rh to compute the corresponding reaction coordinates and energy profiles. The basic theories, concepts as well as computational methods that are necessary to follow the presented research results are briefly introduced and explained in this chapter.

2.1 Born-Oppenheimer approximation and PES

Concisely, computational quantum chemistry is all about solving the Schrödinger equation (equation 2.1) to obtain the description of electrons that control the molecular structure as well as its reactivity.

$$\hat{H}\Psi=E\Psi \qquad (2.1)$$

where E is the energy, Ψ is the wavefunction and $\hat{H}$ is the Hamiltonian operator that includes all energy terms in a molecule. Considering the electrostatic repulsions among positive nuclear charges and among negative electrons, as well as the attraction between nuclei and electrons, the Schrödinger equation can then be written as equation 2.2:

$$(T_N+T_e+V_{NN}+V_{ee}+V_{eN})\Psi=E\Psi \qquad (2.2)$$

where T_N is the kinetic energy opearator of the nuclei and T_e is that of the electrons. V_{NN}, V_{ee} and V_{eN} are potential energy operator among the nuclei, among the electrons and between nuclei and electrons. The exact solution of Schrödinger equation requires a treatment of both nuclei coordinates and electrons coordinates, which is not achievable for complex many-body systems, thus requiring approximation for numerical solution to Schrödinger equation.

As stated above, the total energy of a molecule is defined as the sum of the total nuclear repulsion energy and the total electronic energy. To compute these quantities, we apply the Born-Oppenheimer approximation (BOA)[2], one of the most critical hypotheses in quantum chemistry. Since the mass of a nucleus is ca. 2000 times larger than that of an electron, the nuclei move much slower than the electrons. With such velocity difference, one can assume the nuclei are fixed in space despite of electrons motion. For instance, the absorbed photon energy promotes vertical excitation of rPSB11 from S_0 to S_1. The nuclear conformation of both structures can be considered identical, as the nuclei are so slow that are not capable of reacting to the instantaneous electronic structure change. The mathematic consequence of BOA is that the overall wavefunction can be written as a product of a nuclear component and an electron component:

$$\Psi(r,R)= \Psi_N(R)\times\Psi_{el}(r,R) \qquad (2.3)$$

where r is the electron coordinate and R is the nuclear coordinate. The nuclear wavefunction $\Psi_N(R)$ depends on the nuclear positions exclusively while the electronic wavefunction $\Psi_e(r,R)$ containing both electron and nuclear coordinates, depends parametrically on the nuclear positions (i.e., the electron cooridnates are variables and nuclear coordinates are consistant). The total Schrödinger equation can then be separated in nuclear and electronic parts. For a chosen molecule of which the configuration is R_1, the electronic part of the Schrödinger equation can be solved as:

$$H_{el}\Psi_{el}(r,R_1)=E_{el}\Psi_{el}(r,R_1) \qquad (2.4)$$

The potential energy E of such moelcule is a simple sum of the electronic energy and nuclear potential energy:

$$E(R_1)=E_{el}(r,R_1)+V_{NN}(R_1) \qquad (2.5)$$

Solving equation 2.4 for other nuclear configurations of interest yield a PES of a molecule. For a molecule of N atoms, each of its atoms can be specified with three Cartesian coordinates, (x, y, z), in sum 3N possible motions. As the external motions do not change the total potential energy, the PES is consequently a 3N-6 (minus 3 global translations and 3 global rotations along the x, y and z axis) dimensional space for a non-linear molecule and 3N-5 (minus 3 global translations and 2 global rotations along, for instance, the y and z axis) dimensional space for a linear molecule. In another words, the PES of a molecule depends on its internal coordinates and electronic structure.

PES allows determining the energy and structure of a molecule with mathematic approaches called optimization methods. In fact, the chemically most interesting points of a PES are the stationary points, where the gradients with respect to all 3N-6 internal coordinates are zero:

$$\frac{dE(R)}{dR_i}=0 \quad i=1, 2, 3, \cdots 3N-6 \qquad (2.6)$$

where R refers to all possible internal coordinates and R_i refers to a specific internal coordinate.

Of all types of stationary point, the most critical ones are minima and saddle points. The reactants, stable intermediates and products of a reaction could be represented by points of minimum on PES:

$$\frac{d^2E(Q)}{dQ^2_i}>0 \quad i=1, 2, 3, \cdots 3N-6 \qquad (2.7)$$

where $d^2E(Q)/dQ_i^2$ is the eigenvalue of the Hessian matrix written in terms of internal coordinates R, and Q_i are the eigenvectors (normal coordinates or modes). The transition state structure can be represented as the first order saddle point on PES, which is minima along all normal coordinates but one maximum along the normal coordinate corresponding to the reaction coordinates that is characterized by:

$$\frac{d^2E(Q)}{dQ^2{}_i}>0 \quad i=1,2,3,\cdots 3N\text{-}7 \qquad \frac{d^2E(Q)}{dQ^2{}_{RC}}<0 \qquad (2.8)$$

where Q_{RC} is the reaction coordinate.

2.2 Semi-classical trajectory

The application of BOA allows to decouple the nuclear and electronic wavefunction as the electrons respond to motion of nuclei instantaneously and one can neglect the details of electronic motion[3] (see equation 2.5). The potential energy E(R) can then be computed by solving the electronic part of the Schrödinger equation and in this case, we say that E(R) is determined via quantum mechanics (QM). Though the QM method provides us with accurate results, its high computational cost prevents us from applying it to large biological molecule such as a protein. One computationally convenient/enabling approach is to treat most of the large biological molecule using classical mechanics. In this case we say that we employ molecular mechanics (MM) where the atoms and bonds can be regarded as points with a given mass and charge, and as springs connecting these points, respectively. The energy and movement of atoms are then described by the sum of predefined functions containing fitted parameters (obtained from the experiment or from high-level QM calculations on model molecules). The entire set of such parameters (termed force field) determines the accuracy of the he MM potential energy.

Obviously, MM method, based on a sum of readily computable terms, is computational more affordable compared with QM method, which involves the solution of an eigenvalue problem. However, MM method is not cable of determining the electronic structure of a molecule or describing bond breaking and bond formation, as the electrons are treated as parameterized fixed charges and springs in the MM method. In the case of a photoisomerization reaction involving the breaking and formation of a C=C double bond, a quantum mechanical description of the electrons is obviously required. Thus, to make the E(R) calculation affordable for a large biological molecule, one can combine QM and MM methods by treating the relevant electrons (i.e. the ones describing the bond breaking and bond forming processes) at QM level but the nuclei at the MM level. The total E(R) of the molecule is then express as: $E(R)= E_{MM}(R) + E_{QM}(R) + E_{QM/MM}$ where $E_{QM/MM}$ describes the QM/MM interaction. In this dissertation the $E_{QM/MM}(R)$ contribution is computed according to the so called electrostatic embedding method[4]. The QM and MM hybrid strategy described above is called QM/MM method.

To determine the motion of nuclei one need to use the Newton's second law F = ma. The corresponding force acting on nuclei is the negative gradient of PES:

$$\text{force} = -\frac{dE(R)}{dR} \qquad (2.9)$$

The simulation of molecular motion on PES as a function of time with the above method is termed classical trajectory simulation. For adiabatic process (i.e., the reaction occurs on a single state or, equivalently, the nuclei move along a single PES), the BOA is generally valid since the nuclear and electronic motions are always de-coupled. However, when the reaction involves more than one states (e.g., the photoisomerization of rPSB11), the inevitable non-adiabatic transitions between two electronic states (i.e. from S_1 to S_0) leads to a breakdown of the BOA. As mentioned in Chapter I, the photoisomerization of rPBS11 follows a path connecting the vertical excitation region of S_1 with the CI where it decays to S_0. When the excited rPSB11 chromophore approaching the CI, the non-adiabatic coupling become large as the electronic wavefunctions of the S_0 and S_1 mix rapidly, demanding a description of accompanied electronic-nuclear motion (Figure 2.1)[5,6]. Again, in such situation a surface hopping method[7,8] is employed, which allows transition of a molecule from one PES to another when the transition possibility, a function of non-adiabatic coupling vector measuring the wavefunction mixing, meets certain hopping criteria.

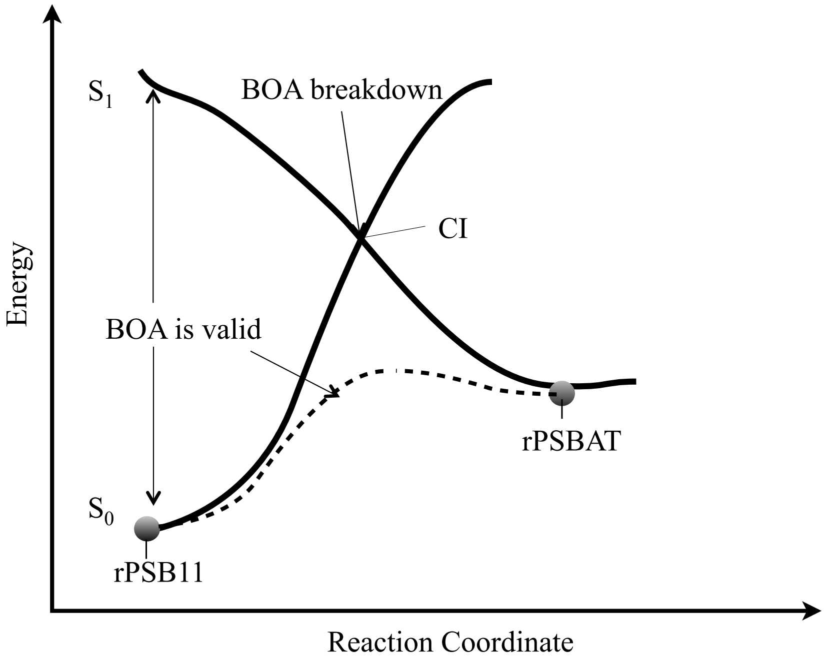

Figure 2.1 Breakdown of BOA. The BOA is valid in thermal isomerization and vertical excitation to S$_1$ but is not valid as the excited state molecule approaches the CI, where the surface hopping method is applied.

2.3 Electronic structure theory method

Above we have discussed the ideas to simplify the calculation by separating of motions of electrons and nuclei as well as to obtain a reaction coordinates on a PES. The remaining critical question is how to solve the electronic part of Schrödinger equation. Over the past decades, numerous quantum chemistry methods have been developed[9]. Below we briefly introduce the few methods employed in this work.

According to the Pauli exclusion principle[10], two electrons of the same atomic orbital must display different spin quantum number with either +1/2 or -1/2. To accommodate spin into the electronic Hamiltonian given in equation 2.4, variable x is introduced to include both space variable r and spin variable s, given x = (r, s). The spin-orbital function of an electron can then be written as a product of its molecular orbital function ϕ (r) (which is a function of space variable r) and corresponding spin function ω (s) (which is a function of spin variable s) as:

$$\phi\,(x)=\phi\,(r)\omega(s) \qquad (2.10)$$

The outcome of Pauli exclusion principle stated above is that the wavefunction of a N-electron system must be antisymmetric. A convenient expression of such a wavefunction is a Slater determinant:

$$\Psi(x_1, x_2,\cdots x_N)=\frac{1}{\sqrt{N!}}\begin{bmatrix}\phi_1(x_1) & \cdots & \phi_N(x_1)\\ \vdots & \ddots & \vdots \\ \phi_1(x_N) & \cdots & \phi_N(x_N)\end{bmatrix} \qquad (2.11)$$

Obviously, Salter determinant satisfies both antisysmmetry principle and Pauli exclusion principle that exchanging two columns or rows of determinant resulting in changing of its sign and the value of determinant is zero when two electrons have the same x coordinate.

In the simplest case, the electronic wavefunction of a molecule is composed of a single Slater determinant and this is the Hartree-Fock (HF)[11] method. One advantage of HF method is its relatively low computational cost compared to methods corresponding to higher levels of theory[12]. However, the HF method is not cable of describing excited state photochemistry, as it is limited to closed-shell systems[13]. Another shortcoming of the HF method is that it always results in a higher energy than the exact result due to the lack of static and dynamical electron correlation[14]. In the HF method, the motion of the electrons is treated independently from each other and their repulsive energy is treated in an average way. In another word, the instantaneous repulsion is not involved in the HF method.

One technique to improve the HF method is to include all possible Slater determinants. This is known as full configuration interaction (FCI)[15] wavefunction:

$$\Psi_{FCI}=C_0\Psi_{HF}+\sum_{i=1} C_i\Psi_i \qquad (2.12)$$

The FCI method provides the exact solution to the electronic Schrödinger equation when considering all possible molecular orbitals in the calculation. Though in practice this number of molecular orbitals is finite as the energy does not change after that a large enough number of orbitals is used, such number (i.e., again, reflecting the number of electronic configurations) in a biological molecule such as rPSB11 is too large. Consequently, the FCI method cannot be used to compute the Rh potential energy even when the QM/MM method is employed. A "complete active space self-consistent field" (CASSCF)[16] method allows us to limit the selection of the FCI electronic configurations to the one generated from the most important molecular orbitals and electrons of the molecule. This is equivalent to defining an "active space" containing the electrons and orbitals describing the chemical event to be investigated (e.g. a bond breaking or a photon absorption). As schematically represented in Figure 2.2a, all possible electron configurations generated with the electrons and orbitals within the red box, which contains 4 electrons and 4 orbitals, define a (4,4) active space and are thus included in the CASSCF wavefunction. In contrast, the electron configurations produced moving electrons from outside the box into the box or from the box to outside the box are neglected. In the case of rPBS11 photoisomerization, we included the entire π-system of the moiety (Figure 2.2b colored in red), 12 π-electrons and 12 π-orbitals in total, into a (12,12) active space.

In this Dissertation, the CASSCF method is applied to obtain the $E_{QM}(R)$ term of the $E_{QM/MM}$ energy necessary for computing the geometries and reaction coordinate of the Rh isomerization. However, the $E_{QM}(R)$ generated from CASSCF method is always higher than the observed value as it lacks part of the description of the dynamic electron correlation. The second order multiconfigurational perturbation theory (CASPT2)[17] which use the CASSCF wavefunction as reference wavefunction, introduces dynamic electron correlation into the system, thus providing a more accurate evaluation of electronic energy. Here we adopt a CASPT2//CASSCF protocol that has been documented within previous research on Rh photoisomerization[18], in which the energy evaluation is performed at the CASPT2 level while the geometry (or trajectory) calculation is performed at the CASSCF level.

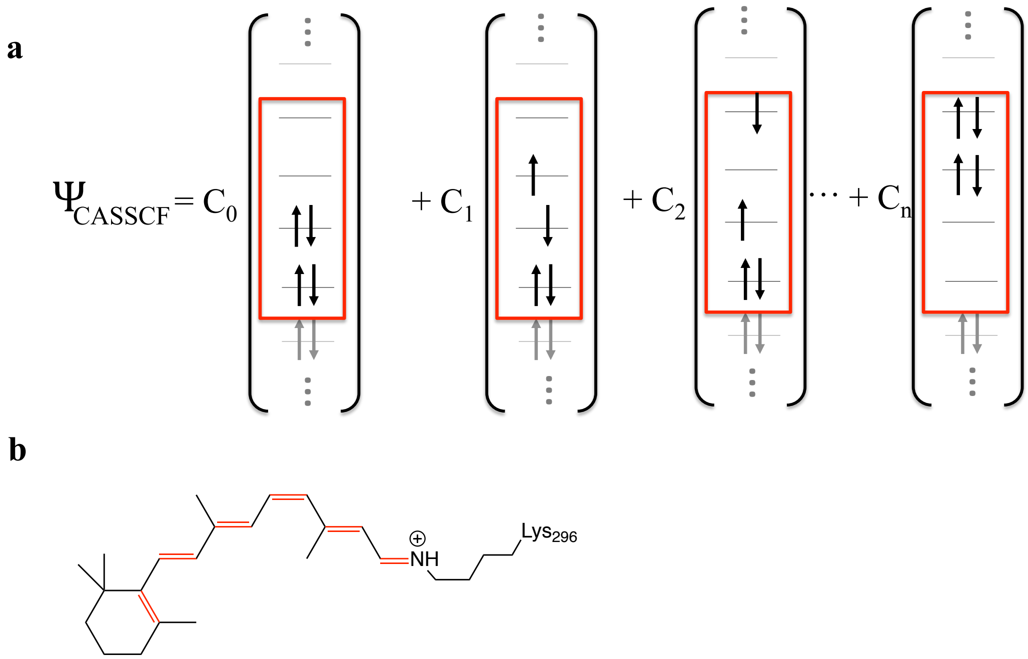

Figure 2.2 CASSCF level of theory. **a.** A schematic representation of a (4,4) CASSCF wavefunction. Active electrons and orbitals are in black and in red box. Inactive electrons and orbitals are in gray. **b.** We include the entire π-system (red) of rPSB11 into active space.

2.4 Automatic rhodopsin (QM/MM) modeling protocol

For the present Dissertation research, obtaining a high-quality three-dimensional model of Rh is essential. To do this we have employed a prototype automatic rhodopsin modeling (ARM)[19] protocol for the construction of Rh models. The models constructed using ARM are globally uncharged, gas-phase QM/MM models. More specifically and as outlined above, rPSB forms the QM subsystem and is treated with a CASPT2//CASSCF level of theory. The opsin cavity, on the other hand, forms the MM subsystem and is calculated with Amber force field[20] to compute the interactions among MM and also between MM and QM atoms. Residue and water molecules within certain distance from the retinal chromophore forming a cavity and the retinal chromophore are flexible during the calculation while all atoms outside the cavity are kept fixed. An H atom is added as QM/MM frontier cross the bond connecting the Cσ and Cε of the rPSB attached lysine. The QM/MM interaction is treated with the electrostatic potential fitted (ESPF) methodology[21] which correspond to the anticipated electrostatic embedding. Again, the total energy of the QM/MM system is given by equation 2.13.

$$E_{total}=E_{QM}+E_{MM}+E_{QM/MM} \qquad (2.13)$$

The workflow of ARM is shown in Figure 2.3. Briefly, the input of ARM is a protein structure file in PDB (Protein Data Bank) format and the ionization state of the starting structure is determined by ProPka[22]. Then external Na+ and Cl− ions necessary for charge neutralization as required for an ARM model are added using the in-house coded ION module. The DOWSER[23] program adds hydrogen and polar atoms based on an energy minimization criteria. The obtained geometry is then relaxed at room temperature by GROMACS[24] with a 1 ns molecular dynamics simulation (MD) on the cavity residue side-chains and the retinal chromophore. The MD output structure is finally optimized with combined Molcas/Tinker[25,26] package at QM/MM level to reach the final structure.

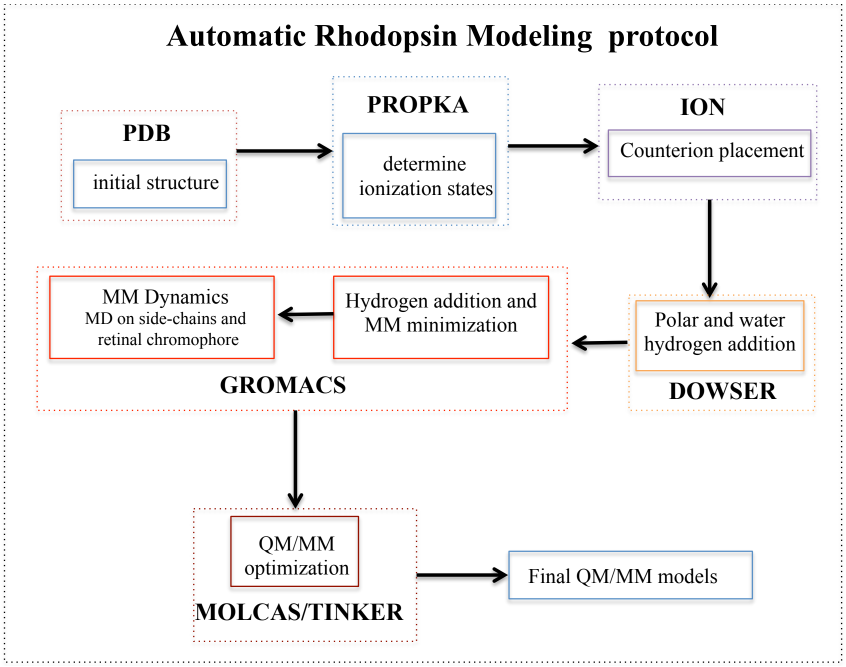

Figure 2.3 ARM workflow. Names of programs are in bold and bashed box with their functions in solid box.

2.5 References

(1) Gozem, S.; Luk, H. L.; Schapiro, I.; Olivucci, M. *Chem. Rev.* **2017**, *117* (22), 13502–13565.

(2) Born, M.; Oppenheimer, R. *Ann. Phys.* **1927**, *389* (20), 457–484.

(3) Curchod, B. F. E.; Martinez, T. J. *Chem. Rev.* **2018**, *118* (7), 3305–3336.

(4) Field, M. J.; Bash, P. A.; Karplus, M. *J. Comput. Chem.* **1990**, *11* (6), 700–733.

(5) Subotnik, J. E.; Jain, A.; Landry, B.; Petit, A.; Ouyang, W.; Bellonzi, N. *Annu. Rev. Phys. Chem.* **2016**, *67* (1), 387–417.

(6) Yarkony, D. R. *Chem. Rev.* **2012**, *112* (1), 481–498.

(7) Tully, J. C. *J. Chem. Phys.* **1990**, *93* (2), 1061–1071.

(8) Tully, J. C.; Preston, R. K. *J. Chem. Phys.* **1971**, *55* (2), 562–572.

(9) Taft, C. A.; da Silva, V. B.; da Silva, C. H. T. de P. *J. Pharm. Sci.* **2008**, *97* (3), 1089–1098.

(10) Pauli, W. *Zeitschrift für Phys.* **2008**, *31* (1), 765–783.

(11) Hartree, D. R. *Math. Proc. Cambridge Philos. Soc.* **1928**, *24* (1), 111–132.

(12) Echenique, P.; Alonso, J. L. *Mol. Phys.* **2007**, *105* (23–24), 3057–3098.

(13) Cohen, H. D.; Roothaan, C. C. J. *J. Chem. Phys.* **1965**, *43* (10), S34–S39.

(14) Whitfield, J. D.; Love, P. J.; Aspuru-Guzik, A. *Phys. Chem. Chem. Phys.* **2012**, *15* (2), 397–411.

(15) Knowles, P. J.; Handy, N. C. *Chem. Phys. Lett.* **1984**, *111* (4–5), 315–321.

(16) Roos, B. O. In *Advances in Chemical Physics*; 2007; pp 399–445.

(17) Andersson, K.; Malmqvist, P.; Roos, B. O. *J. Chem. Phys.* **1992**, *96* (2), 1218–1226.

(18) Frutos, L. M.; Andruniow, T.; Santoro, F.; Ferre, N.; Olivucci, M. *Proc. Natl. Acad. Sci.* **2007**, *104* (19), 7764–7769.

(19) Melaccio, F.; del Carmen Marín, M.; Valentini, A.; Montisci, F.; Rinaldi, S.; Cherubini, M.;

Yang, X.; Kato, Y.; Stenrup, M.; Orozco-Gonzalez, Y.; et al. *J. Chem. Theory Comput.* **2016**, *12* (12), 6020–6034.

(20) Cornell, W. D.; Cieplak, P.; Bayly, C. I.; Gould, I. R.; Merz, K. M.; Ferguson, D. M.; Spellmeyer, D. C.; Fox, T.; Caldwell, J. W.; Kollman, P. A. *J. Am. Chem. Soc.* **1996**, *118* (9), 2309.

(21) Ferre, N.; Cembran, A.; Garavelli, M.; Olivucci, M. *Theor. Chem. Acc.* **2004**, *112* (4), 335–341.

(22) Olsson, M. H. M.; Shondergaard, C. R.; Rostkowski, M.; Jensen, J. H. *J Chem Theory Comput* **2011**, *7* (2), 525–537.

(23) Zhang, L.; Hermans, J. *Proteins* **1996**, *24* (4), 433–438.

(24) Pronk, S.; Páll, S.; Schulz, R.; Larsson, P.; Bjelkmar, P.; Apostolov, R.; Shirts, M. R.; Smith, J. C.; Kasson, P. M.; van der Spoel, D.; et al. *Bioinformatics* **2013**, *29* (7), 845–854.

(25) Aquilante, F. *J. Comput. Chem.* **2016**, *37*.

(26) Ponder, J. W.; Richards, F. M. *J. Comput. Chem.* **1987**, *8* (7), 1016–1024.

CHAPTER III. A BENCHMARKING STUDY: POPULATION DYNAMICS SIMULATION OF RHOFOPSIN WITH REDUCED RETINAL CHROMOPHORES

This Chapter is*, in part,* reproduced with permission from Manathunga, M.; Yang, X.; Luk, H. L.; Gozem, S.; Frutos, L. M.; Valentini, A.; Ferre, N.; Olivucci, M. *J. Chem. Theory Comput.* **2016**, *12* (2), 839–850. Copyright © 2019 American Chemical Society

3.1 Abstract

While the light-induced population dynamics of different rhodopsins has been investigated spectroscopically, systematic computational studies have not yet been possible due to the phenomenally high cost of suitable level of quantum chemical methods and the need of propagating hundreds, if not thousands, of non-adiabatic trajectories. Here we explore the possibility of studying the photodynamics of rhodopsins by constructing and investigating QM/MM models featuring reduced retinal chromophores. In order to do so we use the sensory rhodopsin found in the cyanobacterium Anabaena PCC7120 (ASR) as a benchmark system and in preparation to the investigation of the population dynamics of Rh. We find that the mechanistic features associated with the excited state dynamics of QM/MM models of ASR are reproduced using models incorporating a minimal (i.e., three double-bond) chromophore. Furthermore, we show that ensembles of non-adiabatic ASR trajectories computed using the same abridged models replicate the trends in spectroscopy and lifetimes estimated using unabridged models and observed experimentally at room temperature. We conclude that a further expansion of these studies may lead to low-cost QM/MM models of rhodopsins that may be used as effective tools in investigating their photochemical properties.

3.2 Introduction

As mentioned in Chapter I and Chapter II, the photoisomerization of the rhodopsin chromophore occurs on a sub-picosecond time scale. Thus, the experimental approach necessary for studying the photoisomerization mechanism could be very demanding and not suitable for systematic investigations. Accordingly, the development of computational tools allowing for a practical and effective study of the photoisomerization of rhodopsins is highly desirable.

The photoisomerization of rhodopsins is computational investigated by constructing QM/MM models of the protein starting from crystallographic data or suitable homology models[1]. These QM/MM models are then used for subsequent photochemical reaction paths or non-adiabatic trajectory computations. However, the high computational cost associated with the QM methods required for excited state and, therefore, non-adiabatic trajectory calculations limits the maximum number of trajectories that can be computed and, in principle, the statistical accuracy of the resulting dynamics. Indeed, in many trajectory studies it is assumed that the computation of a single trajectory started from the protein ground state S_0 equilibrium structure at zero K (called "FC trajectory") provides information on the excited state dynamics of the entire population at room temperature[2–4].

The target of the present benchmarking study is twofold. The first, substantially technical, target is to investigate the possibility of reducing the computational cost by employing an abridged but affordable QM/MM rhodopsin model incorporating a structurally modified retinal chromophore with three, rather than six, conjugating double bonds (Figure 3.1). To study the limitations of such model, we compare the corresponding FC trajectories with those obtained using models incorporating a full chromophore. The target is to show whether the basic mechanistic features associated with the excited state dynamics are reproducible. The second and more applicative target is to develop a protocol for rapidly getting information on the kinetic parameters and photochemical reactivity in large rhodopsin sets at room temperature. In fact, affordable abridged models would allow us to compute hundreds of QM/MM trajectories necessary to achieve a description of the molecular population evolution at room temperature.

We employ the sensory rhodopsin from the cyanobacterium Anabaena PCC7120 (Anabaena sensory rhodopsin, ASR)[5] as a convenient benchmark molecule. In fact, while in most rhodopsins the function is initiated through a single isomerization (e.g., usually from all-*trans* to 13-*cis* in microbial rhodopsins and from 11-*cis* to all-*trans* in animal rhodopsins), the ASR function is driven by the interconversion of two forms, ASR_{AT} and ASR_{13C}, featuring the all-*trans*,15-*anti* and 13-*cis*,15-*syn* chromophores, respectively (see Figure 3.1, top)[6]. Accordingly, the ASR_{AT} model can be employed to study the *trans* → *cis* isomerization and the ASR_{13C} model to study the inverse reaction. Furthermore, these forms display significant differences in isomerization quantum yields and kinetics thus providing a basis for evaluating the quality of the constructed QM/MM models. Indeed, the quantum yields were reported to be 0.4 and 0.1 for ASR_{AT} and ASR_{13C}, respectively[7,8], while kinetics measurements indicate that ASR_{13C} isomerizes in 0.15−0.25 ps whereas the opposite ASR_{AT} isomerization takes 0.75−4.00 ps[9]. A recent study has shown that FC trajectories computed using unabridged ASR_{AT} and ASR_{13C} QM/MM models produce kinetic data consistent with the corresponding observed quantities[10].

As anticipated above, the present study is based on the construction of ASR_{AT} and ASR_{13C} QM/MM models incorporating abridged retinal chromophores featuring three double-bond (from now on called PSB3 chromophores). These modified models, ASR_{AT}-M and ASR_{13C}-M, respectively, are obtained by shortening the native chromophores as shown in Figure 3.1. In the gas-phase, the PSB3 chromophore is known to reproduce several features of the full chromophore and for this reason has been extensively used as a benchmark for investigating the photochemistry of rhodopsin at low computational cost[11−14]. Below, we will assess the magnitude of such differences in ASR_{AT}-M and ASR_{13C}-M models where the PSB3 chromophore is mechanically and electrostatically embedded in the protein "molecular" environment and not studied in isolated conditions. In Section 3.3 we report a detailed description of the construction of the ASR_{AT}-M and ASR_{13C}-M models and of the sampling method used to simulate their room temperature populations. Section 3.4 is divided in two result subsections. In subsection 3.4.1 we compare the FC trajectories computed at ASR_{AT}-M and ASR_{13C}-M models with the reported trajectories computed with the full retinal model. In subsection 3.4.2 we study the room temperature photoisomerization kinetics of a 400 semi-classical (non-adiabatic) trajectory ensembles for both the ASR_{13C}-M and ASR_{AT}-M model. We find that, consistently with the FC trajectory results, the ASR_{13C}-M population decay is significantly faster than the decay of the ASR_{AT}-M population thus reproducing the trend observed for the corresponding experimental systems.

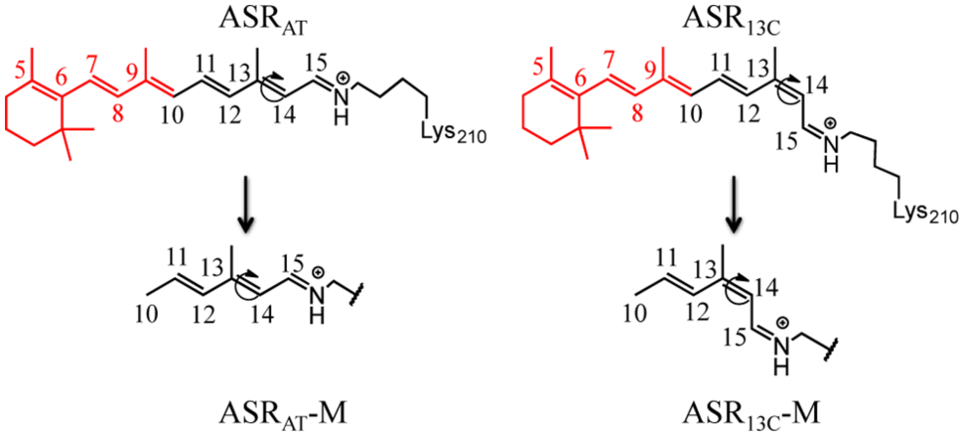

Figure 3.1 Modified ASR models. Modified models are constructed by removing a part of the chromophore shown in red.

3.3 Method

The ASR_{AT}-M and ASR_{13C}-M models were constructed by discarding the C_1–C_{10} portion of the retinal chromophore from the corresponding unabridged ASR_{AT} and ASR_{13C} models, respectively (see Figure 3.1 for a schematic illustration of the process). Accordingly, the equilibrium structures of the original ASR_{AT} and ASR_{13C} models were constructed following the protocol reported in section 2.5 of Chapter II. Their chromophores were then trimmed to obtain the corresponding cavity embedded PSB3 chromophores (see Figure 3.2). At the frontier between the QM subsystem (i.e., the PSB3 chromophore) and the MM subsystem (the protein), a hydrogen link atom was employed to saturate the bond between the last QM atom and the first MM atom in the Lys210 residue.

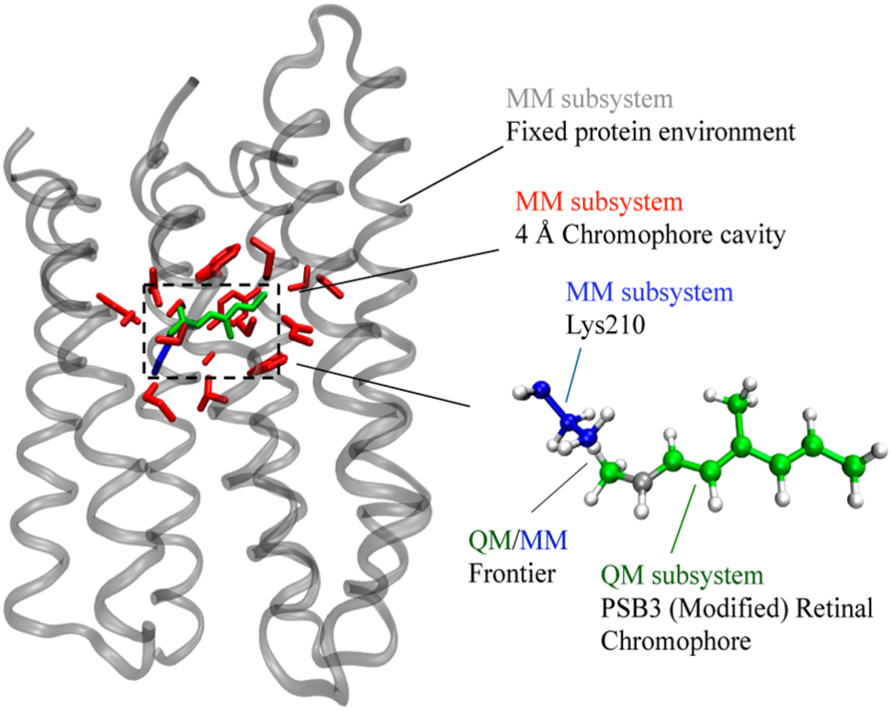

Figure 3.2 PSB3 ASR_{AT}-M model. The QM subsystem is colored in green (C and N atoms) and silver (H atoms connected to green atoms). The MM subsystem components are colored in grey (fixed atoms displayed in ribbon representation), in red (flexible cavity side-chains), in blue (flexible Lys210 side-chain) and in silver (H atoms connected to the blue atoms). The 'Frontier label' points to the H link-atom, which is part of the QM subsystem.

The original chromophore cavities, defined by the MM subsystem side chains with at least one atom not more than 4 Å far from any QM atom, were redefined. The resulting models were then relaxed (only the cavity residues and the QM subsystem are free to move) to obtain the equilibrium geometries of the final ASR_{AT}-M and ASR_{13C}-M models. As shown in Figure 3.3 for ASR_{AT}-M, the cavities hosting the reduced PSB3 chromophores conserve, substantially, the same cavity shape of the original ASR_{AT} and ASR_{13C} models as the above procedure avoids the collapse of the residues in the vicinity of the removed moieties upon relaxation.

As also anticipated in Chapter II the calculations were performed using the MOLCAS software package[15] included in the ARM workflow. Same thing for the TINKER software package[16] which is coupled to MOLCAS to perform the QM/MM calculations and employs the AMBER-FF94 parameters. In ARM the description of the electrostatic embedding of the QM subsystem into the MM subsystem was treated using the electrostatic potential fitted (ESPF) methodology[14,17]. FC trajectories were computed using a deterministic surface-hop method[18–21]. The room temperature trajectories were instead computed using the stochastic Tully surface-hop method[19,22]. The required initial conditions were computed using a protocol yielding Boltzmann-like distributions. More specifically, 400 initial conditions were generated using the following 3-step protocol:

- Room temperature molecular dynamics (40 ns) was performed at the MM level for both the unabridged ASR_{13C} and ASR_{AT} models using a MM parameterized retinal chromophore and keeping fixed the protein backbone and side-chains outside the 4 Å cavity region.
- Geometries and velocities corresponding to 400 snapshots were extracted from the above simulations at every 100 ps interval, and ASR_{13C}-M and ASR_{AT}-M models

were created for each snapshot by substituting the original chromophores with the corresponding abridged PSB3 chromophore. The new 4 Å cavities are then redefined as explained above.

- Each ASR_{13C}-M and ASR_{AT}-M model was relaxing on ground state for 200 fs a at QM level. The final geometry and velocity vectors were taken as initial conditions for the subsequent excited state non-adiabatic trajectory computation.

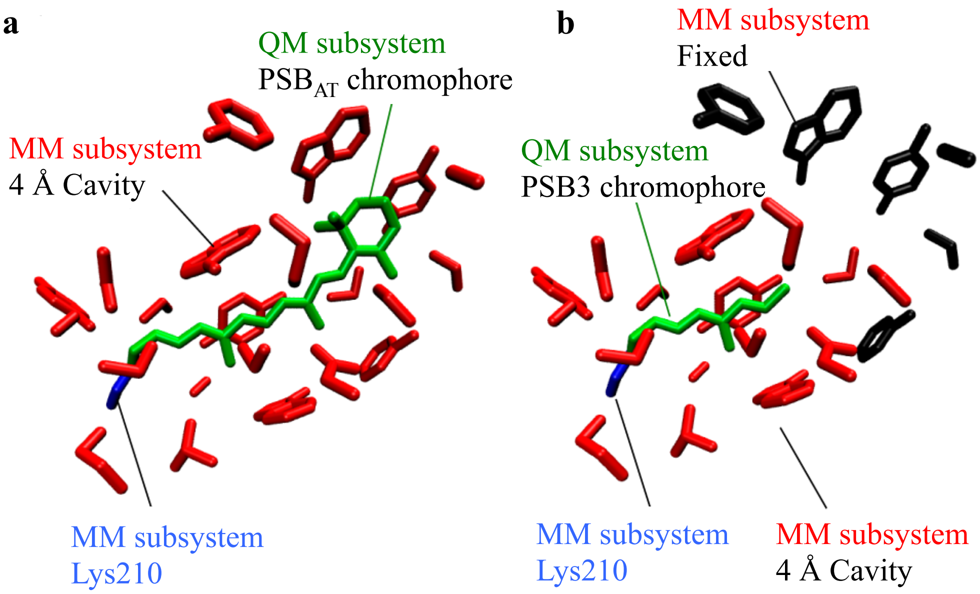

Figure 3.3 ASR_{AT} and ASR_{AT}-M cavity. **a.** Cavity of the full ASR_{AT} model. The QM chromophore is in green, the chromophore bound lysine (Lys 210) is in blue, and the rest of the MM cavity residues are in red. **b.** Cavity defined around the reduced retinal chromophore of the ASRAT-M model. The MM residues originally belonging to the ASRAT cavity and located outside the ASRAT-M cavity are shown in black and are kept frozen during the computations.

3.4 Results and discussion

3.4.1 Comparison of FC trajectories computed with abridged and unabridged ASR QM/MM models

The ultrafast excited state dynamics of ASR_{AT}-M and ASR_{13C}-M has been probed by computing the corresponding FC trajectories. In both cases we propagated the trajectories for 200 fs. The simulated S_1 lifetime (τ_{FC}) is defined as the time required to intercept the S_1/S_0 CI located halfway along the isomerization coordinate (typically when the $C_{13}=C_{14}$ double bond is ca. 90 degree twisted). In Table 3.1 the results are compared to the observed S_1 lifetimes for ASR and with the previously reported FC trajectories for the unabridged ASR models. The corresponding S_0 and S_1 potential energy profiles are reported in Figure 3.4. ASR_{AT}-M and ASR_{13C}-M models yield the same trend (but very different magnitudes) in τ_{FC} values found for the unabridged ASR_{AT} and ASR_{13C} models as well as for the observed data. In fact, τ_{FC} for ASR_{AT}-M is larger than that of the ASR_{13C}-M indicating a longer S_1 lifetime and a slower product formation time. An additional test reinforcing the similarity between the abridged models and the original ASR_{AT} and ASR_{13C} models is related to the S_1 reaction coordinate. The reaction coordinate of both ASR forms corresponds to a bicycle-pedal motion described by the clockwise and counterclockwise twisting of the $C_{13}=C_{14}$ and $C_{15}=N$ bonds respectively, while the $C_{11}=C_{12}$ bond remains substantially unreactive as shown in Figure 3.5. It is concluded that, mechanistically, the PSB3 in the abridged models follow the same, relatively complex, reaction coordinate of full chromophore models (but with different speeds).

Table 3.1 Observed[8,9] and computed S_1 lifetime (τ) and λ^a_{max} of unabridged ASR[10] and modified ASR models

	ASR observed		**ASR simulated**		**ASR-M simulated**	
Model	**τ (fs)**	**λ_{max} (nm)**	**τ_{FC} (fs)**	**λ_{max} (nm)**	**τ_{FC} (fs)**	**λ_{max} (nm)**
AT	750/4000	549	> 400	533	61	336
13C	150	537	150	527	53	329

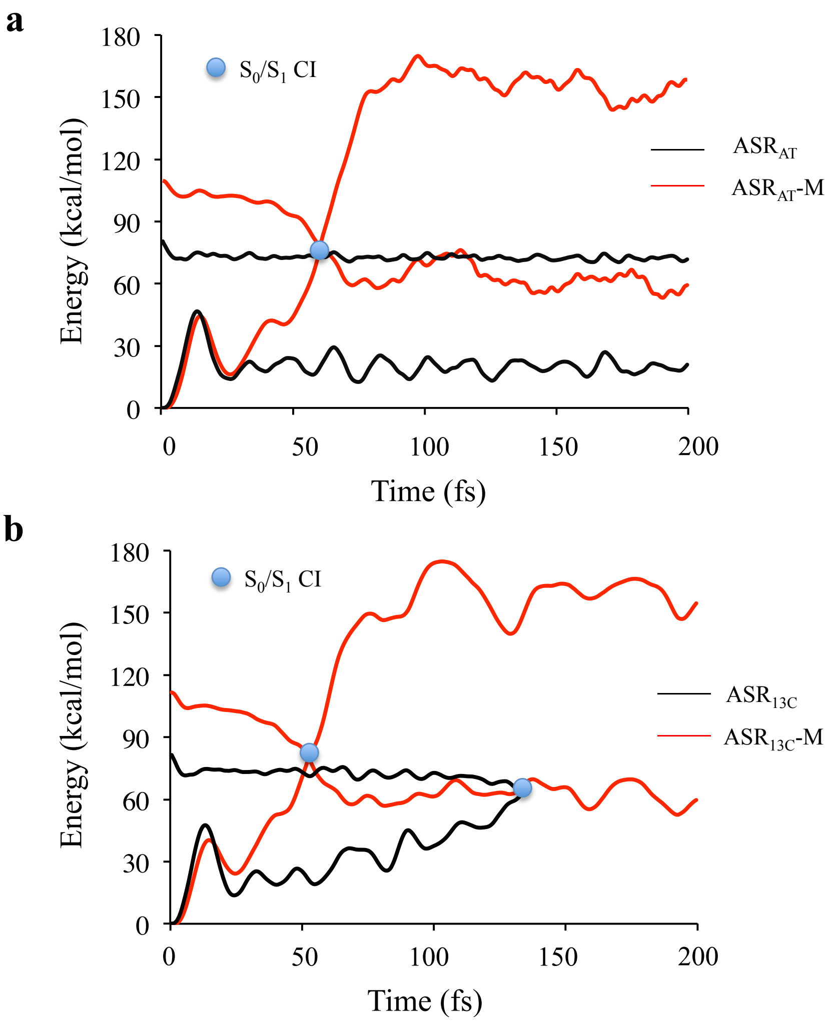

Figure 3.4 FC trajectories of unabridged and modified models. **a.** Comparison between ASR_{AT} (in black) and ASR_{AT}-M (in red) **b.** Comparison between ASR_{13C} (in black) and ASR_{13C}-M (in red). In both case, the trajectories have been released from the corresponding S_1 FC point with zero initial velocity. The circles represent points of surface hop located in the vicinity of a S_0/S_1 CI point.

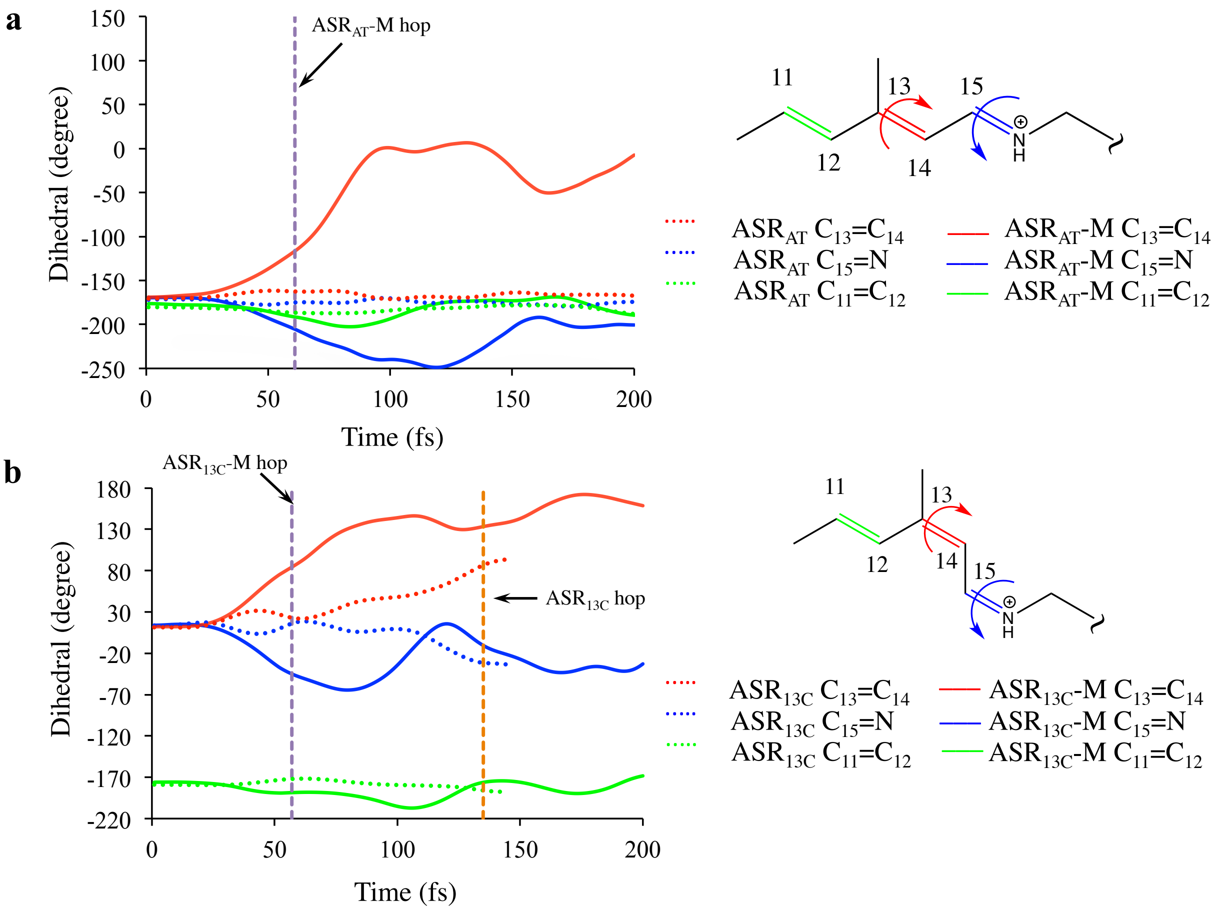

Figure 3.5 Isomerization coordinate for unabridged and modified models. **a.** ASR$_{AT}$ **b.** ASR$_{13C}$. The dihedral angle progression along the FC trajectory is plotted for the torsion of C_{15}=N double bond (in blue), of C_{13}=C_{14} double bond (in red) and of C_{11}=C_{12} double bond (in green) using solid line for modified models and dashed line for full retinal models. The vertical dashed line indicates corresponding hop event. It is clear that the modified models reproduced a bicycle-pedal motion of the full retinal model that can be described by the clockwise and counterclockwise twisting of the C_{13}=C_{14} and C_{15}=N bonds, while the C_{11}=C_{12} bond remains substantially unreactive.

3.4.2 Probing the room temperature dynamics

The results above suggest that the PSB3 models are able to reproduce basic kinetic features of full chromophore models. However, obviously, a single FC trajectory is insufficient to produce statistically meaningful results, and a large set of trajectories is required to derive quantities such as quantum yields and converged excited state lifetime parameters. As we would discuss below there are two parts of the population dynamics calculation affecting the statistical significance of the results: the Boltzmann-like distribution computation and the surface-hop decision. The initial conditions generated following the protocol reported in section 3.3 requires an initial random seed[23], and, similarly, during each Tully surface-hop trajectory a random number is required whenever a hop decision has to be taken[19]. Here the room temperature, population dynamics for the photoisomerization of ASR_{AT}-M and ASR_{13C}-M is investigated using ensembles of 400 trajectories. Before computing the trajectory, the quality of the computed Boltzmann-like distributions was evaluated by plotting the total energy and dihedral angle values of the isomerizing $–C_{12}–C_{13}=C_{14}-C_{15}-$ double bond. These are reported in the bar-diagrams of Figure 3.6 for ASR_{AT}-M and ASR_{13C}-M and show the expected Gaussian-like shape. The central dihedral values of the ASR_{AT}-M and ASR_{13C}-M initial conditions distribution, which are -190 and 20 degrees, respectively, indicate both models are pre-twisted in the same clockwise direction due to the asymmetric protein environment (i.e., dihedrals of ASR_{AT}-M and ASR_{13C}-M are not exactly -180 and 0 degrees) and consistently with the corresponding S_0 equilibrium structures of Figure S3.1 (see section 3.7) and clockwise isomerization direction of Figure 3.5.

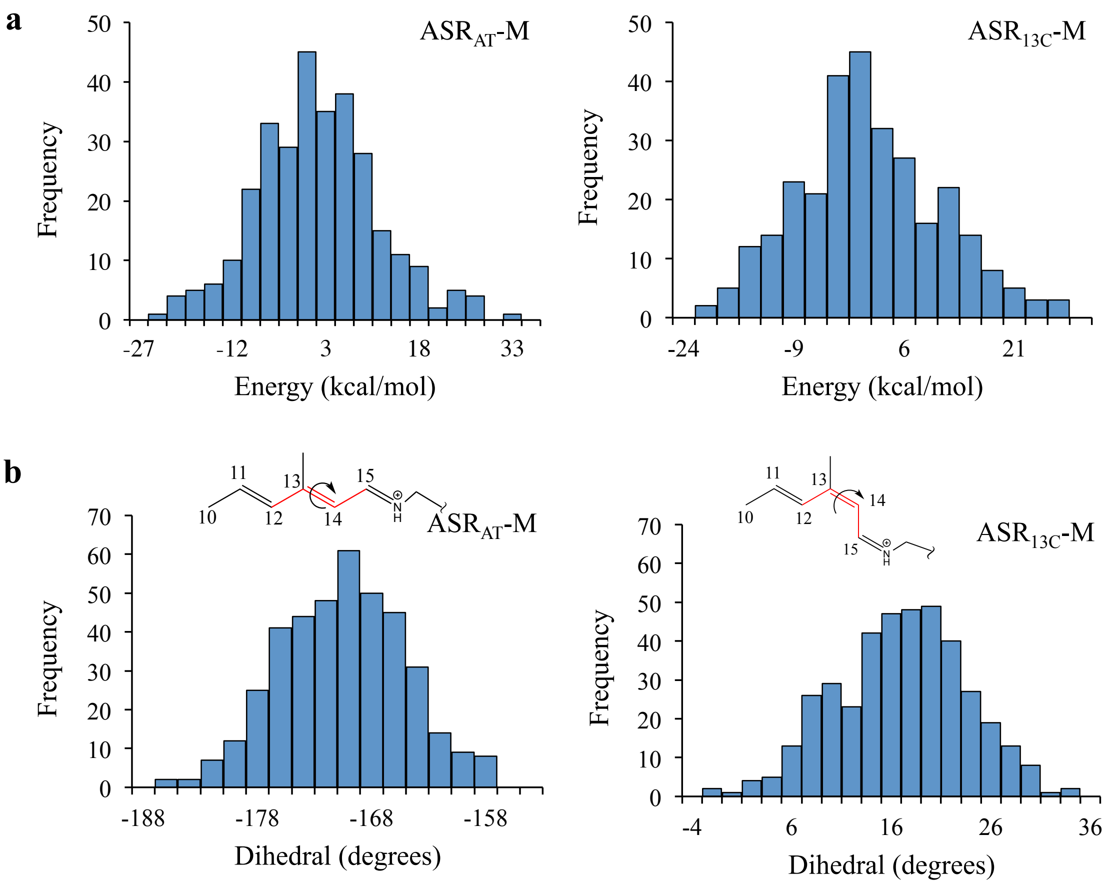

Figure 3.6 Initial condition validations. **a.** Distribution of total energy, the average value of the population is taken as reference and **b.** Distribution of and central dihedral of 400 initial conditions of ASR$_{AT}$-M and ASR$_{13C}$-M. In all cases a Gaussian-like distribution is achieved.

The corresponding results of subsequent excited state trajectories starting from the 400 initial conditions are displayed in Figure 3.7a. The evolution of the values of the skeletal dihedral angle representing the -C_{12}-C_{13}=C_{14}-C_{15}- reacting double bond is given in black lines. The dots showing the points where trajectories decay from S_1 to S_0 are in orange if such decay leading to photoproduct formation (reactive trajectory) or blue if back to reactant (unreactive trajectory).

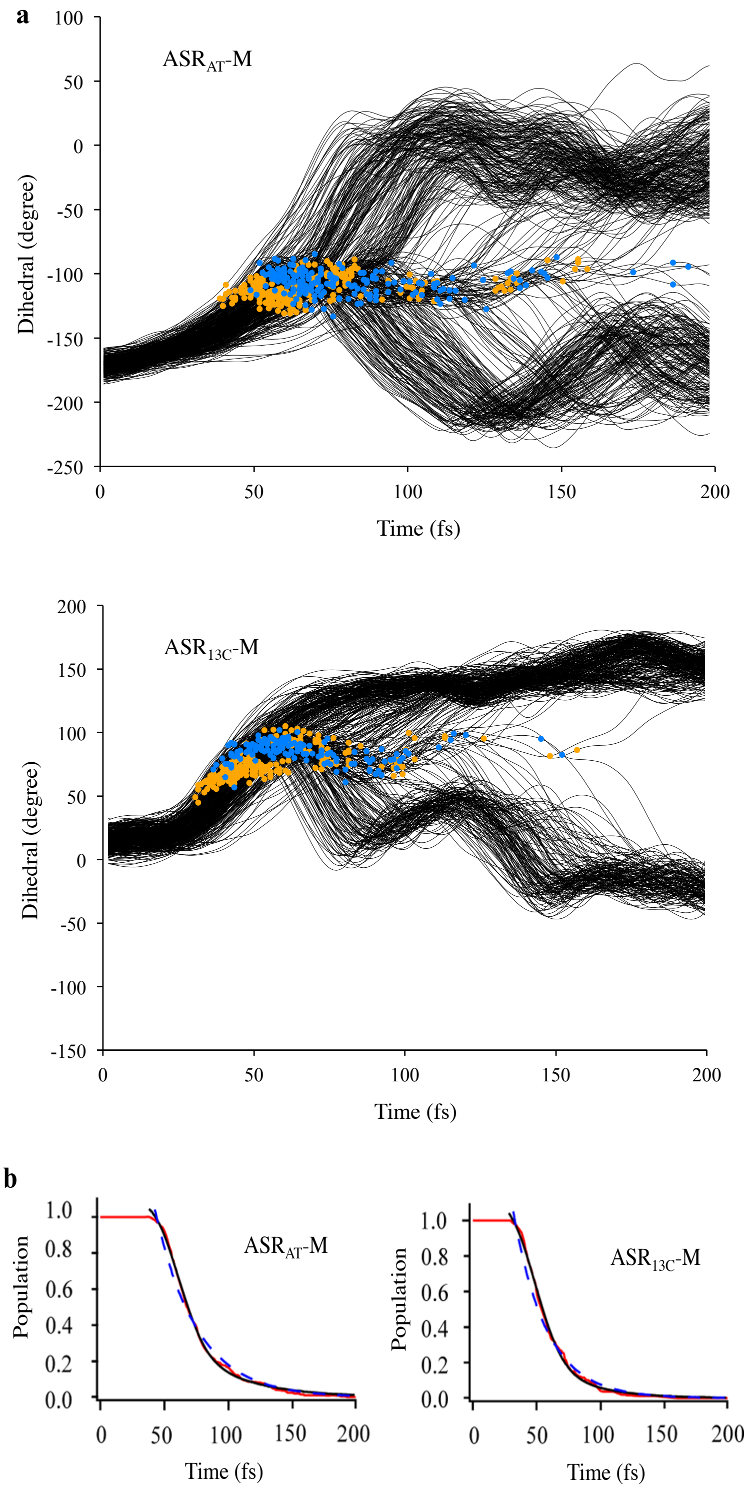

Figure 3.7 Evolution of torsional dihedral of reactive –C_{12}-C_{13}=C_{14}-C_{15}- bond and excited state lifetime fitting of 400 trajectories. **a.** Orange and blue dots indicate reactive and unreactive decay respectively. **b.** The red solid line represents the population decay and the fitting function is in blue dashed line.

From Figure 3.7a, it is obvious that ASR_{13C}-M decay relatively faster than ASR_{AT}-M. The kinetic parameters can be obtained by fitting the population decay with the following equation 3.1 and are reported in Table 3.2 together with the computed quantum yield.

$$f(t)= a_1 e^{(-\left(\frac{(t-t_1)}{t_2}\right)^2)} + y_0 + \left((1-a_1)-y_0\right) e^{(\frac{-(t-t_1)}{t_3})} \qquad (3.1)$$

where a_1 is the weight of the Gaussian decay component, y_0 is a fitting parameter, t_1 is the latency time (i.e., the time that precedes the decay onset), and t_2 and t_3 are the decay times of the Gaussian and exponential components, respectively. As shown in Figures 3.7b the Gaussian plus exponential function f(t) allows a better fit with respect to the more common biexponential function. In fact, using equation 3.1 the decay dynamics is correctly fitted with $\chi 2$ values 0.033 and 0.038, respectively. The conventional biexponential decay model would fit the computed decay dynamics less satisfactorily having corresponding χ^2 values of 0.256 and 0.269 which are higher than that of the Gaussian/exponential fit (the smaller the χ^2 value, the better the fitting), indicating a combination of Gaussian and exponential fitting could be a wise choice when describing the nonexponential decay of the ASR population. The physical meaning of these terms can be viewed as follows. The population remains on S_1 for a time t_1 before it starts to decay. A part of the population moves toward the CI quickly and decays "impulsively" according to a Gaussian function so that the corresponding "time scale" is the Gaussian decay time (t_2). The rest of the population reaches the S_1/S_0 CI more diffusively and decays exponentially (corresponds to exponential decay time t_3). The fraction of the population that remains on S_1 after 200 fs is y_0. The contribution of Gaussian (a_1) and exponential decay ($1-y_0-a_1$) to the total population decay merely depends on the nature of the S_1 potential energy surface. It is expected that the steeper the surface be the higher the Gaussian weight is. The "total" excited state lifetime (τ) is calculated as equation 3.2

$$\tau = t_1 + a_1 t_2 + (1 - a_1 - y_0) t_3 \qquad (3.2)$$

τ is therefore different from τ_{FC} used for associating a S_1 lifetime to a FC trajectory which, in turn, can be compared to the $t_1 + a_1t_2$ time. The statistical convergence of the quantum yields and kinetic parameters a_1, τ, t_1, t_2, and t_3 obtained by fitting with the function $f(t)$, is evaluated by plotting the corresponding values as a function of the number of trajectories.

Table 3.2 Fitting coefficients and quantum yield of ASR_{AT}-M and ASR_{13C}-M

Model	**a_1**	**t_1 (fs)**	**t_2 (fs)**	**t_3 (fs)**	**τ**	**χ^2**	**$t_1 + a_1t_2$ (fs)**	**quantum yield**
ASR_{AT}-M	0.465	44	27	42	80	0.038	57	0.57
ASR_{13C}-M	0.554	32	28	33	62	0.033	47	0.64

As shown in Figure 3.7 and Table 3.2, the 400-trajectory ensemble of ASR_{AT}-M and ASR_{13C}-M confirms the faster dynamics of the ASR_{13C}-M model with respect to the ASR_{AT}-M model and appears to be qualitatively consistent with the trend observed for the ASR_{13C} and ASR_{AT} FC trajectories whose results list in Table 3.1. Further analysis in the kinetic parameters indicates that the faster ASR_{13C}-M decay is justified by a shorter latency time (t_1). This reflects a faster motion of the initial ASR_{13C}-M population out of the FC region and presumably a more effective coupling with the torsional motion characterizing the evolution toward the CI. Note that the ASR_{13C}-M model decay shows a larger Gaussian weight (a_1 = 0.554), whereas in ASR_{AT}-M, the decay is more exponential like. As we also mentioned above, we attribute the Gaussian time scale to the time scale (t_2) associated with the impulsive population decay and the exponential time scale (t_3) with a following non-impulsive decay process. The faster population decay of ASR_{13C}-M and comparatively slower decay of ASR_{AT}-M are apparent when looking at the evolution of the central dihedral angle (Figure 3.7). These differences are accompanied by a reduced spreading of hop times in ASR_{13C}-M indicating a S_1 population decay more coherent than in the ASRAT-M case.

The quality of the population dynamics simulation is highly dependent on the ensemble size. For this reason, we have computed, for the ASR_{AT}-M model, two independently generated sets of 400 initial conditions (i.e., generating twice the Boltzmann-like distribution and ensuring that the molecular dynamics simulation step uses, for the two cases, different seeds). We have then compared the values obtained by computing parallel sets of 100, 200, 300, and 400 QM/MM non-adiabatic trajectories. In the following such a test is called "full-replica test". Also, in order to isolate the random effect introduced by the Tully surface-hop method, the QM/MM non-adiabatic trajectories were computed twice starting from the same Boltzmann-like distribution. In the following such a convergence test is indicated as the "Tully-replica test".

The results of the full-replica and Tully replica tests are reported in the panels of Figure 3.8. In the full-replica test the differences in quantum yields computed for the two independent trajectory sets (see Figure 3.8a) oscillate within 0.05 and appear not to converge (i.e., shift to a zero value). Thus, a sample of 400 trajectories appears to be insufficient to reach a converged quantum yield prediction within, roughly, a 0.05 precision. In contrast, the Tully replica test (see Figure 3.8c) shows quantum yields with a tendency to converge when moving from 100 to 400 trajectories. Clearly, full convergence requires a larger number of trajectories in spite of the constrained molecular environment (i.e., outside the chromophore cavity) and, therefore, a limited number of degrees of freedom with respect to the number of the degrees of freedom of the full protein. Note that in the full-replica test the difference in exponential decay time t_3 is exceptionally high (~35 fs) when a 100-trajectory ensemble is used pointing to an inability of such a set to produce converged time scales. The convergence of all time scales (t_1, t_2, t_3, and τ)

and weight (a_1) improves when moving to the 400-trajectory ensemble leading to a maximum 15 fs uncertainty and 0.4 differences in the a_1 value. The variations of lifetimes in the Tully replica test are smaller (below 5 fs) indicating a closer consistency even if there is no regular improvement with increasing of the ensemble size indicating, again, difficulties in the convergence. We conclude that a 400-trajectory ensemble provides only a semi-quantitative description of the population dynamics with expected variations above 0.05 for quantum yields, 15 fs for the time scales and 0.4 for the Gaussian weight.

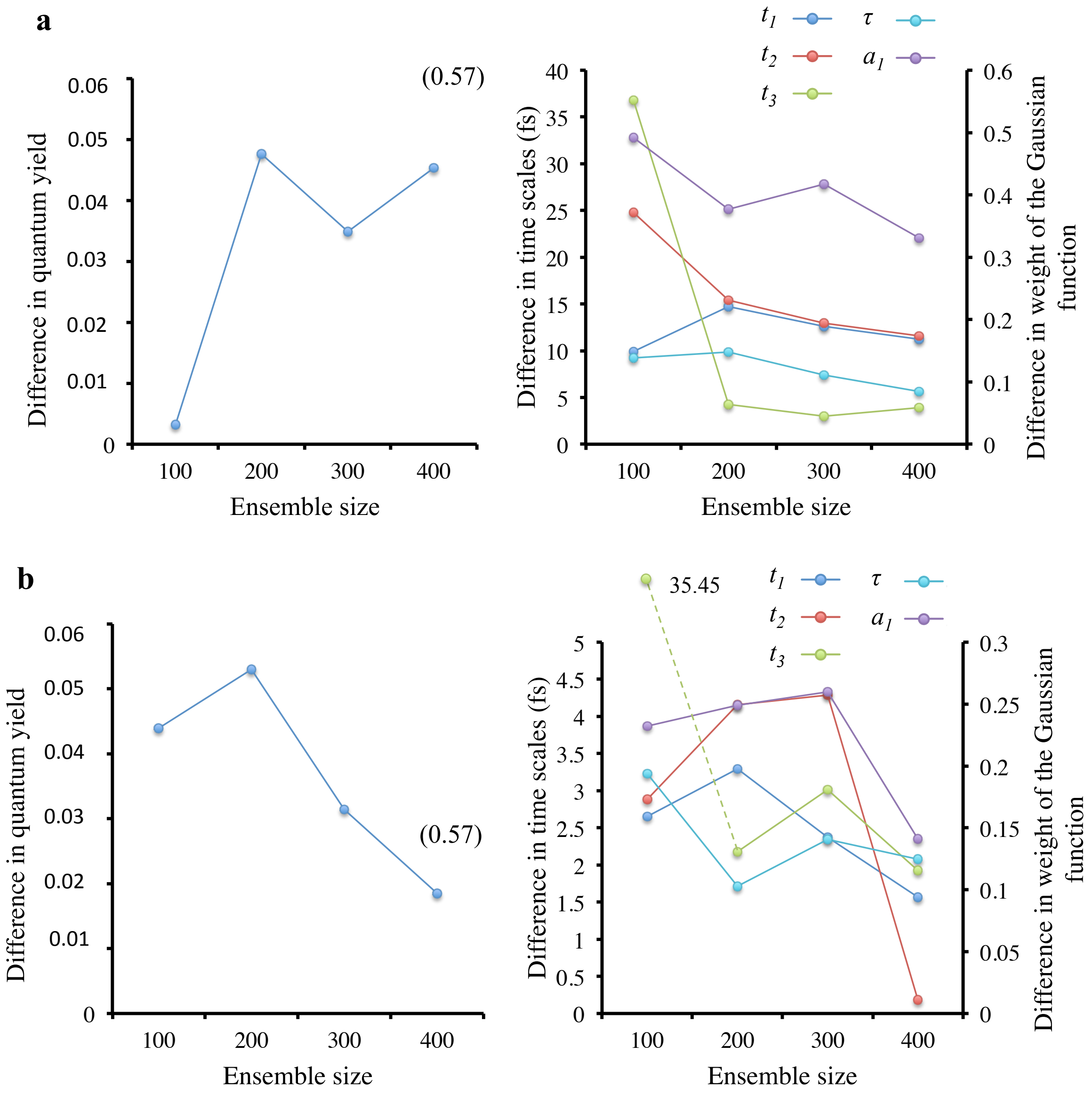

Figure 3.8 Convergence test. **a**. The full replica test and **b.** the tully replica test against the ensemble size of ASR_{AT}-M model. The reference quantum yield of ensemble size of 400 trajectories is shown in brackets of 0.57 on left side. The convergence of latency time (t_1 in blue), Gaussian decay time (t_2 in red), exponential decay time (t_3 in green), excited state lifetime (τ in cyan), and weight of the Gaussian decay (a_1 in purple) is shown on right side.

One interesting result of the population dynamics reported above is an oscillatory behavior of the reactive and unreactive decay events. The results of such analyses are given in Figure 3.9 where we display the S_1 to S_0 decay points as a function of time for both ASR$_{AT}$-M and ASR$_{13C}$-M. Accordingly, reactive decay process corresponding to trajectories evolving toward the photoproduct, and therefore contributing to a higher quantum yield, is marked in orange. The decay process leading to the reconstitution of the reactant is marked in blue. The diagrams demonstrate that for the ultrafast photoisomerizations of ASR$_{AT}$-M and ASR$_{13C}$-M quantum yields do not build up homogeneously as a function of time. In fact, it can be clearly seen that waves of reactive and nonreactive trajectories alternate each ca. 10 to 15 fs. The first oscillation starts, for both ASR$_{AT}$-M and ASR$_{13C}$-M, with a massive production of photoproducts that is rapidly followed by a wave of reactant reconstitution. This first complete reactive-unreactive cycle has a total duration of ca. 25 to 30 fs, and it is followed by a second period displaying similar features. As mentioned in Chapter I, three vibrational motions drive the photoisomerization of rhodopsins. Such oscillatory behavior is very likely induced by a vibrational motion whose period is ca. 30 fs. As we will see in Chapter IV and Chapter V this oscillatory quantum yield building is also present in Rh and the vibrational mode responsible for it is a wagging motion called hydrogen-out-of-plane (HOOP) motion.

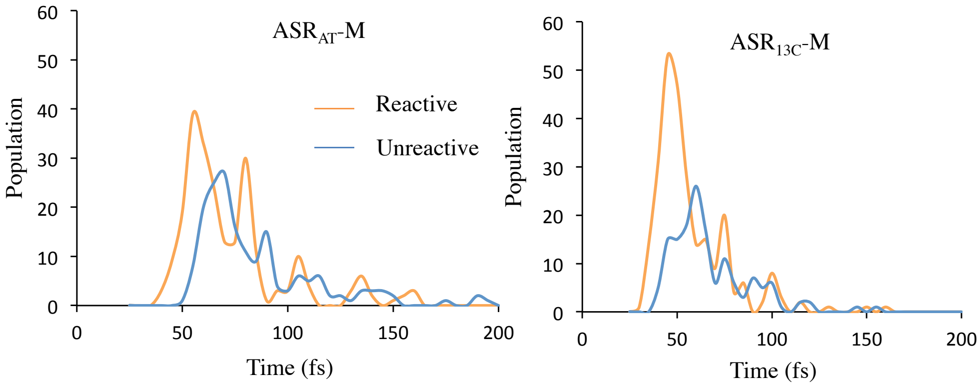

Figure 3.9 Oscillatory behavior of the excited state ensemble decay. Reactive decay is in orange and unreactive decay is in blue.

3.5 Conclusion

Above we used ASR as a benchmark system for investigating if QM/MM models built with the ARM protocol and with a PSB3 chromophore would be capable of replicating certain qualitative (i.e., mechanistic) features of the S_1 dynamics documented for ASR models with un unabridged chromophores[5,24]. We found that the bicycle-pedal photoisomerization mechanism[25] is operating in both ASR isomers. These models also support an unidirectional clockwise twisting of the $C_{13}=C_{14}$ double bond. On the other hand, as evident from the comparison of the data in Table 3.1, the ASR_{13C} and ASR_{13C}-M FC trajectories in Figure 3.4, the trajectory ensemble in Figure 3.7, and the comparison of the fitted excited state lifetimes in Table 3.2, both the absorption maxima (i.e. in terms of wavelengths) and the S_1 lifetime are, with respect to the unabridged and experimental systems, considerably reduced. This is attributed to the decrease in length of the conjugated chain of the chromophore and related increase in the S_1−S_0 energy gap and slope of the S_1 energy surface. However, in spite of the increase in slope, our dynamics studies (FC trajectories and room temperature non-adiabatic trajectories) indicate that ASR_{AT}-M has a longer S_1 lifetime with respect to ASR_{13C}-M, in line with the trends documented for the unabridged ASR models and, also, with the experimental observations. This is valid in spite of the demonstrated convergence issue of the kinetic parameters (with our 400 trajectory ensembles).

In contrast, with the conclusions above, the computed trend in isomerization quantum yields indicates that the faster ASR_{13C}-M affords a higher quantum yield at variance with the observed experimental trend. On the other hand, the computed trend appears consistent with the reported hypothesis of a direct proportionality[26,27] between the reaction speed and the quantum yield: an idea based on a simple Landau−Zener model[28,29] for the ultrafast decay. In order to further investigate the origin of the computed quantum yield trend we have “decomposed” the ensemble populations in reactive and nonreactive trajectories. The preliminary results of Figure 3.9 clearly indicate that the quantum yield value is generated through a relatively complex process displaying oscillatory time features. At this stage it is therefore concluded that the familiar Landau−Zener decay picture for ultrafast decay is therefore too simplistic for even a qualitative discussion of quantum yield trends (at least in double bond isomerizations). Indeed, in the following Chapter IV, we employ the population dynamics protocol benchmarked in the present chapter with a QM/MM models of Rh featuring a reduced retinal chromophore to propose a correlation between the outcome of a trajectory (reactive/unreactive) and the vibrational phase of a certain specific HOOP vibrational mode at CI.

3.6 References

(1) Melaccio, F.; del Carmen Marín, M.; Valentini, A.; Montisci, F.; Rinaldi, S.; Cherubini, M.; Yang, X.; Kato, Y.; Stenrup, M.; Orozco-Gonzalez, Y.; et al. *J. Chem. Theory Comput.* **2016**, *12* (12), 6020–6034.

(2) Schapiro, I.; Ryazantsev, M. N.; Frutos, L. M.; Ferré, N.; Lindh, R.; Olivucci, M. *J. Am. Chem. Soc.* **2011**, *133* (10), 3354–3364.

(3) Gozem, S.; Luk, H. L.; Schapiro, I.; Olivucci, M. *Chem. Rev.* **2017**, *117* (22), 13502–13565.

(4) Luk, H. L.; Melaccio, F.; Rinaldi, S.; Gozem, S.; Olivucci, M. *Proc. Natl. Acad. Sci.* **2015**, *112* (50), 15297–15302.

(5) Strambi, A.; Durbeej, B.; Ferre, N.; Olivucci, M. *Proc. Natl. Acad. Sci. U. S. A.* **2010**, *107* (50), 21322–21326.

(6) Kawanabe, A.; Furutani, Y.; Jung, K.-H.; Kandori, H. *J. Am. Chem. Soc.* **2007**, *129* (27), 8644–8649.

(7) Cheminal, A.; Leonard, J.; Kim, S.-Y.; Jung, K.-H.; Kandori, H.; Haacke, S. *Phys. Chem. Chem. Phys.* **2015**, *17* (38), 25429–25439.

(8) Cheminal, A.; Leonard, J.; Kim, S. Y.; Jung, K.-H.; Kandori, H.; Haacke, S. *Chem. Phys. Lett.* **2013**, *587*, 75–80.

(9) Wand, A.; Rozin, R.; Eliash, T.; Jung, K.-H.; Sheves, M.; Ruhman, S. *J. Am. Chem. Soc.* **2011**, *133* (51), 20922–20932.

(10) Schapiro, I.; Ruhman, S. *Biochim. Biophys. ACTA-BIOENERGETICS* **2014**, *1837* (5, SI), 589–597.

(11) Ruckenbauer, M.; Barbatti, M.; Mueller, T.; Lischka, H. *J. Phys. Chem. A* **2013**, *117* (13), 2790–2799.

(12) Valsson, O.; Filippi, C. *J. Chem. Theory Comput.* **2010**, *6* (4), 1275–1292.

(13) Gozem, S.; Huntress, M.; Schapiro, I.; Lindh, R.; Granovsky, A. A.; Angeli, C.; Olivucci, M. *J. Chem. Theory Comput.* **2012**, *8* (11), 4069–4080.

(14) Gozem, S.; Melaccio, F.; Valentini, A.; Filatov, M.; Huix-Rotllant, M.; Ferre, N.; Manuel Frutos, L.; Angeli, C.; Krylov, A. I.; Granovsky, A. A.; et al. *J. Chem. Theory Comput.* **2014**, *10* (8), 3074–3084.

(15) Aquilante, F.; De Vico, L.; Ferre, N.; Ghigo, G.; Malmqvist, P.-A.; Neogrady, P.; Pedersen, T. B.; Pitonak, M.; Reiher, M.; Roos, B. O.; et al. *J. Comput. Chem.* **2010**, *31* (1), 224–247.

(16) Ponder, J. W.; Richards, F. M. *J. Comput. Chem.* **1987**, *8* (7), 1016–1024.

(17) Ferre, N.; Angyan, J. G. *Chem. Phys. Lett.* **2002**, *356* (3–4), 331–339.

(18) Tully, J. C.; Preston, R. K. *J. Chem. Phys.* **1971**, *55* (2), 562–572.

(19) Tully, J. C. *J. Chem. Phys.* **1990**, *93* (2), 1061–1071.

(20) Vreven, T.; Bernardi, F.; Garavelli, M.; Olivucci, M.; Robb, M. A.; Schlegel, H. B. *J. Am. Chem. Soc.* **1997**, *119* (51), 12687–12688.

(21) Weingart, O.; Migani, A.; Olivucci, M.; Robb, M. A.; Buss, V.; Hunt, P. *J. Phys. Chem. A* **2004**, *108* (21), 4685–4693.

(22) Granucci, G.; Persico, M. *J. Chem. Phys.* **2007**, *126* (13), 134114.

(23) Pronk, S.; Páll, S.; Schulz, R.; Larsson, P.; Bjelkmar, P.; Apostolov, R.; Shirts, M. R.; Smith, J. C.; Kasson, P. M.; van der Spoel, D.; et al. *Bioinformatics* **2013**, *29* (7), 845–854.

(24) Schapiro, I.; Ruhman, S. *Biochim. Biophys. Acta - Bioenerg.* **2014**, *1837* (5), 589–597.

(25) Warshel, A.; Levitt, M. *J Mol Biol* **1976**, *103* (2), 227–249.

(26) Weiss, R. M.; Warshel, A. *J. Am. Chem. Soc.* **1979**, *101* (20), 6131–6133.

(27) Schoenlein, R.; Peteanu, L.; Mathies, R.; Shank, C. *Science (80-.).* **1991**, *254* (5030), 412–415.

(28) Zener, C. *Proc. R. Soc. A Math. Phys. Eng. Sci.* **1932**, *137* (833), 696–702.

(29) Kim, J. E.; Tauber, M. J.; Mathies, R. A. *Biophys. J.* **2003**, *84* (4), 2492–2501.

3.7 Supplementary figure

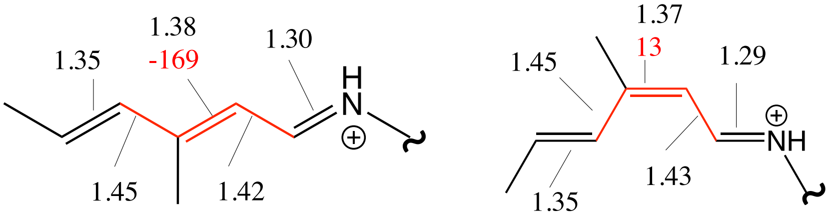

ASR$_{AT}$-M in protein

ASR$_{13C}$-M in protein

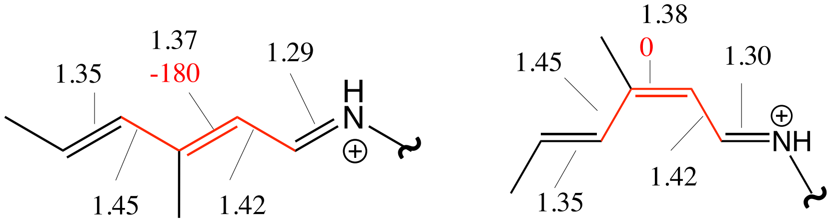

ASR$_{AT}$-M in gas-phase

ASR$_{13C}$-M in gas-phase

Figure S3.1 S_0 equilibrium structure for ASR$_{AT}$-M and ASR$_{13C}$-M models. Bond lengths (black) are in Angstroms and dihedral (red) is in degree.

3.8 Chapter copyrights

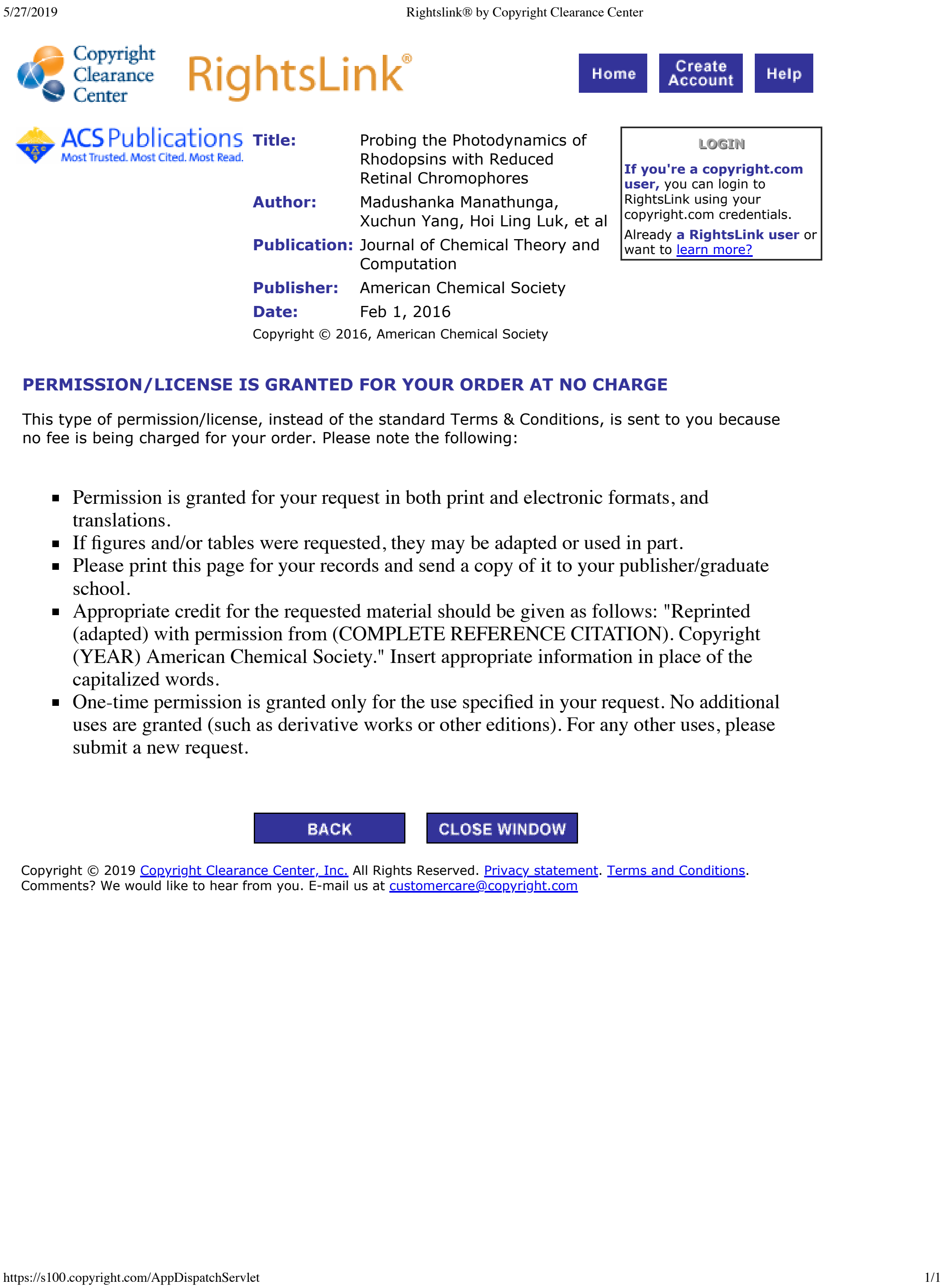

5/27/2019 Rightslink® by Copyright Clearance Center

Title: Probing the Photodynamics of Rhodopsins with Reduced Retinal Chromophores

Author: Madushanka Manathunga, Xuchun Yang, Hoi Ling Luk, et al

Publication: Journal of Chemical Theory and Computation

Publisher: American Chemical Society

Date: Feb 1, 2016

Copyright © 2016, American Chemical Society

LOGIN

If you're a copyright.com user, you can login to RightsLink using your copyright.com credentials.

Already **a RightsLink user** or want to learn more?

PERMISSION/LICENSE IS GRANTED FOR YOUR ORDER AT NO CHARGE

This type of permission/license, instead of the standard Terms & Conditions, is sent to you because no fee is being charged for your order. Please note the following:

- Permission is granted for your request in both print and electronic formats, and translations.
- If figures and/or tables were requested, they may be adapted or used in part.
- Please print this page for your records and send a copy of it to your publisher/graduate school.
- Appropriate credit for the requested material should be given as follows: "Reprinted (adapted) with permission from (COMPLETE REFERENCE CITATION). Copyright (YEAR) American Chemical Society." Insert appropriate information in place of the capitalized words.
- One-time permission is granted only for the use specified in your request. No additional uses are granted (such as derivative works or other editions). For any other uses, please submit a new request.

Copyright © 2019 Copyright Clearance Center, Inc. All Rights Reserved. Privacy statement. Terms and Conditions.
Comments? We would like to hear from you. E-mail us at customercare@copyright.com

https://s100.copyright.com/AppDispatchServlet 1/1

This Chapter, in part, reused the content of the jounarl article:

“Manathunga, M.; Yang, X.; Luk, H. L.; Gozem, S.; Frutos, L. M.; Valentini, A.; Ferrè, N.; Olivucci, M. *J. Chem. Theory Comput.* **2016**, *12 (2)*, 839–850.”

with permission from

Dr. Madushanka Manathunga, Dr. Hoi Ling Luk, Dr. Samer Gozem, Dr. Luis Manuel Frutos, Dr. Alessio Valentini, Dr. Nicolas Ferrè, Dr. Massimo Olivucci

CHAPTER IV. THE PHOTOISOMERIZATION REACTIVITY OF BOVINE RHODOPSIN IS VIBRATIONAL-PHASE DEPENDENT

This Chapter is, *in part,* reproduced with permission from Schnedermann, C.; Yang, X.; Liebel, M.; Spillane, K. M.; Lugtenburg, J.; Fernández, I.; Valentini, A.; Schapiro, I.; Olivucci, M.; Kukura, P.; and Mathies, R. A. *Nat Chem*. **2018**, *10*, 449-455.

4.1 Abstract

Vibronic coupling is key to efficient energy flow in molecular systems and a critical component of most mechanisms invoking quantum effects in biological processes. Despite increasing evidence for coherent coupling of electronic states being mediated by vibrational motion, it is not clear how and to what degree properties associated with vibrational coherence such as phase and coupling of atomic motion can impact the efficiency of light-induced processes under natural, incoherent illumination. Here, we show, using a mixed computational and experimental approach, that deuteration of the H_{11}-C_{11}=C_{12}-H_{12} double bond of the rPSB11 chromophore in the visual pigment bovine rhodopsin significantly and unexpectedly alters the photoisomerization yield while inducing smaller changes in the ultrafast isomerization dynamics. The semi-classical (non-adiabatic) molecular dynamics simulations reveal correlation between the photoisomerization photoproduct formation and the phase of a specific vibrational mode at the decay point (i.e. at a CI or in its strict vicinity). The observed isotopic impact on the photoisomerization quantum yield is then interpreted as a modulation of such vibrational phase.

4.2 Introduction

As mentioned in Chapter I, the photoisomerization of Rh is classified as vibrational coherent internal conversion processes through a CI allowing for the rapid formation of isomerized photoproduct irrespective of the illumination conditions[1–7]. A key question that remains unanswered is whether this coherence is functionally significant. Highly time-resolved transient-grating studies of Rh recently reported the sub-50 fs appearance of photoproduct and extracted short lifetime oscillatory vibrational features assigned to the transient excited state[7,8]. These observations suggest that the vibrational motion of key modes that make up the isomerization coordinate, like the torsional twisting at the isomerizing C=C double bond (α) and hydrogen-out-of-plane motion (described by the "deviation from planarity" coordinate δ_{op}) could be an important factor in determining the efficiency and outcome of the reaction (definition of α and δ_{op} coordinate is shown in Figure 1.2a). Furthermore, molecular dynamics simulations of the Rh surface crossing have proposed that the phase of vibrational motions upon encountering the CI connecting the excited and ground electronic states is important for the reactivity[2–4,9–14]. In particular, recent theoretical studies on the isomerization dynamics of Rh have emphasized that the degree of vibrational coherence plays a crucial role for the quantum yield of photoproduct formation[15,16]. Despite multiple indications that the relative phase of vibrational modes may be important in Rh photochemistry[2,14,17], there is no direct evidence suggesting its relevance, for the chemical outcome, in particular biologically relevance, incoherent excitation.

An informative means to test the reactive influence of vibrational modes and their phase relationship at the CI involves isotopic labeling. Isotopes have traditionally been employed to study reaction mechanisms through primary kinetic isotope effects such as in the light-driven proton transfer in green-fluorescent protein[18,19]. In the context of visual photochemistry, early studies on visual photochemistry suggested a primary kinetic isotope effect associated with chromophore proton or hydrogen transfer, but these models have not been sustained[20,21].

To examine the effect of isotopic substitution on the photochemistry of vision, our experimental collaborators synthesized three modified 11-*cis* retinal analogues (11-D, 12-D and 11,12-D_2) and regenerated these chromophores in the opsin protein (Figure 4.1). They then measured the isomerization quantum yield using a continuous-wave light source and the isomerization kinetics by recording the dynamic appearance of the photoproduct using ultrafast transient absorption spectroscopy[22]. While isotopic substitution caused only a modest effect (within the experimental error) on the photoisomerization kinetics, they observed a large effect on the photochemical quantum yield, which is dictated by the efficiency of internal conversion through the CI from the rPSB11 reactant to the rPSBAT photoproduct.

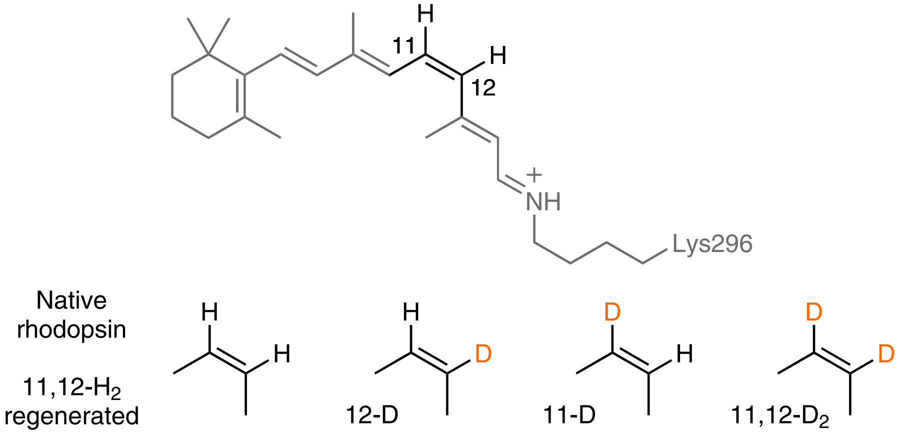

Figure 4.1 Native and isotopically labeled rPSB11.

More specifically, they proposed that the time difference between the photoproduct formation and probe pulses provide an internally referenced measure of the lag time for photoproduct formation. The retrieved average lag time is 150.6 ± 5.2 fs and the individual traces show subtle variations across the isotopomers (Figure 4.2a). Native and 11,12-H_2 regenerated Rh are expected to show the same value but differ by 3.2 fs, which could be attributed to systematic errors. The lag time for 11,12-D_2 increases by 9.1 fs and the 11-D isotopomer exhibits similar dynamics to 11,12-D_2 (increase by 7.3 fs), while the 12-D is indistinguishable from native Rh. In contrast to the minor effect on the photoisomerization kinetics, the isotopic substitution has a significant effect on the photochemical quantum yield (Figure 4.2b). The native and 11,12-H_2 regenerated Rh exhibits statistically indistinguishable isomerization quantum yields of 0.63 and 0.65, respectively, demonstrating that retinal regeneration did not alter the system. The 11,12-D_2

derivative exhibits a quantum yield of 0.69, which is higher compared to the native (6%) and regenerated (4%) chromophore. In contrast, the 11-D and 12-D isotopomers, with just a single isotopic substitution, have substantially lower quantum yields of 0.45 and 0.48, respectively. This extraordinary yield reduction as well as the increase for 11,12-D_2 is statistically significant beyond experimental error. The rPSB11 in solution exhibits an even lower quantum yield of 0.19 outside the protein pocket[23]. These results evidence an anomalous isotope effect where symmetric deuteration of the isomerizing bond produces a higher isomerization quantum yield while asymmetric isotopic substitution significantly lowers the yield.

The above experiment suggests a weak dependence of the photochemical dynamics upon isotopic substitution manifested in the delayed appearance (lag time) of the photoproduct formation for deuterated isotopes relative to native Rh. This delay is correlated with the degree of isotopic substitution and is expected based on mixing of the δ_{op} and α motions whose frequency primarily determines the time it takes to reach the CI. Critically, the variations in dynamic parameter are small compared with the changes in isomerization quantum yield that ranges from -30% to +8%. Also, there appears to be no correlation between the extracted kinetic parameters and the isomerization quantum yield, suggesting a novel isotope effect where mass induced changes in vibrational phase and thereby mode specific vibrational coupling alter the reaction efficiency of a vibronically coherent photochemical reaction.

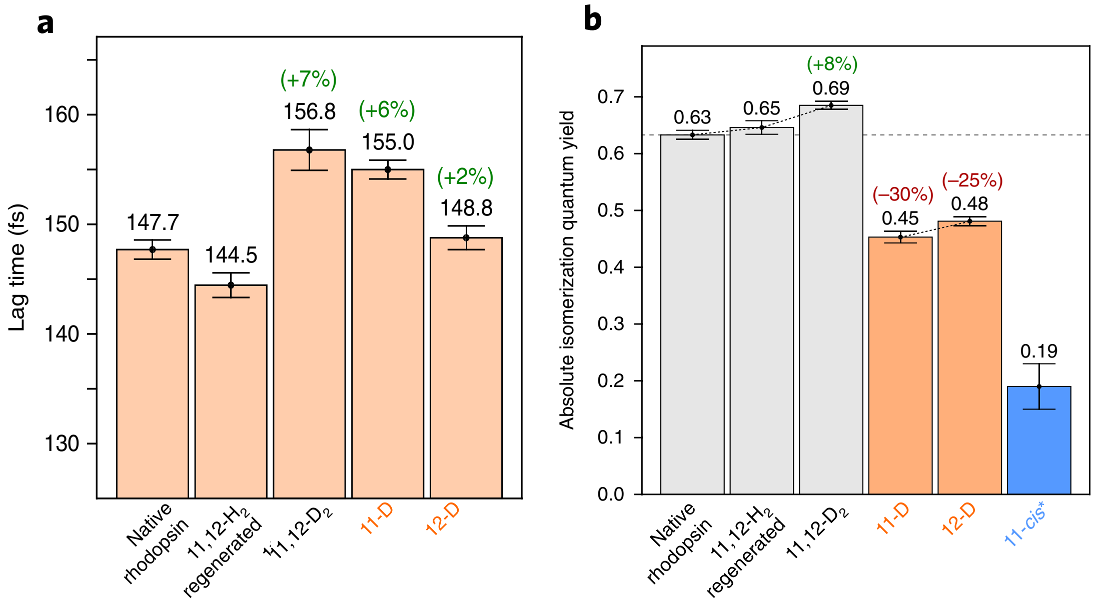

Figure 4.2 Lag time and quantum yield for native, 11,12-H_2 regenerated deuterated retinal chromophore. **a.** Retrieved lag (or delay) time before photoproduct formation. All error bars refer to one standard deviation and range from 0.5 to 1.2%. The percentage differences between the average lag time of the native and regenerated Rh and the specified isotopically labeled chromophores are also shown. **b.** Grey, symmetrically substituted; orange, asymmetrically substituted. The quantum yields are compared to the free chromophore in methanol solution (blue, *). The percentage differences between the average quantum yield of the native and regenerated Rh and the specified isotopically labeled chromophores are also shown. All error bars refer to one standard deviation and range from 1 to 2%for the studied isotopomers.

These results can be understood by adopting a vibrationally coherent picture of Rh's reactive internal conversion, which considers the nature and relative timing and phasing of the various atomic motions within a single molecule. The extremely rapid isomerization event reduces the overall reaction coordinate in Rh to critical displacements along a localized backbone α and δ_{op} motions, with surface hopping restricted to a relatively narrow range of torsional angles around -90 degrees. A local isomerizing twist about the C_{11}=C_{12} double bond is achieved through a correctly phased motion of the -C_{10}-C_{11}=C_{12}-C_{13}- torsion and the corresponding anti-symmetric H-C_{11}=C_{12}-H torsion, related to the δ_{op} coordinate, at the CI. A successful isomerization reaction thus requires a cooperative effect of both vibrational degrees of freedom in a well-defined manner.

To obtain deeper insight into the phase relationship and role of these modes, we carried out population dynamics simulations for all studied isotopomers using a QM/MM Rh model featuring a computationally more affordable five double-bond chromophore (Figure 4.4) and semi-classical trajectories. The excited-state lifetime and quantum yield of each isotopomer were computed by propagating 400 trajectories starting with initial conditions corresponding to a room temperature Boltzmann distribution. The simulated quantum yields parallel the experimentally observed isotope-dependent trend, and reproduce observed the isotope-independent trend in the lag times. The details of the computational methods, results and discussion relative to the research effort summarized above are presented in following sections.

4.3 Methods

4.3.1 QM/MM model generation and validation

The QM/MM model of Rh was constructed starting from its 2.2 Å resolution crystallographic structures (PDB code: 1U19)[24] following the protocol as reported in Chapter II and III but using a different and less approximate retinal chromophore obtained from a model featuring the full chromophore.

We now briefly outline the Rh model construction (see Figure 4.3) that starts with the preparation of a QM/MM model featuring the full chromophore. In such model, the 11-*cis* retinylidene, NH and CεH3 atoms linked to the C_δ atom of the Lys296 side-chain form the QM subsystem. This is described at the CASSCF level of theory[25] with a 12 electrons in 12 orbitals active space, which comprises the entire π-system of the moiety. The rest of the protein forms the MM subsystem. This is described by a modified AMBER94 force field featuring specific parameters for the Lys296 side-chain[26–28]. The interaction between the MM and QM subsystems is described at the electrostatic embedding level using the ESPF concept[29]. The Lys296 and all the side-chains or waters with at least one atom within 4 Å from any atom of the chromophore are flexible. A consistent model was also constructed for the bathorhodopsin (bathoRh) photoisomerization product featuring the all-*trans* retinylidene chromophore. As shown in Table 4.1, the models reproduce the observed trend of the absorption maxima.

Table 4.1 Computed and experimental vertical excitation energies (ΔE_{S1-S0}) from S_0 to S_1 and corresponding λ^{a}_{max} values

Model	Comput. $\Delta E_{S_1-S_0}$ kcal/mol (nm)	Observed $\Delta E_{S_1-S_0}$ kcal/mol (nm)[30]
Rh	57.1 (501)	57.4 (498)
bathoRh	55.8 (512)	54.0 (529)
PSB5-Rh	63.0 (454)	
PSB5-bathoRh	60.3 (474)	

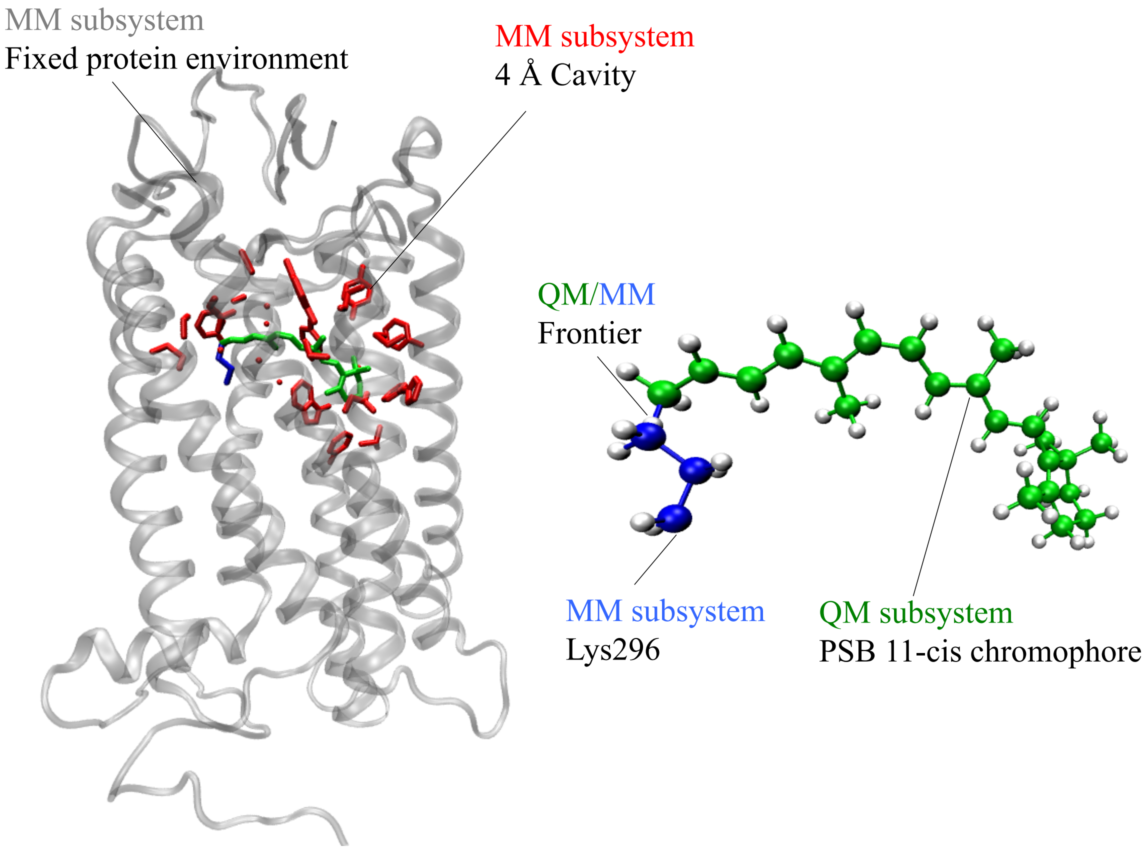

Figure 4.3 Rh QM/MM model. The QM subsystem is colored in green (C and N atoms) and silver (H atoms connected to green atoms). The MM subsystem components are colored in grey (fixed atoms displayed in ribbon representation), in red (flexible cavity side-chains), in blue (flexible Lys296 side-chain) and in silver (H atoms connected to the blue atoms). The 'Frontier label' points to the H link-atom, which is part of the QM subsystem.

The construction of the less expensive QM/MM model with an abridged retinal chromophore (PSB5-Rh model) is performed taking as a template structure the full chromophore model described above. As shown in Figure 4.4, the 4 Å flexible cavity was redefined to include a five-double-bond backbone (PSB5) chromophore featuring an active space comprising 10 π-electrons in 10 π-orbitals. The vertical excitation energies for the equilibrium structures of the Rh and PSB5-Rh models were computed at the CASPT2 level of theory[31]. As shown in Table 4.1, the resulting PSB5-Rh model displays an excitation energy that is only 6 kcal/mol blue shifted with respect to the unabridged model mainly due to the rather out of plane twisted β-ionone ring of the full chromophore. Furthermore, PSB5-Rh and PSB5-bathoRh display the same vertical excitation energy trend of the corresponding Rh and bathoRh models with the unabridged chromophore.

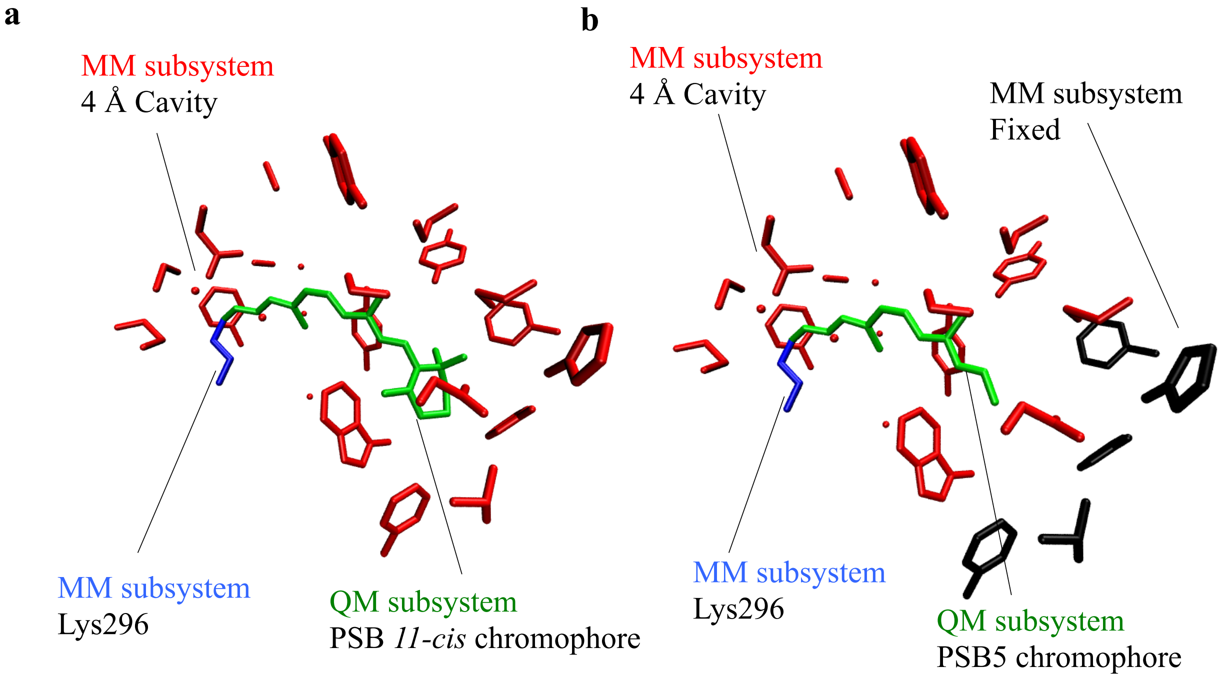

Figure 4.4 Cavities of the Rh and PSB5-Rh models. **a**. Cavity of the Rh model. **b**. Cavity of the reduced PSB5 chromophore. The chromophores are in green, the chromophore bound Lys296 is in blue, and the cavity side-chains are in red. The PSB5-Rh model side-chains originally belonging to the Rh model cavity but located outside the PSB5-Rh cavity are shown in black and were kept frozen during the computations

4.3.2 Initial conditions generation and population dynamics simulation

For each isotopomer (11,12-H_2, 11,12-D_2, 11D and 12D) of the PSB5-Rh model, a Boltzmann-like distribution of 400 initial conditions (geometries and velocities) was generated following the protocol reported in Chapter III. The quality of the computed Boltzmann-like distribution was evaluated by plotting the total energy, the vertical excitation energy $\Delta E_{S0\text{-}S1}$ value at CASSCF level and distribution of α and δ_{op} coordinates. The diagrams in Figure 4.5 show the expected Gaussian-like shape. The same result was obtained for each PSB5-Rh isotopomer model and the obtained initial conditions (geometries and velocities) where used to launched 400 semi-classical trajectories where the surface hop is decided by a stochastic parameter according to the Tully surface-hop method. The trajectories were propagated for 200 fs.

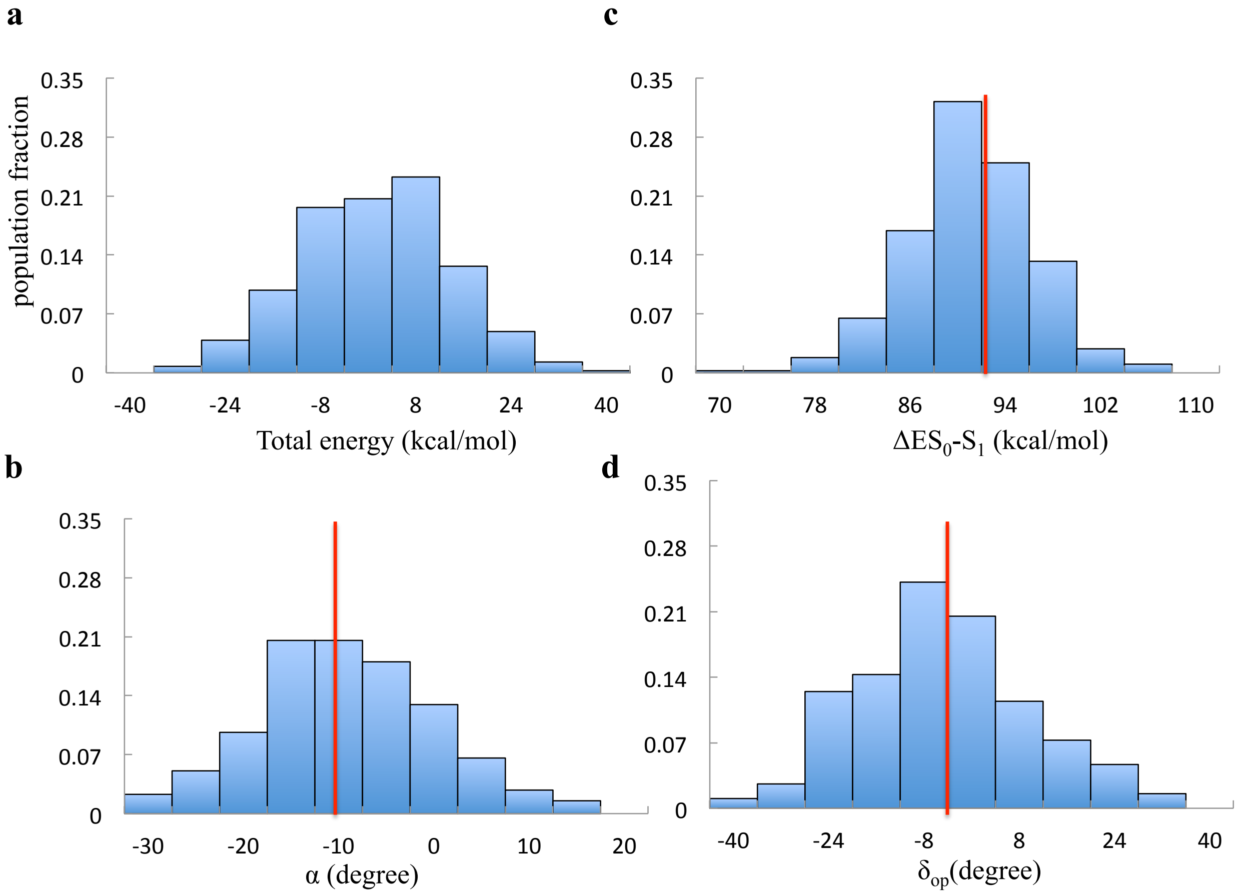

Figure 4.5 Initial condition validations. **a.** Distribution of relative total energy. The average value is taken as reference. **b**. Distribution of vertical excitation energy. **c**. Distribution of α coordinates **d.** Distribution of δ_{op} coordinates. All plots are from the PSB5-Rh model with hydrogens at positions C_{11} and C_{12} (11,12-H_2 Rh-PSB5 model). The vertical red line represents corresponding value at the S_0 equilibrium structure.

4.4 Results and discussion

4.4.1 Analysis of the population dynamics

As also mentioned above, we obtained the simulated excited-state lifetime and quantum yield of each isotopomer by propagating 400 room temperature semi-classical trajectories on the first electronically excited state S_1. The results of our simulations agree with the experimentally observations (see section 4.2). More specifically, the simulation reproduced the observed quantum yields trend (increase for 11,12-D_2, decrease for 11-D and 12-D) as well as the observed weak isotope dependent trend in photoisomerization kinetics (Table 4.2).

Table 4.2 Experimental and simulated results

		11,12-H_2[a]	**11,12-D_2**	**11-D**	**12-D**
Experiment	Lab time (fs)	147.7 ± 1.0	156.8 ± 1.9	155.0 ± 0.9	148.8 ± 1.1
	Quantum yield	0.63 ± 0.01	0.69 ± 0.01	0.45 ± 0.02	0.48 ± 0.01
Simulation	Hop time[b] (fs)	100 ± 31	113 ± 41	100 ± 35	93 ± 35
	Quantum yield	0.69	0.70	0.61	0.58

All indicated errors refer to one standard deviation. [a]Experimental values for native Rh. [b]Average hop time.

Motivated by this agreement between experiment and theory, we investigated the simulated trajectories to extract general trends for all isotopomers governing the underlying mechanisms. In all isotopmers we observed an oscillatory behavior showing initially alternating 'reactive' (formation of *trans*-photoproduct) and 'unreactive' (formation of *cis*-reactant) waves associated with different subsets of the decaying population (Figure 4.6b). The subsets corresponded to distinct phases of the α and δ_{op} modes. It is instructive to define an effective coordinate $\tau = \alpha - \delta_{op}/2$, which is assumed to be (geometrically) proportional to the overlap between the two π-orbitals involved in the breaking and reconstitution of the C_{11}=C_{12} double bond (Figure 4,6a). We found that the ‘reactive’ or ‘unreactive’ direction is best described by considering the τ velocity ($d\tau/dt$) at CI where a negative τ velocity leads to photoproduct rPSBAT formation (Figure 4.6c, orange) while a positive τ velocity results in reactant rPSB11 formation (Figure 4.6c, blue). After examining the individual α, δ_{op} components of the τ motions, we see that the α velocity ($d\alpha/dt$) component behave in a similar way in the reactive and unreactive trajectories. This means that rendering the velocity of δ_{op} ($d\delta_{op}/dt$) the decisive factor determining the sign of the τ velocity and therefore the reactivity of each specific trajectory. As highlighted in Figure 4.6d, reactive and unreactive trajectories approach the CI at approximately the same α velocity in both cases negative (α is moving towards more negative values). Successful photoproduct formation occurs when δ_{op} moves in the opposite direction to α, namely when $d\delta_{op}/dt$ is positive. This leads to a counterclockwise skeletal twisting motion (orange trajectory) after the hop. Reactant formation is observed if δ_{op} moves in the same direction as α, that is, towards more negative values (blue trajectory).

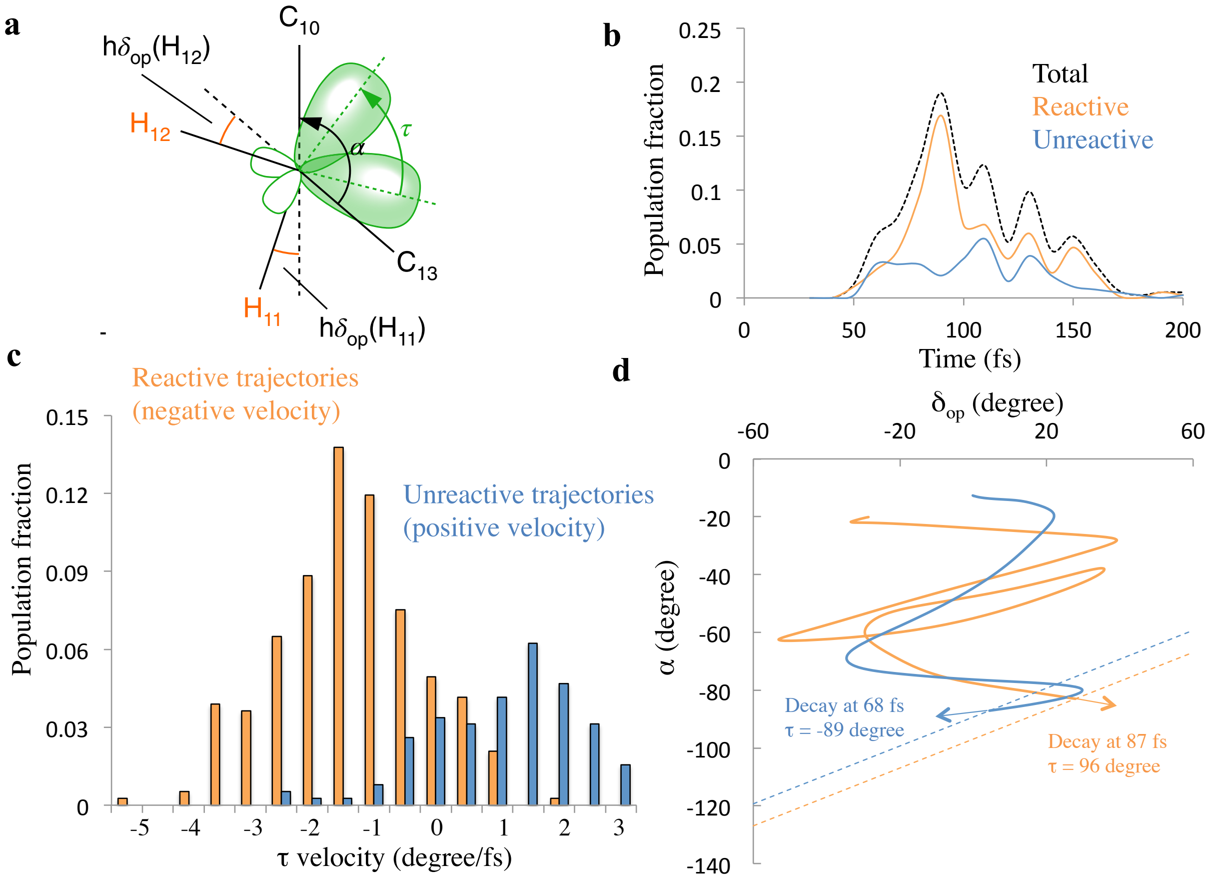

Figure 4.6 Simulated excited-state isomerization dynamics of Rh. **a.** The relationship between the 'overlap' coordinate (τ) and the π-orbitals responsible for double-bond reconstitution is schematically illustrated on the right. $h\delta_{op}$ (H_{11}) is defined as the dihedral angle between the H_{11}-C_{11}-C_{12} and C_{10}-C_{11}-C_{12} planes and $h\delta_{op}$ (H_{12}) is defined as the dihedral angle between the H_{12}-C_{11}-C_{12} and C_{11}-C_{12}-C_{13} planes in such a way that the relationship $\delta_{op} = h\delta_{op}(H_{11}) + h\delta_{op}(H_{12})$ is satisfied. **b.** Oscillatory character of the excited-state population decay for both the reactive and unreactive sub-populations. **c.** Distribution of the τ velocities at the decay point (CI) for the reactive and unreactive sub-populations. Negative and positive τ velocities correlate with reactive (orange) and unreactive (blue) events, respectively. **d.** Representative reactive and unreactive trajectories showing that the sign of the τ velocity is determined by the sign of the δ_{op} velocity. The two straight dashed lines give the corresponding values of τ for the reactive (orange) and unreactive (blue) trajectory.

4.4.2 Analysis of α and δ_{op} modes

We plotted the time evolution of excited α and δ_{op} modes of 400 trajectories for each isotopomer. The α mode of all four isotopomers shared similar progression that starts around 10-15 fs and proceed coherently with a counterclockwise -C_{10}-C_{11}=C_{12}-C_{13}- skeletal motion (Figure 4.7). Around -50 degree twisting and 40 fs delay, one can detect a bifurcation, which causes part of the population to change the direction of skeletal twisting (from counterclockwise to clockwise) and go back towards a α values close to the ones of the initial vertical excited population. The bifurcation causes a partial inversion in the C11=C12 twisting progression on the excited state and its role is discussed in details in Chapter V. At delays from 70-90 fs the branch of the population continuing the counterclockwise torsional motion in the forward direction reaches ca. -90 degrees twisting while the branch reverting the twisting direction reaches values close to the vertical excited value (-15 degrees). This second branch then re-invert the direction of torsional motion and reaches -90 degrees around 100–110 fs delay.

At variance with the α mode, the δ_{op} mode shows different, but not bifurcating, progressions among the four isotopomers. Its period is found to be monotonically increasing with the degree of isotope substitution (Figure 4.8b). In the 12-D isotopomer one sees a decrease in the amplitude of the oscillations that may be associated with the differences in excited state carbocationic vs. carbenic electronic structures at C_{11} and C_{12} respectively (see Figure 4.8a) and, as a consequence, on the different forces acting on H_{11} and H_{12}.

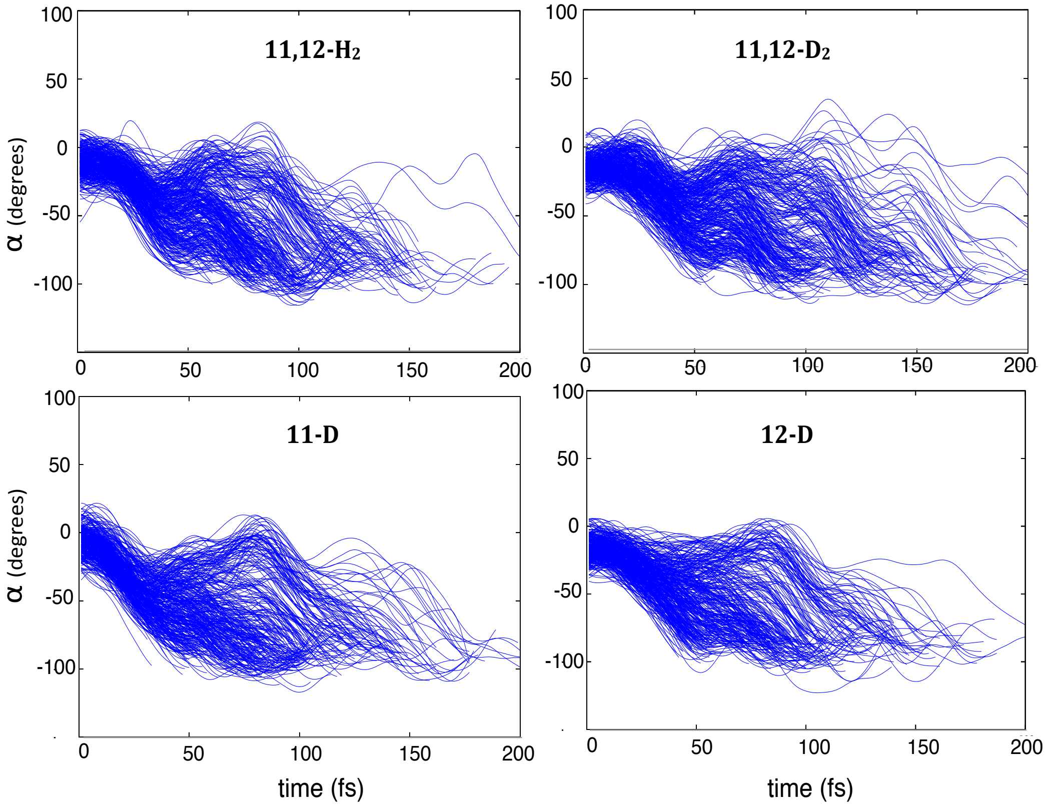

Figure 4.7 Time evolution of α motion of each isotopomers.

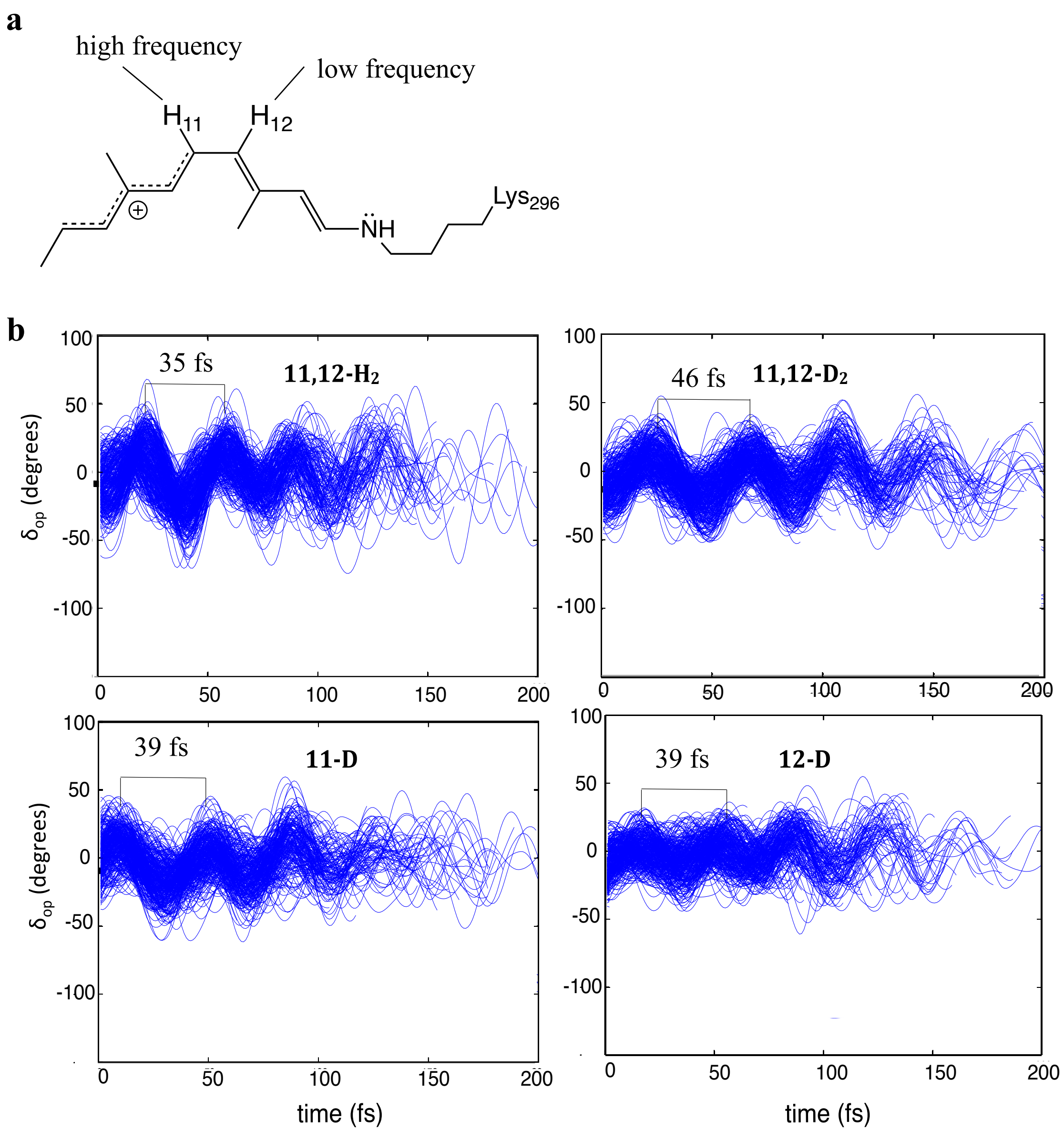

Figure 4.8 Time evolution of δ_{op} motion of each isotopomers. **a.** Different H_{11} and H_{12} wags behavior (notice the 'charge transfer' electronic structure characterizing the excited state) **b.** Comparison of the δop changes and periods (frequencies) between the 400 excited-state trajectories of each isotopomer.

Following above findings, we can now reconcile the discrepancy arising between the modest changes in reaction rates and the non-monotonous trend in isomerization quantum yields for Rh isotopomers. Partial deuteration of the retinal backbone has only a small effect on the torsional mode progression and consequently on the movement of the ground and excited electronic states towards the CI, since the torsion is predominantly localized on the carbon framework. Because the surface hopping probability is directly linked to the evolution of this torsion to values close to -90 degrees, no significant kinetic changes are expected upon deuteration in agreement with our experimental and theoretical observation of a weak isotope-dependence on the excited-state lifetime. The main difference between the isotopomers used here is that the C_{11}-H and C_{12}-H wags are coupled for native 11,12-H_2 Rh and, similarly, the C_{11}-D and C_{12}-D wags are coupled for 11,12-D_2, resulting in the formation of anti-symmetric (the two hydrogen and deuterium atoms move in opposite directions) δ_{op} vibrations. Such vibration remains fully coherent during the excited state lifetime and maintains a specific phase relationship with the evolving carbon framework twisting α until the molecule decays via the CI. In this context, it is evident from both the experimental data and the simulation that the di-deuteration provides a slightly more suitable phase-matching of the δ_{op} with respect to the α coordinate, resulting in an increase in isomerization quantum yield. However, when a single position is deuterated, the coupling between the substituent at C_{11} and C_{12} is reduced with respect to the wild type chromophore resulting in slightly more isolated C-H and C-D out-of-plane wags defining the δ_{op} motion (this is particularly evident in the case of the deuterium substitution at C_{12} (see Figure 4.8b). Consequently, single deuterations alters the phase relationship between the C-H and C-D wagging motions and the α coordinate which, as the data and the simulations suggest, decrease the photoproduct (I.e. a completely randomized C_{11}-H and C_{12}-H wags would probably lead to a 0.5 quantum yield).

4.5 Two-mode harmonic model

Above we concluded that an increasing level of deuteration of the $C_{11}=C_{12}$ double bond can modulate the α/δ_{op} phase relationship. To investigate how such phasing relationship results in a non-monotonous quantum yield trend (increase for 11,12-D_2, decrease for 11-D and 12-D) for the Rh photoisomerization, we constructed a minimal two-mode harmonic mathematical model with frequency parameters (ω_α and $\omega_{\delta op}$) derived from the simulations. The model contains a α mode with frequency ω_α = 83 cm^{-1} and a δ_{op} mode with an isotope-dependent frequency $\omega_{\delta op}$ = 953 cm^{-1}, 855 cm^{-1} and 725 cm^{-1} for the wild-type 11,12-H_2, monodeuterated 11-D/12-D and di-deuterated 11,12-D_2 isotopomers, defined by equations 4.1 and 4.2.

$$\alpha=A_\alpha \cos[\omega_\alpha t]+B \qquad (4.1)$$

$$\delta_{op}=A_{\delta op} \cos[\omega_\delta t+C] \qquad (4.2)$$

The amplitude parameters A_α and $A_{\delta op}$ are also extracted from the 400 calculated trajectories and kept constant. The B and C coefficients represent initial conditions (t = 0) and are obtained from the simulated Boltzmann distribution of each isotopomer. Each trajectory computed using equations (4.1) and (4.2) represents the coherent dynamics of a subpopulation defined by the B and C values. The modeled time evolution of α, δ_{op} and the resulting τ value for specific B and C values of the 11,12-H_2 isotopomer are illustrated in Figure. 4.9a. The normalized fraction of decayed subpopulation (represented by a 2D-trajectory) at each time point is calculated to be proportional to the velocity of τ multiplied by the value of a reference Gaussian function (derived from the simulations) and a subpopulation decay factor, which represents the decay probability (Figure. 4.9a, gray shaded area). The subpopulation of 11,12-H_2

decays in three distinct waves (Figure. 4.9a, bottom), namely two reactive (orange) and one unreactive (blue) wave, showing the same compound character (i.e. with reactive and unreactive fractions) of the subpopulation decay found in the simulation (Figure. 4.6b). In fact, the short time separation between the first reactive and the unreactive wave and the larger time separation between the two successive reactive waves in Figure. 4.9a roughly matches the time separations between the corresponding reactive and unreactive maxima found in the simulation (Figure. 4.6b). On the basis of the present model, based upon subpopulations that can exit and then re-enter the decay region (see Figure 4.9b), the oscillations in the population decay for both the reactive and unreactive fractions are seen in a basic 2D model and results from the superposition of trajectory belonging to the subpopulation (i.e. with similar initial conditions). The modeling of trajectories characterized by different B and C values (i.e. of different subpopulations) and/or $\omega_{\delta op}$ value indicates that the above conclusions are general. The details of the two-mode harmonic mode construction are presented in section 4.8.

The origin of the decay waves can be understood by considering the corresponding temporal evolution of the α and δ_{op} coordinates (Figure. 4.9b). At ~70 fs delay (compare Figure. 4.9a and 4.9b); the trajectory enters the decay region. Initially the trajectory shows a positive velocity of δ_{op} and the corresponding decay leads to photoproduct formation (compare Figure. 4.9b to Fig. 4.6d). At the turning point, the trajectory inverts its direction, still remaining in the decay region, and thus leads to reactant formation upon decay. At ~85 fs, the trajectory exits the decay region halting a population decay. Just before 100 fs, however, the trajectory re-enters the decay region with a positive velocity of δ_{op} leading to a second wave of photoproduct formation, which is stopped after ~110 fs.

According to the above model the change in the overall quantum yield upon isotopic labeling depends on three factors characterizing each subpopulation: the initial conditions characterizing each subpopulation, the evolution of the phase relationship between δ_{op} and α and the magnitude of the dephasing of the C_{11}-H and C_{12}-H wags. We find that the deviation of the average δ_{op} of the simulated trajectories, $d(\delta_{op}{}^{AV})/dt$, of asymmetrically deuterated isotopomers is more sensitive to the value of the initial conditions than that of their symmetric counterparts. This is reflected by the deviation of the simulated population dynamics from a trajectory released from the vertical excited region with no velocities (see section 4.8). More specifically, the 11,12-H_2 and 11,12-D_2 populations follow rather closely such trajectory revealing that the corresponding motion is dominated by the structure of the S_1 potential energy surface rather than by the initial velocities. This condition would guarantee a high degree of vibrational coherence. In contrast, the 11-D and 12-D populations display much larger deviations suggesting a more de-phased motion and a lesser degree of vibrational coherence. Thus, despite being intrinsically dependent on a frequency change occurring upon isotopic substitution, the observed/simulated isotope effect should be described as a vibrational phase isotope effect, since it relies on a *dynamic phase relationship* achieved at the CI by the fundamental vibrational modes α and δ_{op} involved in the reaction coordinate.

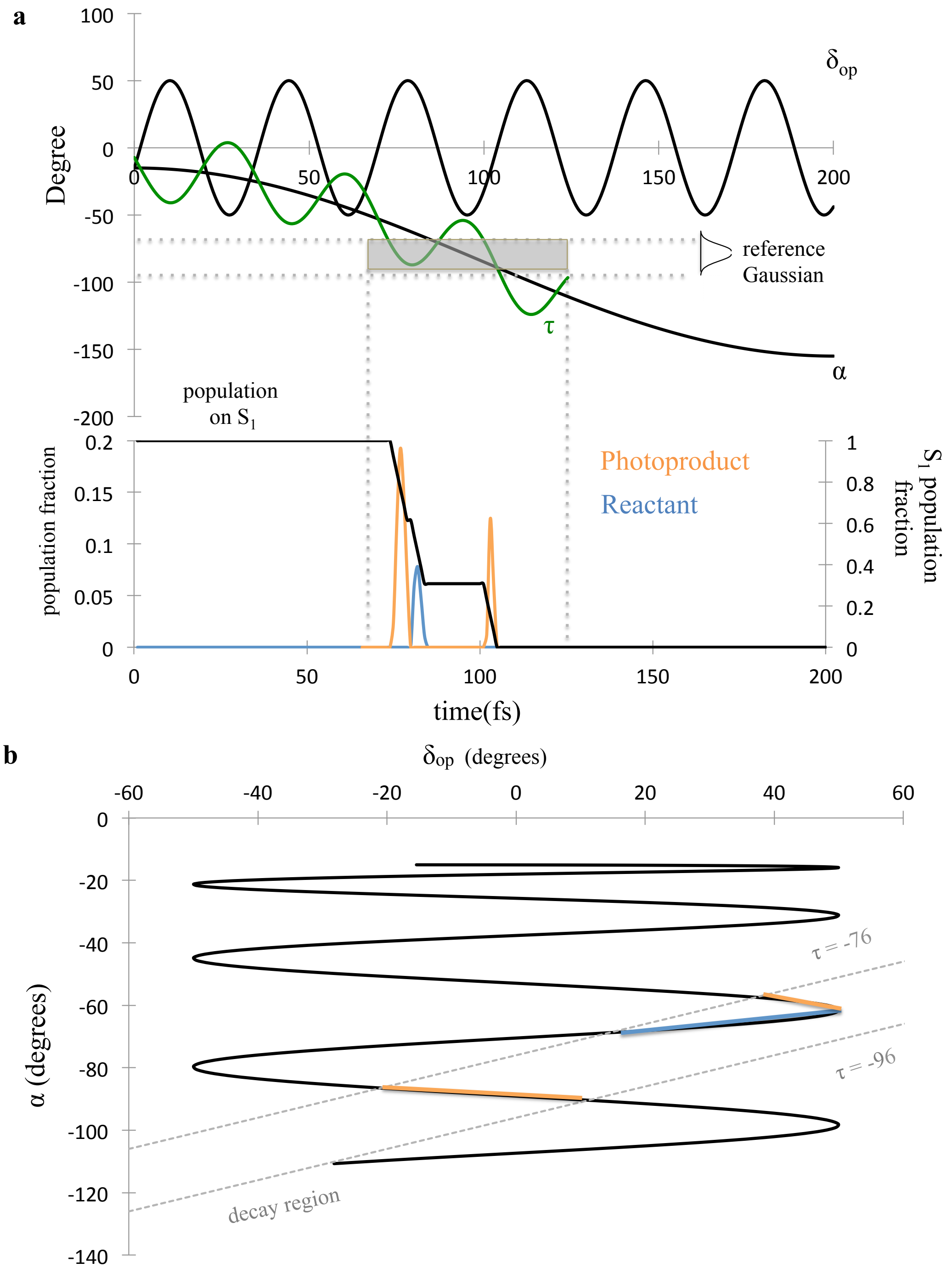

Figure 4.9 2-D modeling of simulated Rh population dynamics. **a.** Graphical representation of the α and δ_{op} periodic functions and Gaussian decay region defining the model. The alternating reactive and nonreactive population decay events produced by the model are projected below **b.** Origin of the reactive (orange) and nonreactive (blue) decay events in terms of trajectory segments characterized by an increase and decrease of δ_{op} while α is monotonically increasing. The shaded area between τ = -76 and τ = -96 degree defines the decay region (grey shaded) centered along the collection of CI points forming the intersection space (black dashed line).

4.6 Conclusion

Our theoretical results support the existence of a novel isotope effect that deuteration along the isomerizing double bond of the retinal chromophore in Rh causes a significant and unanticipated pattern of isomerization quantum yield changes while inducing only modest perturbations in the kinetics. The fact that this isotope effect is manifested in the quantum yield demonstrates the importance of multimode vibrational coherence in photochemical reactions, irrespective of the illumination conditions. In fact, we have shown that such isotopic effect is associated with a frequency change in the δ_{op} mode, whose vibrational phase at the decay point have an impact on the electron re-coupling, which allows for the C_{11}=C_{12} double bond reconstitution (this point will be discussed and illustrated in details in Chapter V). The unveiled vibrational-phase dependent photoisomerization reactivity should be functionally important for all vibrationally coherent processes and thus opens up new avenues for studying ultrafast energy flow in vibronic processes.

4.7 References

(1) Kukura, P. *Science (80-.).* **2005**, *310* (5750), 1006–1009.

(2) Schapiro, I.; Ryazantsev, M. N.; Frutos, L. M.; Ferré, N.; Lindh, R.; Olivucci, M. *J. Am. Chem. Soc.* **2011**, *133* (10), 3354–3364.

(3) Frutos, L. M.; Andruniow, T.; Santoro, F.; Ferre, N.; Olivucci, M. *Proc. Natl. Acad. Sci.* **2007**, *104* (19), 7764–7769.

(4) Strambi, A.; Coto, P. B.; Frutos, L. M.; Ferré, N.; Olivucci, M. *J. Am. Chem. Soc.* **2008**, *130* (11), 3382–3388.

(5) Schnedermann, C.; Liebel, M.; Kukura, P. *J. Am. Chem. Soc.* **2015**, *137* (8), 2886–2891.

(6) Wang, Q.; Schoenlein, R.; Peteanu, L.; Mathies, R.; Shank, C. *Science (80-.).* **1994**, *266* (5184), 422–424.

(7) Johnson, P. J. M.; Halpin, A.; Morizumi, T.; Prokhorenko, V. I.; Ernst, O. P.; Miller, R. J. D. *Nat. Chem.* **2015**, *7* (12), 980–986.

(8) Mathies, R. A. *Nat. Chem.* **2015**, *7* (12), 945–947.

(9) Garavelli, M.; Celani, P.; Bernardi, F.; Robb, M. A.; Olivucci, M. *J. Am. Chem. Soc.* **1997**, *119* (29), 6891–6901.

(10) Sinicropi, A.; Migani, A.; De Vico, L.; Olivucci, M. *Photochem. Photobiol. Sci.* **2003**, *2* (12), 1250.

(11) Garavelli, M.; Vreven, T.; Celani, P.; Bernardi, F.; Robb, M. A.; Olivucci, M. *J. Am. Chem. Soc.* **1998**, *120* (6), 1285–1288.

(12) Gozem, S.; Melaccio, F.; Lindh, R.; Krylov, A. I.; Granovsky, A. A.; Angeli, C.; Olivucci, M. *J. Chem. Theory Comput.* **2013**, *9* (10), 4495–4506.

(13) Weingart, O.; Garavelli, M. *J. Chem. Phys.* **2012**, *137* (22), 22A523.

(14) Weingart, O.; Altoè, P.; Stenta, M.; Bottoni, A.; Orlandi, G.; Garavelli, M. *Phys. Chem. Chem. Phys.* **2011**, *13* (9), 3645.

(15) Duan, H. G.; Miller, R. J. D.; Thorwart, M. *J. Phys. Chem. Lett.* **2016**, *7* (17), 3491–3496.

(16) Qi, D.-L.; Duan, H.-G.; Sun, Z.-R.; Miller, R. J. D.; Thorwart, M. *J. Chem. Phys.* **2017**, *147* (7), 074101.

(17) Mathies, R. A.; Lugtenburg, J. In *Handb. Biol. Phys.*; 2000; Vol. 3, pp 55–90.

(18) Laptenok, S. P.; Lukacs, A.; Gil, A.; Brust, R.; Sazanovich, I. V.; Greetham, G. M.; Tonge, P. J.; Meech, S. R. *Angew. Chemie Int. Ed.* **2015**, *54* (32), 9303–9307.

(19) Klinman, J. P.; Kohen, A. *Annu. Rev. Biochem.* **2013**, *82* (1), 471–496.

(20) Peters, K.; Applebury, M. L.; Rentzepis, P. M. *Proc. Natl. Acad. Sci.* **1977**, *74* (8), 3119–3123.

(21) Fransen, M. R.; Luyten, W. C. M. M.; Van Thuijl, J.; Lugtenburg, J. *Nature* **1976**, *260* (5553), 726–727.

(22) Schnedermann, C.; Yang, X.; Liebel, M.; Spillane, K. M.; Lugtenburg, J.; Fernández, I.; Valentini, A.; Schapiro, I.; Olivucci, M.; Kukura, P.; et al. *Nat. Chem.* **2018**, *10* (4), 449–455.

(23) Bassolino, G.; Sovdat, T.; Soares Duarte, A.; Lim, J. M.; Schnedermann, C.; Liebel, M.; Odell, B.; Claridge, T. D. W.; Fletcher, S. P.; Kukura, P. *J. Am. Chem. Soc.* **2015**, *137* (39), 12434–12437.

(24) Okada, T.; Sugihara, M.; Bondar, A.-N.; Elstner, M.; Entel, P.; Buss, V. *J. Mol. Biol.* **2004**, *342* (2), 571–583.

(25) Roos, B. O. In *Advances in Chemical Physics*; 2007; pp 399–445.

(26) Cornell, W. D.; Cieplak, P.; Bayly, C. I.; Gould, I. R.; Merz, K. M.; Ferguson, D. M.;

Spellmeyer, D. C.; Fox, T.; Caldwell, J. W.; Kollman, P. A. *J. Am. Chem. Soc.* **1995**, *117* (19), 5179–5197.

(27) Manathunga, M.; Yang, X.; Luk, H. L.; Gozem, S.; Frutos, L. M.; Valentini, A.; Ferrè, N.; Olivucci, M. *J. Chem. Theory Comput.* **2016**, *12* (2), 839–850.

(28) Ferre, N.; Cembran, A.; Garavelli, M.; Olivucci, M. *Theor. Chem. Acc.* **2004**, *112* (4), 335–341.

(29) Melaccio, F.; Olivucci, M.; Lindh, R.; Ferré, N. *Int. J. Quantum Chem.* **2011**, *111* (13), 3339–3346.

(30) Kandori, H.; Shichida, Y.; Yoshizawa, T. *Biochem.* **2001**, *66* (11), 1197–1209.

(31) Andersson, K.; Malmqvist, P.; Roos, B. O. *J. Chem. Phys.* **1992**, *96* (2), 1218–1226.

4.8 Two-mode harmonic model construction

A minimal (in terms of parameters) two-dimensional model of the population decay was constructed using the results of the analysis and fitting of the trajectory data (400 for each isotopomer). Trajectories with similar initial conditions were populated to a subset of the population (a subpopulation) featured by a single δ_{op} and α value (see Figure S4.1).

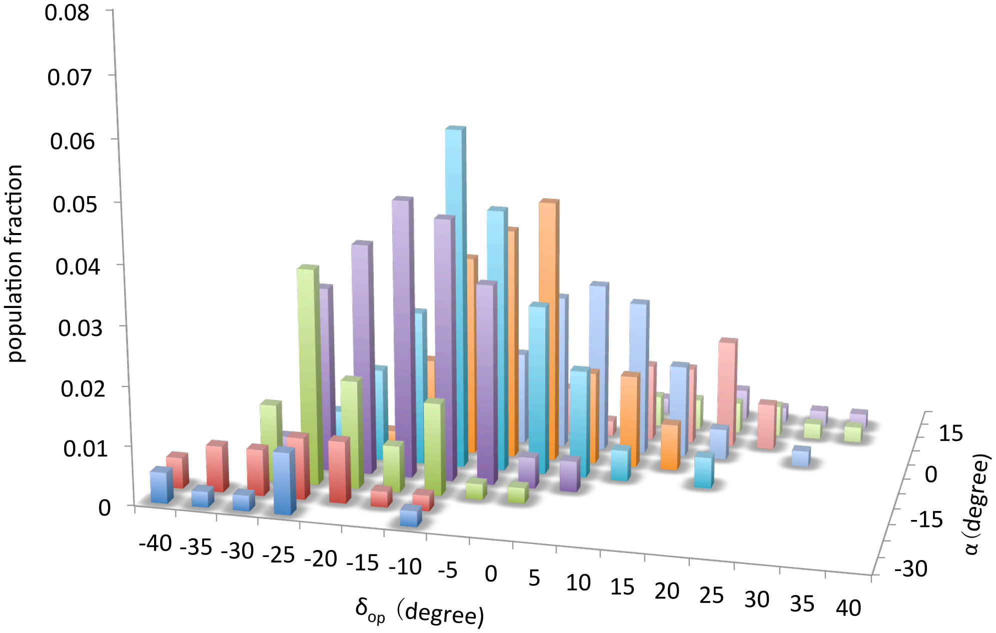

Figure S4.1 Subpopulations of initial conditions.

The model consists of two periodic functions (equations S4.1 and S4.2) assumed to represent the time evolutions of the double bond torsion α and hydrogen-out-of-plane δ_{op} of a subpopulation:

$$\alpha=A_{\alpha}\cos[\omega_{\alpha}t]+B \qquad \text{(S4.1)}$$

$$\delta_{op}=A_{\delta op}\cos[\omega_{\delta}t+C] \qquad \text{(S4.2)}$$

where t is the time changing from t=0 to t=200 fs. The amplitude parameters A_{α}, $A_{\delta op}$ were extracted from the trajectories and kept constant for all isotopomers, subpopulation and corresponding initial conditions. The torsion frequency ω_{α} (83 cm^{-1}) was also kept constant. In contrast, the hydrogen-out-of-plane frequency ω_{δ} was extracted from the trajectory of each isotopomer as explained in the previous section. These ω_δ vales are 953 cm^{-1}, 855 cm^{-1} and 725 cm^{-1} for the undeuterated 11,12-H_2, monodeuterated 11-D and 12-D and di-deuterated 11,12-D_2 isotopomers respectively. Similarly, the values of the parameters B and C representing the initial α and δ_{op} values at time 0 fs, were obtained from the calculated initial conditions defining each subpopulation.

At each time point along each α, δ_{op}-trajectory the fraction of decayed trajectories is computed as the $d\tau/dt$ velocity (degrees/fs) multiplied by the value of a reference Gaussian function (equation S4.3) representing the decay probability.

$$\text{Gaussian}(\tau,\mu,\sigma)=\frac{1}{\sigma\sqrt{2\pi}}e^{-\frac{(\tau-\mu)^2}{2\sigma^2}},\ \mu=-86,\sigma=\frac{10}{3} \qquad \text{(S4.3)}$$

Indeed the Gaussian spans the τ = -86 ± 10 degrees range indicated by the simulated trajectories as the “decay region” (i.e. close to geometries where the two π-orbitals are substantially orthogonal). A negative fraction corresponds to a reactive decay while a positive fraction corresponds to an unreactive decay.

The positive and negative decay fractions of each α, δ_{op}-trajectory, contribute to the total subpopulation quantum yield QY_{sub} (equation S4.4). Notice that the sum extends over all time point of the simulation.

$$QY_{sub}=\frac{\sum_{t=1}^{t=200}\text{photoproduct fraction}}{\sum_{t=1}^{t=200}\text{photoproduct fraction+reactant fraction}} \qquad \text{(S4.4)}$$

In order to compute the total quantum yield (QY_{total}) of each isotopomer (i.e. of its corresponding frequency) we consider all non-empty subpopulations (N_{ne}) (these are indicated as n=1 to N_{ne} in equation S4.5). Each subpopulation is characterized by specific initial conditions (the values of B and C in equations 1 and 2) and by the value of their weight (i.e. fraction) fr_n with respect to the total population.

$$\mathrm{QY_{total}} = \sum_{n=1}^{N_{ne}} \mathrm{fr_n QY_{sub,n}} \qquad \text{(S4.5)}$$

In our 2D-model the α, δ_{op}-trajectory defined above would represent a coherent subpopulation motion. We assumed that coherent motion is, primarily, the consequence of the force imposed by the excited state PES on each molecule belonging to an initial Boltzmann-like distribution. Therefore, for each isotopomer, the degree of coherence along the critical δ_{op} mode was computed by averaging the deviation of the δ_{op} velocities of the simulated trajectories from the δ_{op} velocity of the corresponding FC trajectory (equation S4.6)

$$\mathrm{Dv}_{\delta_{op}} = \frac{\sum_{i=1}^{400} d(\delta_{op}(i)-\delta_{op}{}^{FC})/dt}{400} = \frac{d(\delta_{op}{}^{AV})}{dt} - \frac{d(\delta_{op}{}^{FC})}{dt} \qquad \text{(S4.6)}$$

Where $\delta_{op}(i)$ is the velocity along the i_{th} trajectory and $\delta_{op}{}^{FC}$ is the velocity along the FC trajectory. The FC trajectory was thus taken as representative of the evolution of the center of a vibrational wavepacket moving coherently along the excited state potential energy valley connecting the FC structure with the decay region. $\mathrm{Dv}_{\delta op}=0$ represents a situation where the population run parallel to that of the FC trajectory and its coherent with it.

It is apparent from the diagrams in Figure. S4.2 that while the 11,12-H_2 and di-deuterated 11,12-D_2 isotopomers do not display large $\mathrm{Dv}_{\delta op}$ values, the monodeuterated isotopomers 11-D and 12-D deviates significantly indicating a larger sensitivity to the value of the initial conditions. We heuristically assumed that the magnitude of the maximum $\mathrm{Dv}_{\delta op}$ variation ($\mathrm{MDv}_{\delta op}$) is proportional to the magnitude of the dephasing/dechoerence of the excited state population dynamics.

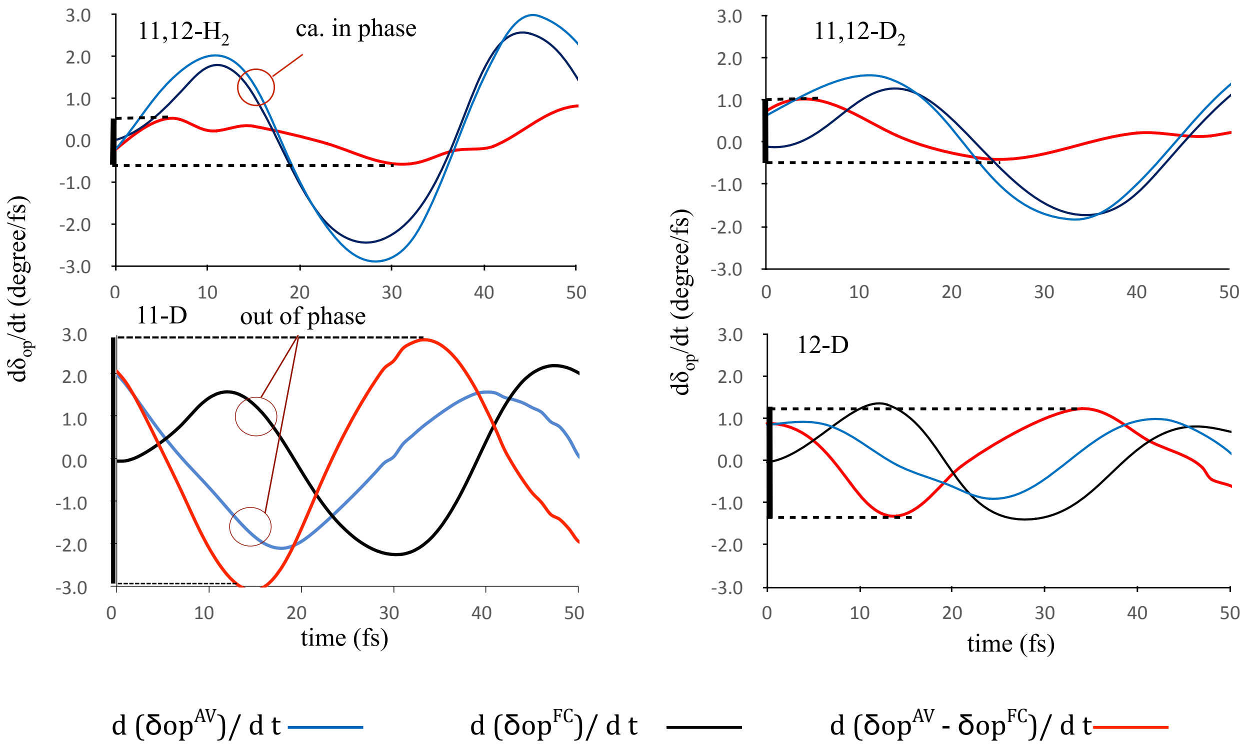

Figure S4.2 Time progression of Dv$_{\delta op}$ for each isotopomer. The average dδ$_{op}$(i)/dt or, equivalently, d(δ$_{op}^{AV}$)/dt value (blue) for each isotopomers is compared with the corresponding dδ$_{op}^{FC}$/dt value (black). The differences between these two velocities, Dv$_{\delta op}$, are also given (red). The bold segment on the ordinate axis represents the maximum Dv$_{\delta op}$ variation MDv$_{\delta op}$.

In order to incorporate the effect of the de-phasing in our interpretative 2D-model, we divide the excited state population in “in-phase” and “out-of-phase” components according to a parameter γ_δ. The total quantum yield, which becomes a function of both ω_δ and γ_δ, was then expressed using equation S4.7.

$$QY_{total}=(1-\gamma_\delta)\sum_{n=1}^{N_{ne}} fr_n QY_{sub,n} \qquad (S4.7)$$

The $MDv_{\delta op}$ values of 11,12-H_2 and 11,12-D_2 are ca. 1.0 and 1.5 degree/fs (see black vertical bars on the velocity axis of Figure S4.2) respectively. The $MDv_{\delta op}$ values of 11-D and 12-D are larger corresponding to ca. 3.5 and 2.5 degree/fs respectively. These values are used to compute the values of the corresponding γ_δ parameters in the following way. The average effect of the de-phasing on the quantum yield was estimated by looking at the difference between the total quantum yield of the original 2D-model, which does not consider the de-phasing (i.e. the one of Table S4.1 here indicated as $QY_{2D\text{-}model}$) and of the simulated dynamics (incorporating the de-phasing). From Table S4.1 we obtain an average total quantum yield difference of ca. 0.06. This value was then used, together with the $QY_{2D\text{-}model}$ and $MDv_{\delta op}$ values, to compute the γ_δ using the relationship:

$$\frac{QY_{2D\text{-}model}-0.06}{QY_{2D\text{-}model}}=\left(1-\frac{\gamma_\delta}{MDv_{\delta op}}\right) \qquad (S4.8)$$

The γ_δ values were 0.08, 0.11, 0.32 and 0.23 for 11,12-D_2, 11,12-D_2, 11-D and 12-D respectively. Using these quantities we re-computed the QY_{total} values for the 2D-model now incorporating a heuristic de-phasing correction. The final QY_{total} values are those reported in Table S4.1 below.

Table S4.1 Comparison of simulated quantum yields for reduced PSB5-Rh model with those computed according to two different 2D-models

	11,12-H$_2$	**11,12-D$_2$**	**11-D**	**12-D**
QY simulated	0.69	0.70	0.61	0.58
Decay time[a]	100	113	100	93
QY 2D-model	0.71	0.79	0.65	0.65
Decay time[b]	105	96	113	101
QY 2D-model with de-phasing corr.	0.65	0.70	0.44	0.50

[a] Average hop time.

[b] This time is evaluated as the time when half of the population has decayed.

4.9 Chapter copyrights

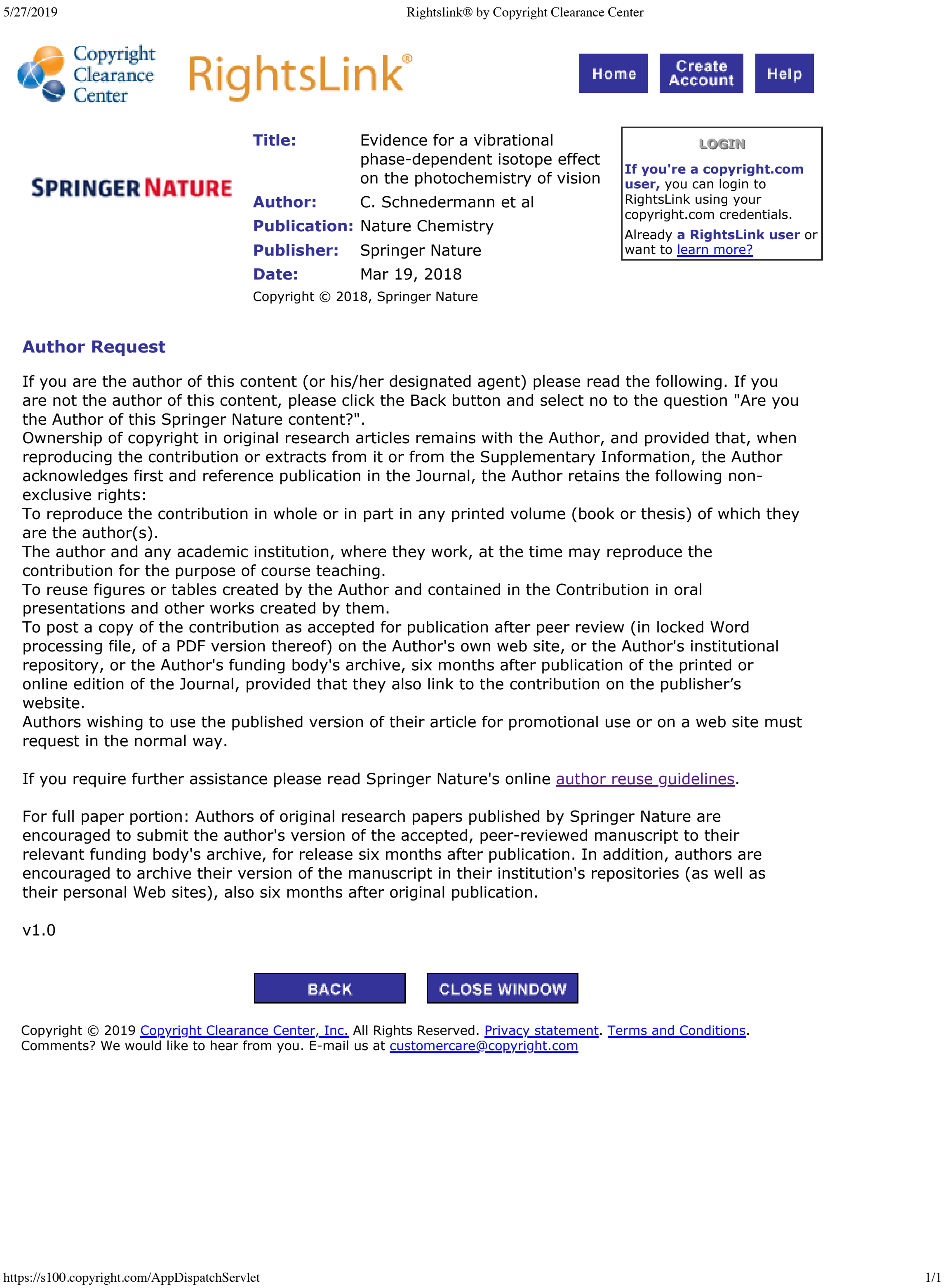

5/27/2019 Rightslink® by Copyright Clearance Center

Title: Evidence for a vibrational phase-dependent isotope effect on the photochemistry of vision
Author: C. Schnedermann et al
Publication: Nature Chemistry
Publisher: Springer Nature
Date: Mar 19, 2018
Copyright © 2018, Springer Nature

If you're a copyright.com user, you can login to RightsLink using your copyright.com credentials.
Already **a RightsLink user** or want to learn more?

Author Request

If you are the author of this content (or his/her designated agent) please read the following. If you are not the author of this content, please click the Back button and select no to the question "Are you the Author of this Springer Nature content?".
Ownership of copyright in original research articles remains with the Author, and provided that, when reproducing the contribution or extracts from it or from the Supplementary Information, the Author acknowledges first and reference publication in the Journal, the Author retains the following non-exclusive rights:
To reproduce the contribution in whole or in part in any printed volume (book or thesis) of which they are the author(s).
The author and any academic institution, where they work, at the time may reproduce the contribution for the purpose of course teaching.
To reuse figures or tables created by the Author and contained in the Contribution in oral presentations and other works created by them.
To post a copy of the contribution as accepted for publication after peer review (in locked Word processing file, of a PDF version thereof) on the Author's own web site, or the Author's institutional repository, or the Author's funding body's archive, six months after publication of the printed or online edition of the Journal, provided that they also link to the contribution on the publisher's website.
Authors wishing to use the published version of their article for promotional use or on a web site must request in the normal way.

If you require further assistance please read Springer Nature's online author reuse guidelines.

For full paper portion: Authors of original research papers published by Springer Nature are encouraged to submit the author's version of the accepted, peer-reviewed manuscript to their relevant funding body's archive, for release six months after publication. In addition, authors are encouraged to archive their version of the manuscript in their institution's repositories (as well as their personal Web sites), also six months after original publication.

v1.0

https://s100.copyright.com/AppDispatchServlet 1/1

This Chapter, in part, reused the content of the jounarl article:

"Schnedermann, C.; Yang, X.; Liebel, M.; Spillane, K. M.; Lugtenburg, J.; Fernández, I.; Valentini, A.; Schapiro, I.; Olivucci, M.; Kukura, P.; and Mathies, R. A. *Nat Chem*. **2018**, *10*, 449-455."

with permission from:

Dr. Christoph Schnedermann, Dr. Matz Liebel, Dr. Katelyn Spillane, Dr. Johan Lugtenburg, Dr. Isabelle.Fernández, Dr. Alessio Valentini, Dr. Igor Schapiro, Dr. Massimo Olivucci, Dr. Philipp Kukura, Dr. Richard A. Mathies

CHAPTER V. IMPACT OF VIBRATIONAL COHERENCE ON THE PHOTOCHEMICAL EFFICIENCY OF BOVINE RHODOPSIN

5.1 Abstract

The vibrationally coherent photoisomerization of rhodopsin is one of the most efficient biological processes in nature. However, how such extreme efficiency is achieved and whether it is related with the vibrational coherent atomic motions along the isomerization coordinate remains unknown. In this chapter, we employ population dynamics simulation of 200 semi-classical trajectories of Rh featuring a full retinal chromophore to investigate the impact of vibrational coherences on the photoisomerization quantum yield. The results show that the degree of coherence of the isomerization mode, i.e. the $C_{11}=C_{12}$ twisting mode, decreases from 20 to 30 fs after light absorption. We also show that the electronic coupling between the reactive electronic state and a higher unreactive state controls such decoherence process. The loss of coherence in the isomerization mode leads to splitting of the initially coherent excited state population into subpopulations of various excited state lifetime. Such "splitting-then-decaying" mechanism enhances photoproduct formation by exploiting the phase relationships between the isomerization mode and the HOOP mode of the H atoms located on the isomerizing double bond at the decay point for each subpopulation as described in the previous chapter.

5.2 Introduction

As mentioned in Chapter I, the photoisomerization of Rh is a vibrationally coherent biological process driven by three types of vibrational motions, namely α, the torsional twisting mode and δ_{op}, the HOOP mode of the $HC_{11}=C_{12}H$ fragment, on the isomerizing $C_{11}=C_{12}$ double bond as well as the BLA mode[1,2] (Figure 1.2a). Despite complementary experimental and theoretical efforts, no direct information on the impact of vibrational coherences on the Rh photoisomerization quantum yield has been reported so far. In Chapter IV, we unveil a relationship between the isomerization reactivity and the α/δ_{op} phase at the point of S_1/S_0 CI. More specifically, the isomerization is successful (i.e. produces the photoproduct rPSBAT) when α moves in the negative (couterclockwise) direction and δ_{op} move out-of-phase with α at the point of decay from S_1 to S_0. In terms of hydrogen motion this condition means that the $HC_{11}=C_{12}H$ hydrogens move in the same counterclockwise direction of the C_{10} and C_{13} carbons of the $C_{10}C_{11}=C_{12}C_{13}$ framework. On the other hand, an in-phase α and δ_{op} motion promote unsuccessful isomerization (i.e. leads to rPSB11 back formation) and this means that the $HC_{11}=C_{12}H$ hydrogens move in the opposite clockwise direction with respect to the C_{10} and C_{13} carbons. In fact, the α value changes most frequently monotonically in a counterclockwise direction during the dynamics from around 0 to -90 degrees (i.e., it displays a negative α velocity, $d\alpha/dt < 0$ at CI). Thus, the α/δ_{op} out-of-phase motion is equivalent to an increasing in δ_{op} value at the decay point (i.e., a positive δ_{op} velocity, $d\delta_{op}/dt > 0$, at CI). Such relationship is illustrated in Figure 5.1a.

In Chapter IV the α/δ_{op} phase relationship is obtained from the population dynamics simulation with PSB5-Rh model and provides a theoretical basis for explaining a recent observed isotopic effect on the Rh quantum yield[3]. The experiment shows that the Rh quantum yield is sensitive to deuterium substitution in $HC_{11}=C_{12}H$ moiety that is found to decrease in $DC_{11}=C_{12}H$ and $HC_{11}=C_{12}D$ but to increase in $DC_{11}=C_{12}D$. Indeed, as explained in Chapter IV, such trend is easily interpreted in terms of a change of the δ_{op} frequency introduced by the deuterium substitution and, in turn, a change of the δ_{op} phase at the decay point. However, the validation of the α/δ_{op} phase relationship on a Rh QM/MM model comprising the full retinal still remains unknown. If such validation is achieved, one can conclude that the quantum yield indeed reflects the fraction of population whose rPSB11 chromophores decaying with a positive δ_{op} velocity. Spectroscopic and theoretical evidences[4,5] have identified the δ_{op} mode to be a coherent motion with period of around 40 fs. In this case, a largest possible population decaying with positive δ_{op} velocity is required to maximize the quantum yield and, therefore, the photoreceptor light sensitivity. One can envision two possible decaying strategies that Rh would adopt to satisfy such requirement. The first strategy is a "narrow-decaying" strategy where the entire S_1 population decays coherently in a very short time window when the δ_{op} value is increasing. The second strategy is a "splitting-then-decaying" strategy based on the possibility that the initially coherent S_1 population decoheres in a discrete fashion at a certain time delay, ultimately splitting into several sub-population which will reach the decay region at different times but always when the desired δ_{op} phase is such to correspond to a positive velocity. A schematic interpretation both of mechanisms is in Figure 5.1b, where both α and δ_{op} modes are simplified as harmonic functions.

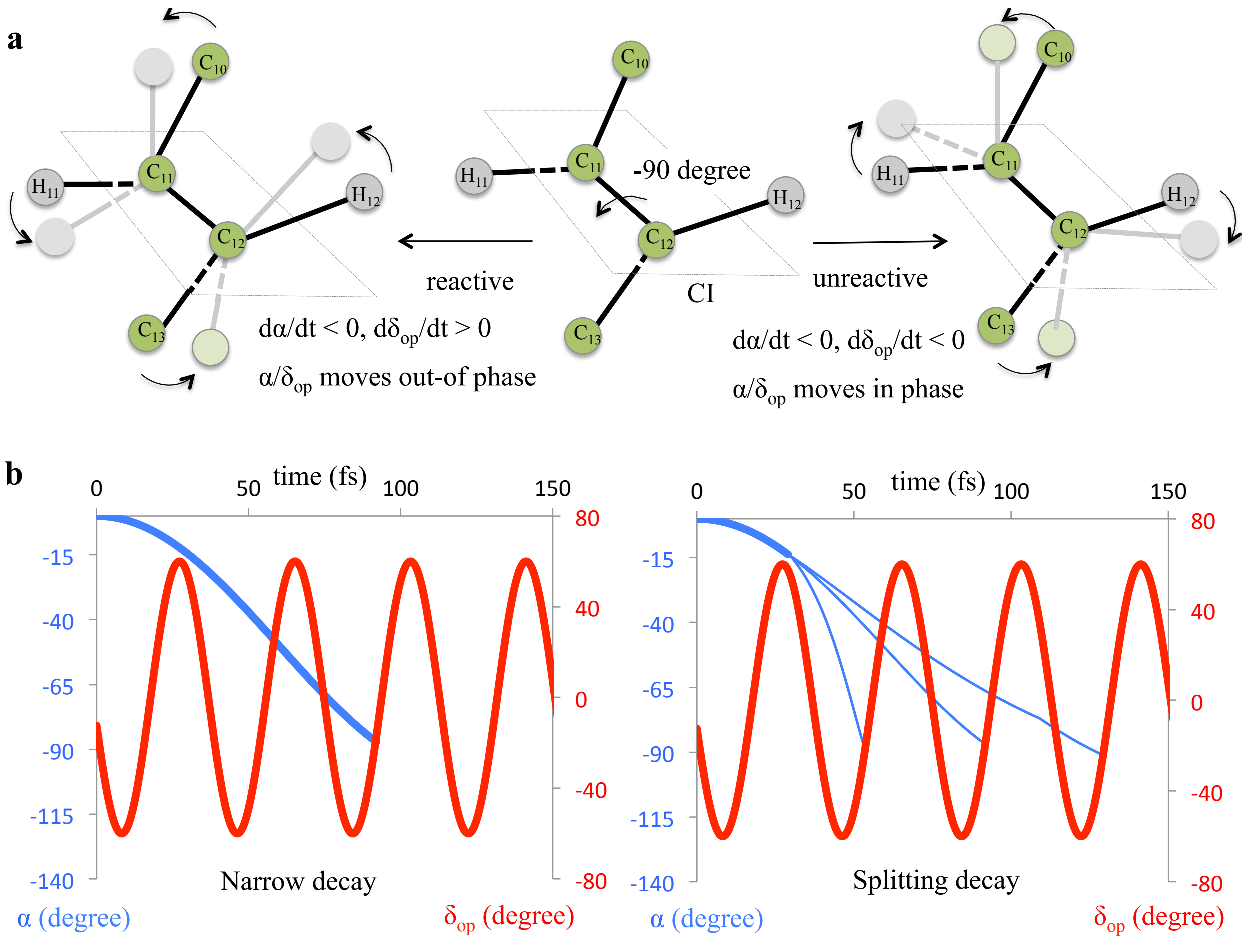

Figure 5.1 Schematic representation of α/δ_{op} phasing determined reactivity and possible decaying mechanism. **a**. Photoproduct formation (reactive decay) requires an out-of phase α/δ_{op} at decay point, while back to rPSB11 reactant (unreactive decay) occurs if the modes are in phase at decay. **b**. Narrow-decaying mechanism (left) and splitting-then-decaying mechanism (right), the α and δ_{op} modes are in blue and red, respectively.

Despite both strategies may lead to a maximization of the quantum yield, the former one is not consistent with both experimental and theoretical evidences. Recent studies reported early photoproduct formation occurring within 50 fs after light absorption but then a decay process lasting for more than 150 fs[2,6]. This result is consistent with the computational results reported in Chapter IV, where we observed decay events occurring from early 50 fs to late 170 fs. Furthermore, in Section 4.4.2 we discuss the bifurcating behavior of the α motion that partial excited state population decay with a monotonically decreasing α motion and thus, decay to S_0 at relatively short timescale while other fractions of the population invert the twisting direction of the α motion from counterclockwise to clockwise and then back to counterclockwise, resulting in delayed decay events.

Consistently with the simulation with PSB5-Rh model, our hypothesis is that the Rh photoisomerization follows a "splitting-then-decaying" mechanism to maximize the quantum yield. More specifically, the δ_{op} motion keeps its coherency all along the decay process and its phase at the decay point determine the reactivity while the α motion loses coherence at an early stage and splits in subpopulations decaying at different times. Currently, it is unclear if and at what extent Rh follows the above idea. Also, factors that contribute to the α bifurcation remains unknown. Accordingly, in the present chapter we employ 200 non-adiabatic trajectories with a QM/MM Rh model featuring a full retinal chromophore to simulate the population dynamics of Rh at room temperature.

5.3 Methods

5.3.1 Rh QM/MM model construction and validation

We built the Rh QM/MM model following the same protocol as reported in chapter IV. Briefly, the model construction started from its 2.2 Å resolution crystallographic structure (PDB code: 1U19)[7]. The QM and MM subsystems as well as the flexible cavity were defined in the same way as in Chapter IV (Figure 4.3 and section 4.3) and an ESPF[8] approach is adapted on the QM/MM frontier. The absorption maximum λ^a_{max} of 487 nm, which was evaluated by computing the vertical excitation energy at CASPT2 level of theory, is consistent with observed value of 498 nm[9]. A FC trajectory (i.e., a single trajectory released from S_1 vertical excitation region with zero initial velocity) was performed for 200 fs. The excited state molecule reaches S_1/S_0 CI at 80 fs with a counterclockwise twisting of the isomerizing $C_{11}=C_{12}$ double bond from around -5 to -90 degrees, which is accompanied with the clockwise twisting of $C_9=C_{10}$ double bond (Figure 5.2a), forming a bicycle-pedal motion that has been previously reproted[10–13]. Moreover, the time evolution of the δ_{op} and BLA modes (Figure 5.2b) provide simulated vibrational frequencies consistent with the observed data[2] listed in Table 5.1.

Table 5.1 Comparison of λ^a_{max} and vibrational frequencies between experiment and simulation

	λ^a_{max} (nm)	**Frequency of δ_{op} (cm^{-1})**	**Frequency of BLA (cm^{-1})**
Observed	498	746	1679
Simulated	487	878	1516

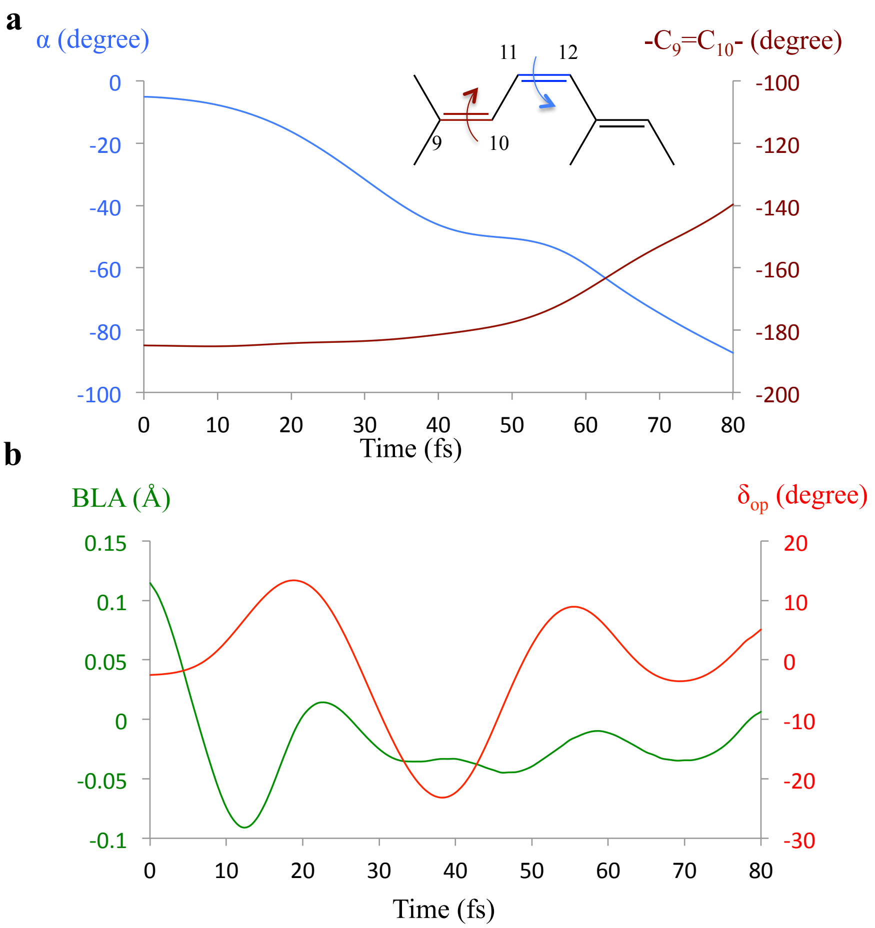

Figure 5.2 Excited state vibrational motions along the Rh FC trajectory. **a.** The bicycle-pedal motion is formed by a counterclockwise twisting of α motion (in blue) and a revising twisting of the C_9=C_{10} double bond (in brown). **b.** The excited state BLA (in green) and δ_{op} (in red) motions.

5.3.2 Initial conditions generation and validation

Due to the high computational cost, we generated a Boltzmann-like distribution of 200, instead of 400, initial conditions for the full retinal Rh model following the protocol reported in Chapter III and Chapter IV. The quality of the computed Boltzmann-like distribution is evaluated by plotting the absorption wavelength, distribution of α, δ_{op} and BLA coordinates. Expected Gaussian-like shape is achieved for all coordinates and the λ^{a}_{max} of the whole population is 500 nm consistent with observed data[9] (Figure 5.3). We then launch the trajectories starting from the initial conditions generated with Tully surface-hop[14] method for 200 fs.

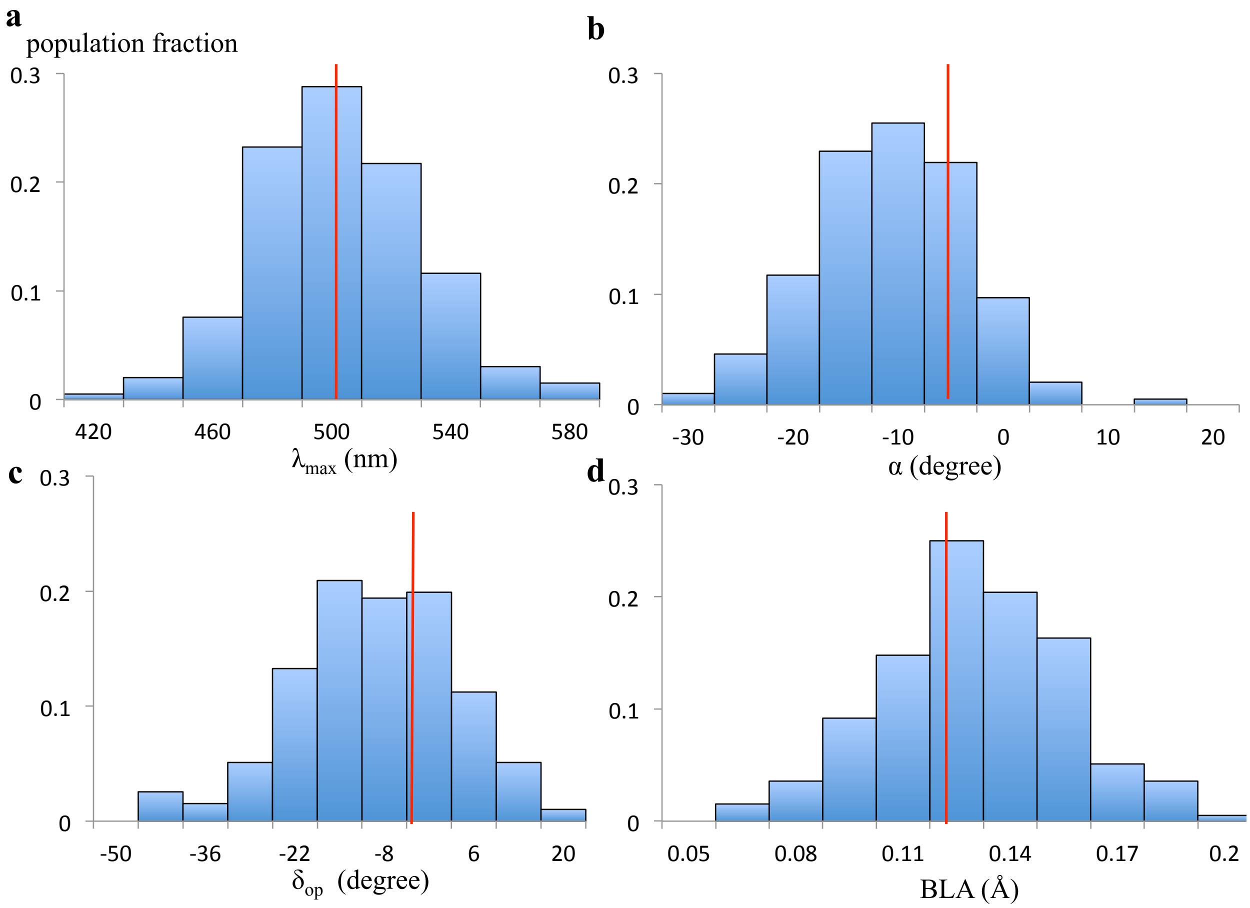

Figure 5.3 Initial condition validations. **a.** Absorption wavelength. **b**. Distribution of α coordinate. **c**. Distribution of δ_{op} coordinate. **d**. Distribution of BLA coordinate. The corresponding value of the S_0 equilibrium structure is given in vertical red line.

5.4 Results and discussion

5.4.1 Analysis of population dynamics

The simulated results from 200 excited state semi-classical trajectories, are in agreement with the experimental observed data in terms of excited state lifetime and quantum yield (see Table 5.2). The simulated excited state lifetime is fitted by equation 3.2 in Chapter III (fitting is shown in Figure S5.1) and the quantum yield is calculated as the ratio of number of trajectories forming photoproduct over the total number of trajectories decaying to S_0. The isotopic effect on quantum yield is also reproduced with a small set of 50 trajectories of 11-D and 11,12-D_2 Rh models where the quantum yield decreases with mono-deuteration but increases with duo-deuteration which is consistent with the results seen in Chapter IV but obtained with a more approximate method. The agreement between observed and simulated results indicates that a sample of 200 trajectories is at least qualitatively acceptable to probe the properties of Rh photoisomerization.

Table 5.2 Comparison of observed and simulated S_1 lifetime and quantum yields of wild type and deuterated Rh models

	S_1 lifetime (fs)	**QY**		
		11,12-H_2	**11D**	**11,12-D_2**
Observed	148 ± 10[3]	0.67[15]/0.65[3]	0.45[3]	0.69[3]
Simulated	92 ±32[a] 98[b]	0.68[c] (0.72)[d]	0.62[d]	0.75[d]

a. Average hop time of 200 trajectories. b. Fitted lifetime of 200 trajectories. c. Based on a sample of 200 trajectories. d. Based on a sample of 50 trajectories.

The time evolution of the decay events (the time it takes for the S_1 trajectories to decay to S_0 entirely) is shown in Figure 5.4a, where the orange and blue curves indicate decay events associated with formation of the photoproduct rPSBAT (reactive decay) and reconstitution of the reactant rPSB11 (unreactive decay), respectively. Figure 5.4a displays two remarkable features of the population decay. One is that the decay events groups into four subpopulations (I to IV in Figure 5.1a), starting from 35 fs and spanning around 150 fs. More specifically, subpopulation I decays with the fastest rate between 40 to 80 fs following by a relatively small subpopulation II decaying between 80 to 100 fs. A broad subpopulation III decays between 100 and 150 fs and a small "tail" subpopulation IV decays beyond 150 fs. Obviously, such decay waves originate in the bifurcating α motion (namely, featuring decoherence) shown in Figure 5.4c. Consistently with the excited state α motion of all 200 trajectories, which is plotted in such a way to display the orange/blue dots marking the reactivity of the corresponding decay events, the coherence of the α mode is only kept for 25-30 fs. In fact, after such short time, a group of trajectories keeps moving along a counterclockwise α motion, forming the rapidly decaying subpopulation I and II. Slower trajectories instead form subpopulation III and IV whose origin is apparently due to an inversion of the direction of α motion from a counterclockwise to a clockwise direction and then re-inverts to the counterclockwise direction, resulting in a delayed decay ranging from 100 to 170 fs. Notice that the loss of coherence is fast and significant only along α mode but slower and weak along the δ_{op} mode (see Figure 5.4d).

The second remarkable feature is related to the oscillatory nature of the successful and unsuccessful decay. Consistently with the simulation based on PSB5-Rh model, when separating the total population into successful and unsuccessful subsets, it is possible to demonstrate the existence of a relationship between the sign of the δ_{op} velocity and the probability of successful photoisomerization (Figure 5.4b). This is also evident from Figure 5.4d where it is clear that the orange points are dominating the growing sides of the coherent harmonic δ_{op} motion. More specifically, it is found that successful trajectories are statistically dominated by trajectories that, at the decay point, satisfy the out-of-phase relationship of δ_{op} with respect to α introduced above thus confirming the rule proposed for the PSB5-Rh models.

The above results support the hypothesis of the “splitting-then-decaying” mechanism. Again, according to such mechanism the initially coherent S_1 population splits into subpopulations of different decay timescale and then the total quantum yield is contributed from the quantum yield of each subpopulation, which is determined by the α/δ_{op} phasing at decay point. The decay time range, quantum yield and corresponding population fraction of each subpopulation are listed in Table 5.3. Notice that all three major subpopulations (I-III) display quantum yields over 0.6 and subpopulation II nearly excludes unreactive trajectories. This results suggest that the initial compact population splits in such a way that an increasing δ_{op} mode (i.e., favoring photoproduct formation) is available at the time of decay thus satisfying the phase relationship mentioned above and documented in Chapter IV.

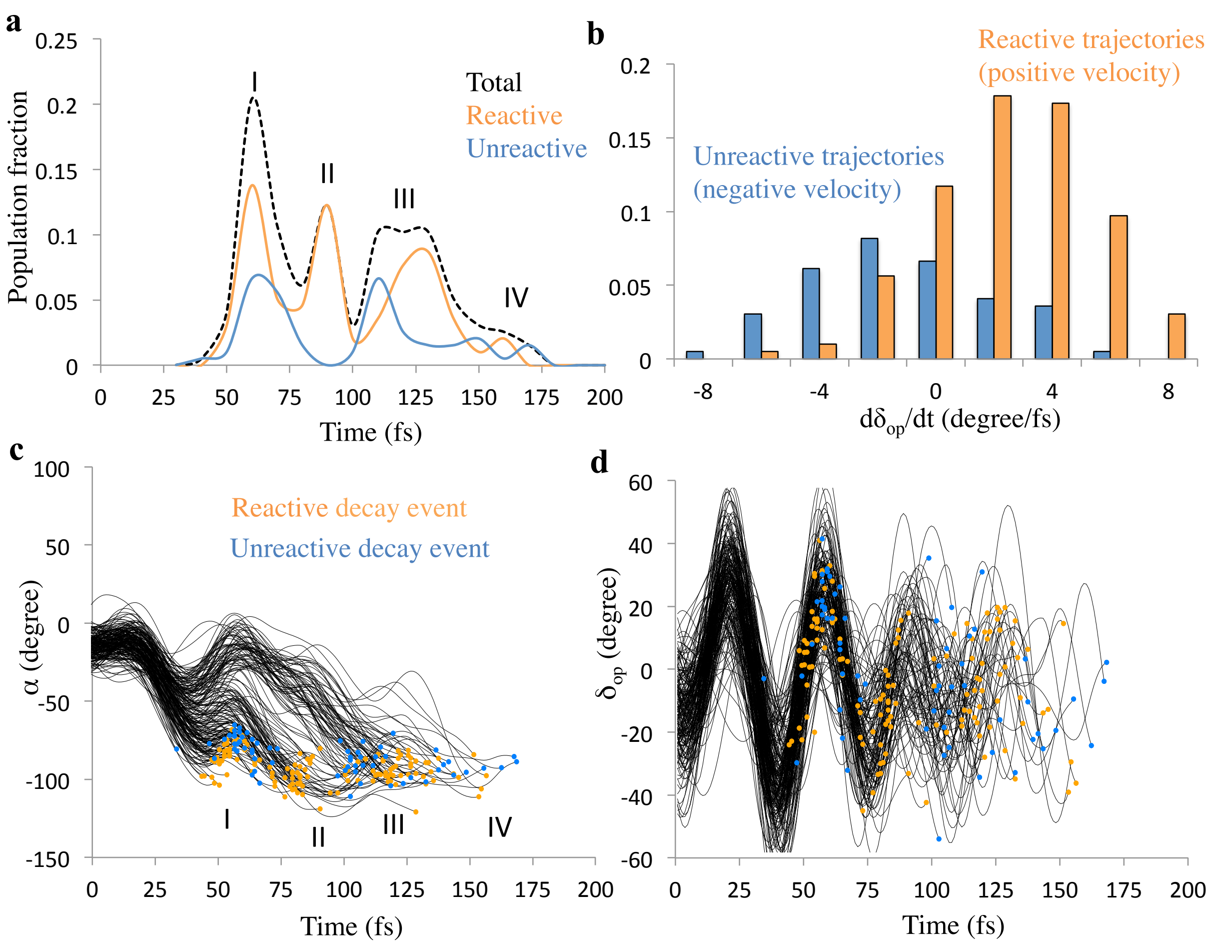

Figure 5.4 Simulated population dynamics of Rh. **a.** The excited-state population decay follows an oscillatory character for both the reactive (orange) and unreactive (blue) trajectories and splits into four subpopulations. **b.** Distribution of the δ_{op} velocities at the decay for the reactive and unreactive trajectories. Positive and negative δ_{op} velocities correlate with reactive (orange) and unreactive (blue) events (also valid for **c** and **d**), respectively. **c.** The time evolution of α motion for 200 trajectories. The bifurcating α motion leads to population splitting. **d.** The time evolution of δ_{op} motion for 200 trajectories.

Table 5.3 Comparison of decay range, quantum yields and weight of all subpopulations

Subpopulation	Decay range (fs)	Quantum yield	Population fraction (%)
I	40 ~ 80	0.61	41
II	80 ~ 100	0.97	16
III	100 ~ 150	0.63	39
IV	150 ~ 170	0.44	4

5.4.2 The α bifurcation is induced by S_1/S_2 state mixing

Here remains the question relative to the cause of the α bifurcation. We extract two subpopulations of similar size out of 200 trajectories. One corresponding to a fast-decaying subpopulation of 49 trajectories that reaches CI within 60 fs without apparent bifurcation and the other to a population of 48 trajectories that decays to S_0 after 120 fs but with strong α bifurcation (red and green curves in Figure 5.5a, respectively). We observed no significant difference in the initial value and velocity of α, δ_{op} and BLA modes of both subpopulations, indicating a weak dependence of the bifurcation event on geometrical initial conditions (see Figure 5.5b, c and d). Furthermore, at the CIs α values of both subpopulations are centered at -90 degree and the α/δ_{op} phase relationship leading to successful events is found to be valid. Those two subpopulations also display similar quantum yields (0.67 for fast-decaying subpopulation and 0.69 for slow-decaying subpopulation). Thus, when examining the initial conditions in terms of geometry and velocities no clear factor has been found that could explain the distinct behavior of α motion in both populations.

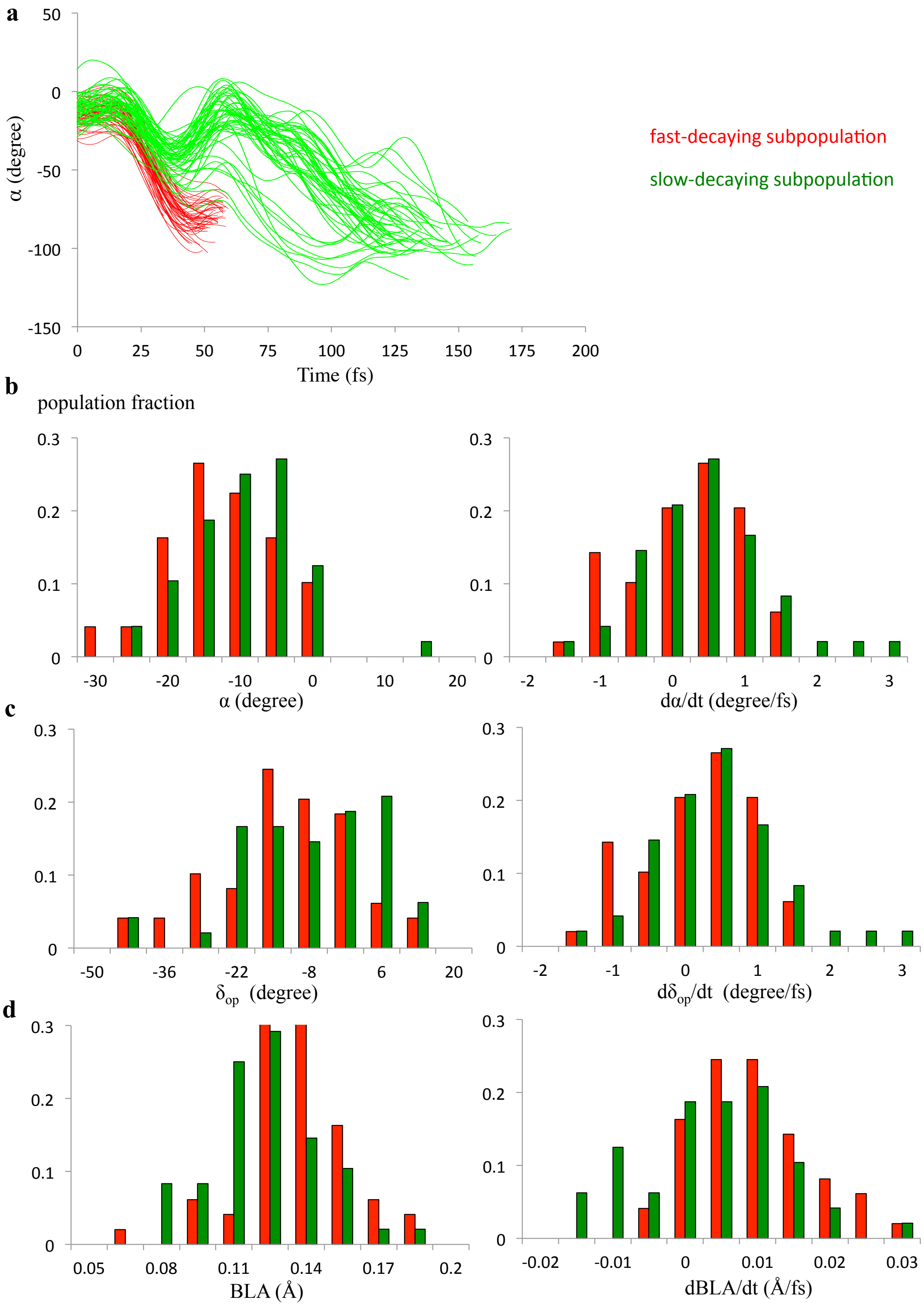

Figure 5.5 Splitting of excited state population is independent on initial conditions. **a.** The time evolution of α motion for extracted fast-decaying (in red) and slow-decaying (in green) subpopulations. **b, c and d.** Distributions of initial value and velocity of α, δ_{op} and BLA for fast-decaying (in red) and slow-decaying (in green) subpopulations are indistinguishable.

The similar initial conditions between fast- and slow-decaying subpopulations imply that those two subpopulations enter different regions of the S_1 PES with distinct shapes after the light absorption. The fast-decaying subpopulation must undergo a barrierless path processes leading directly to the CI while the slow-decaying subpopulation must experience a restrain force along the α mode that temporarily restrain the counterclockwise twisting. Previous studies[16–18] has shown that such force can be related with the electronic coupling between the reactive S_1 and its higher neighbor unreactive S_2 electronic state. As illustrated in Figure 5.6a, the S_1 state of Rh is dominated by a charge transfer (ionic) configuration while its S_2 state has a diradical electronic structure. The S_1 is reactive as the ionic electronic configuration promotes the heterolytic breaking of the original C_{11}=C_{12} double bond which acquires single bond character thus enabling isomerization. While the S_2 is unreactive since the partially bounded C_{11}=C_{12} bond restrain torsional deformation along α. Indeed, previous study[19] has employed FC trajectories to demonstrate that, unlike microbial rhodopsins which easily enters regions of S_1/S_2 degeneracy, the S_1 and S_2 of Rh remain well separated during the isomerization. Another study has reported a correlation between the S_1 lifetime and S_1/S_2 electronic state mixing[16]. The author reported that rPSB11 in methanol solution exhibits a strong S_1/S_2 mixing and a longer S_1 lifetime with respect to the protein environment. Therefore, one can conclude that a mixing of charge-transfer and diratical electronic character along the S_1 PES would slow down the isomerization as the reactive charge-transfer character would be replaced by a more bounded character via S_1/S_2 state mixing.

Our hypothesis is that after the vertical excitation to S_1, the fast-decaying subpopulation enters into a region where S_1 and S_2 are well separated (Figure 5.6b, left) and the steep S_1 PES accelerates the excited state molecules towards to CI that is rapidly reached. In contrast, the slow-decaying subpopulation enters into a region encountering S_1/S_2 state mixing (Figure 5.6b, right) where the S_1 wave function acquires significant or even dominating by bounded diradical character instead of reactive charge-transfer character and thus the α mode temporarily reverts the twisting direction.

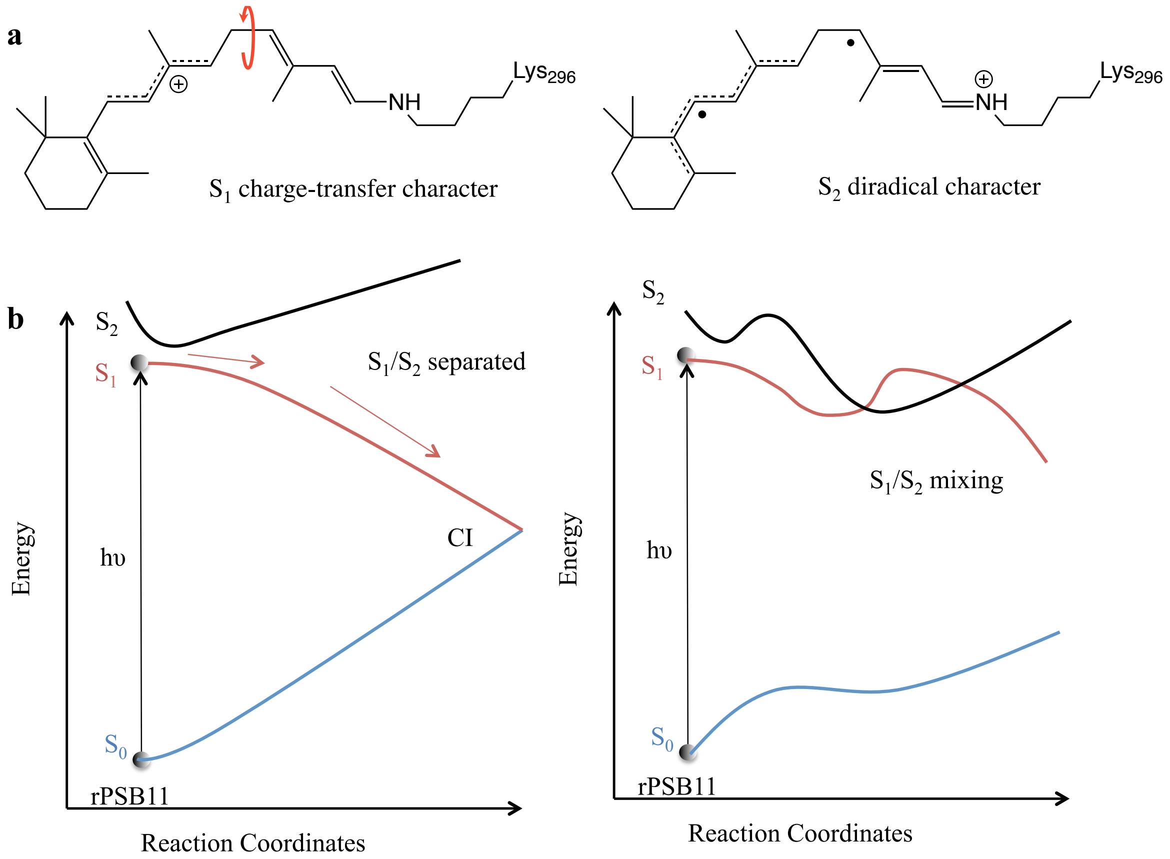

Figure 5.6 S$_1$/S$_2$ state mixing delays decaying process. **a.** Electronic configuration of S$_1$ and S$_2$ states of Rh. **b**. Schematic representation of the PES of S$_0$ (in blue), S$_1$ (in gray) and S$_2$ (in black) of the fast-decaying subpopulation (left) and slow-decaying subpopulation (right).

To prove our hypothesis, we re-evaluated the energy of the first 50 fs of each trajectory for both subpopulations. As shown in Figure 5.7a, after 10 fs the S_1 and S_2 PES rapidly separate in the fast-decaying subpopulation while the slow-decaying subpopulation enters into a region where S_1 and S_2 are almost degenerate. Since the S_1/S_2 mixing is independent of the initial α and δ_{op} values and velocities, we hypothesize that the factor controlling the S_1-S_2 gap is the difference in the protein environment. To provide support for such a hypothesis, we recomputed the trajectories of both subpopulations using the same initial conditions but reducing the MM protein point charges to a half of their original value. With such reduced electrostatics and although the S_1 and S_2 states of the slow-decaying subpopulation still lie close to each other, they become more separated with respect to the ones experiencing the full protein charge (see Figure 5.7b). Also, we observed that both the fast- and slow-decaying subpopulation decay within 110 fs due to a significantly reduced α bifurcation (see Figure S5.2). Therefore, we conclude that the difference in the electrostatic field from the protein environment promotes the S_1/S_2 mixing behavior.

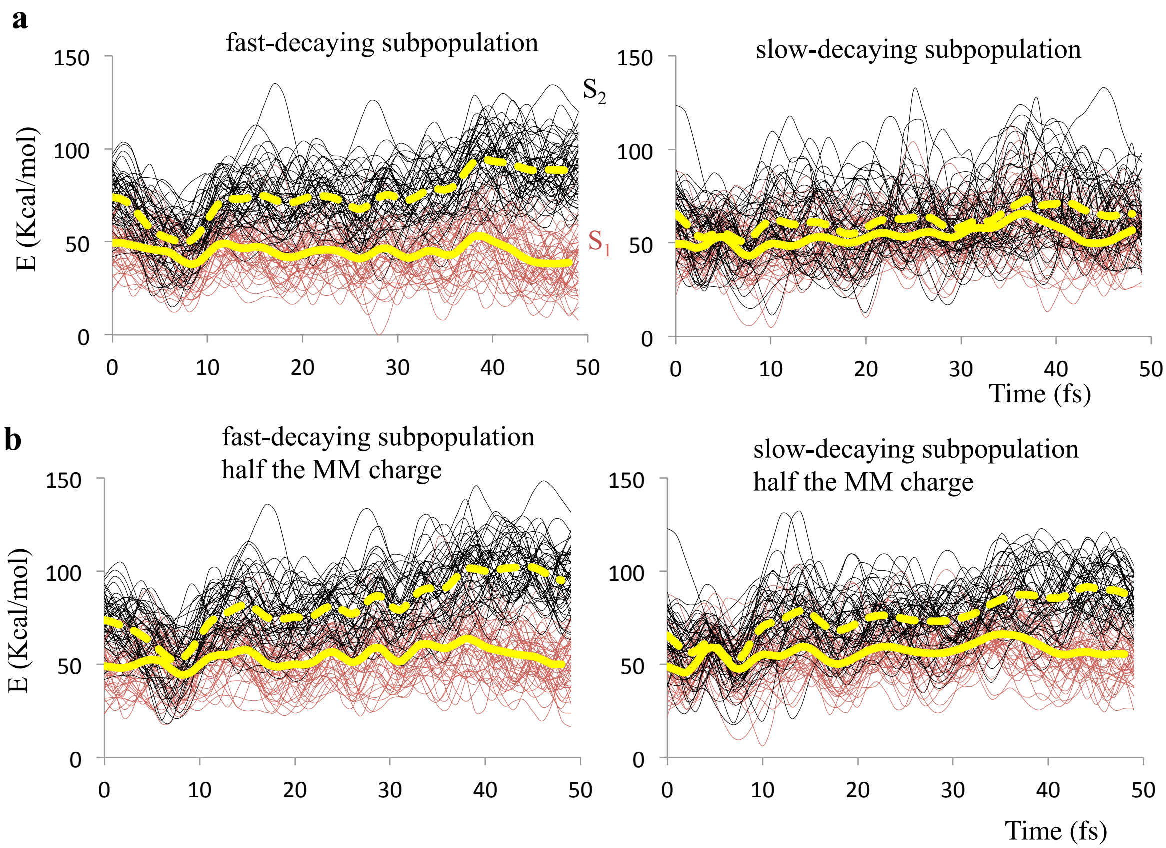

Figure 5.7 Time evolution of energy along S_1 and S_2 state for initial 50 fs of the dynamics. **a.** The energy of S_1 (brown) and S_2 (black) states of fast-decaying subpopulation (left) and slow-decaying subpopulation. Solid and dashed yellow curve indicates average energy of S_1 and S_2, respectively **b**. Same type of plots for trajectories re-calculated with half the MM charge.

5.5 Conclusion

For the first time, we report a simulation of the excited state dynamics of a Rh population. The 200 excited state trajectories extracted from a computed Boltzmann-like distribution at room temperature provided a computed quantum yield (0.68) and S_1 lifetime (98 fs) consistent with the experimental observations. The analysis of our simulated results indicate how the vibrational coherence of the atomic motion occurring during the reaction impacts the efficiency of light-induced photoisomerization through a “splitting-then-decaying” mechanism. Based on such mechanism the protein environment introduces state mixing between the ionic S_1 and diradical S_2, resulting in decoherence of the initially coherent α mode, thus splitting the whole excited state population into subpopulations featuring various decay time. Such splitting enables the quantum yield of each subpopulation to be maximized by modulating the relative phasing of α and δ_{op} modes of its trajectories at the decay point, ultimately leading to a maximization of the quantum yield obtained from the entire Rh population.

5.6 References

(1) Mathies, R. A. *Nat. Chem.* **2015**, *7* (12), 945–947.

(2) Johnson, P. J. M.; Halpin, A.; Morizumi, T.; Prokhorenko, V. I.; Ernst, O. P.; Miller, R. J. D. *Nat. Chem.* **2015**, *7* (12), 980–986.

(3) Schnedermann, C.; Yang, X.; Liebel, M.; Spillane, K. M.; Lugtenburg, J.; Fernández, I.; Valentini, A.; Schapiro, I.; Olivucci, M.; Kukura, P.; et al. *Nat. Chem.* **2018**, *10* (4), 449–455.

(4) Schapiro, I.; Ryazantsev, M. N.; Frutos, L. M.; Ferré, N.; Lindh, R.; Olivucci, M. *J. Am. Chem. Soc.* **2011**, *133* (10), 3354–3364.

(5) Eyring, G.; Curry, B.; Broek, A.; Lugtenburg, J.; Mathies, R. *Biochemistry* **1982**, *21* (2), 384–393.

(6) Johnson, P. J. M.; Farag, M. H.; Halpin, A.; Morizumi, T.; Prokhorenko, V. I.; Knoester, J.; Jansen, T. L. C.; Ernst, O. P.; Miller, R. J. D. *J Phys Chem B* **2017**, *121* (16), 4040–4047.

(7) Okada, T.; Sugihara, M.; Bondar, A.-N.; Elstner, M.; Entel, P.; Buss, V. *J. Mol. Biol.* **2004**, *342* (2), 571–583.

(8) Melaccio, F.; Olivucci, M.; Lindh, R.; Ferré, N. *Int. J. Quantum Chem.* **2011**, *111* (13), 3339–3346.

(9) Kandori, H.; Shichida, Y.; Yoshizawa, T. *Biochem.* **2001**, *66* (11), 1197–1209.

(10) Garavelli, M.; Celani, P.; Bernardi, F.; Robb, M. A.; Olivucci, M. *J. Am. Chem. Soc.* **1997**, *119* (29), 6891–6901.

(11) Schapiro, I.; Weingart, O.; Buss, V. *J. Am. Chem. Soc.* **2009**, *131* (1), 16–17.

(12) Warshel, A. *Nature* **1976**, *260* (5553), 679–683.

(13) Frutos, L. M.; Andruniow, T.; Santoro, F.; Ferre, N.; Olivucci, M. *Proc. Natl. Acad. Sci.*

2007, *104* (19), 7764–7769.

(14) Tully, J. C. *J. Chem. Phys.* **1990**, *93* (2), 1061–1071.

(15) Dartnall, H. J. A. *Vision Res.* **1968**, *8* (4), 339–358.

(16) Manathunga, M.; Yang, X.; Orozco-Gonzalez, Y.; Olivucci, M. *J. Phys. Chem. Lett.* **2017**, *8* (20), 5222–5227.

(17) Manathunga, M.; Yang, X.; Olivucci, M. *J. Phys. Chem. Lett.* **2018**, *9* (21), 6350–6355.

(18) Luk, H. L.; Melaccio, F.; Rinaldi, S.; Gozem, S.; Olivucci, M. *Proc. Natl. Acad. Sci.* **2015**, *112* (50), 15297–15302.

(19) Luk, H. L.; Melaccio, F.; Rinaldi, S.; Gozem, S.; Olivucci, M. *Proc. Natl. Acad. Sci.* **2015**, *112* (50), 15297–15302.

5.7 Supplementary figures

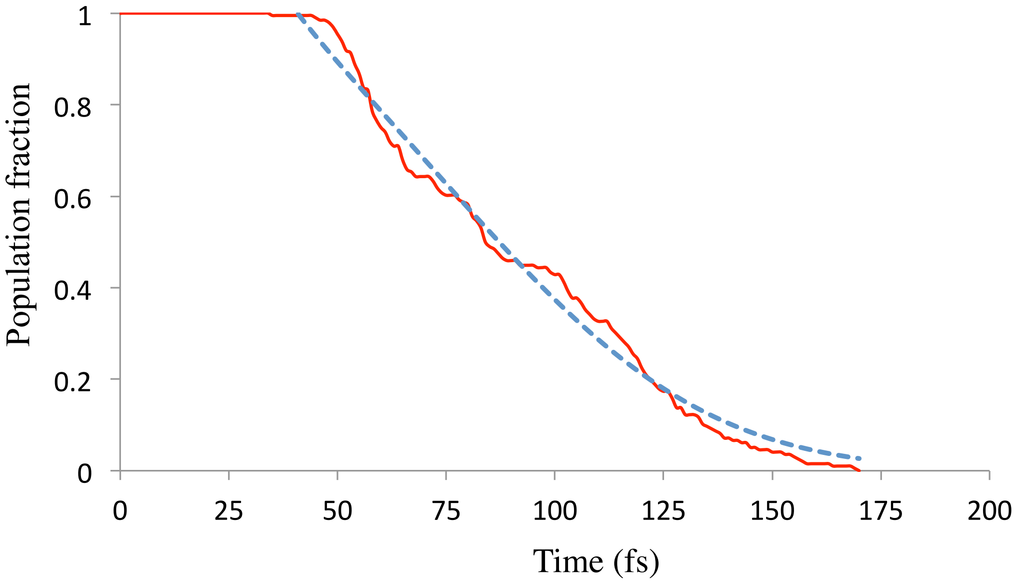

Figure S5.1 Excited state lifetime fitting. Fitting is based on equation 3.1, the population decay is in solid red line and the fitting function is in dashed blue line.

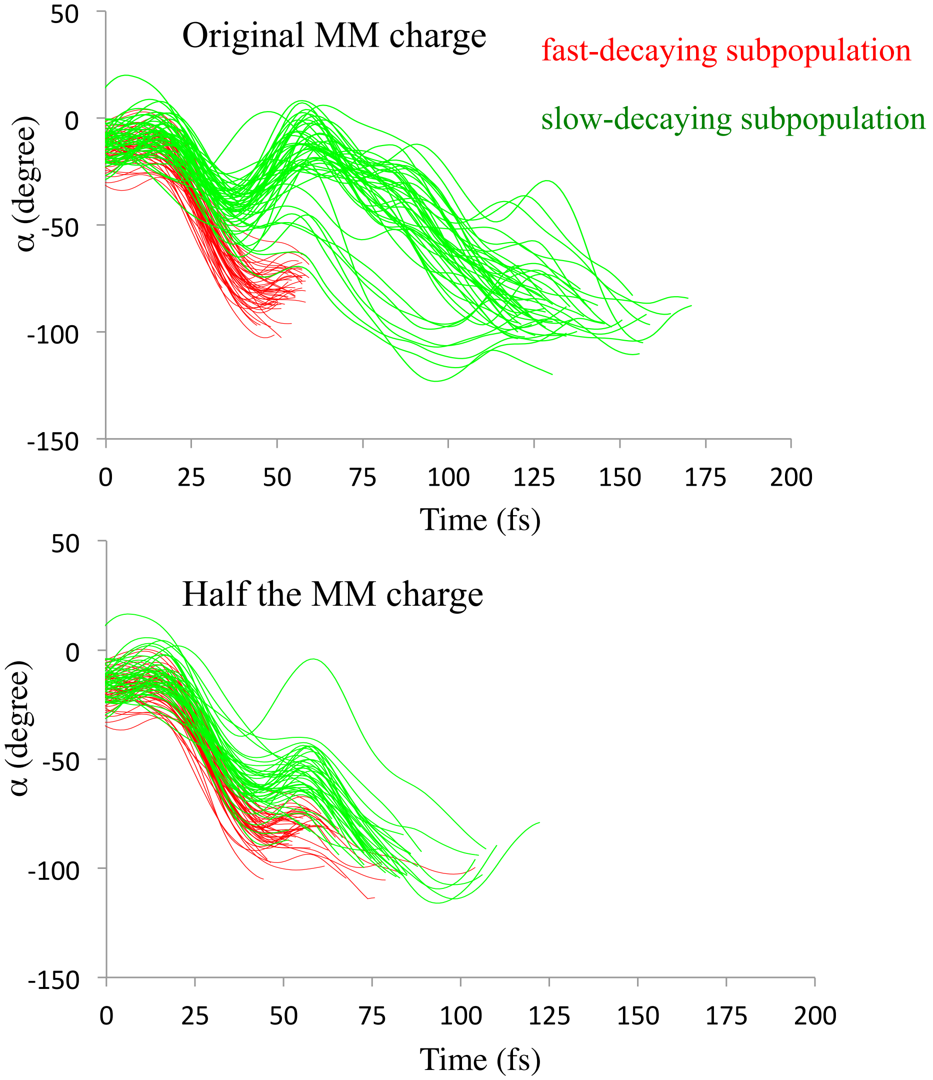

Figure S5.2 Comparison of α motion between trajectories calculated with original MM charge and half the MM charge. The time evolution of α motion is in red for fast-decaying subpopulation and in green for slow-decaying subpopulation.

CONCLUSION AND PERSPECTIVE

In this Dissertation, I provide theoretical and computational evidence supporting a mechanism where vibrational coherence is important for achieving an efficient photoisomerization (i.e. for displaying high quantum yield) in the biological photoreceptor Rh, the vertebrate visual pigment. Such conclusion is reached after the analysis of the results of a novel population dynamics simulation that has been performed with the protocol benchmarked in Chapter III and employing an ASR QM/MM model featuring an abridged retinal chromophore. This protocol is shown to be capable of reproducing the trends in spectroscopy and excited state kinetics seen in the corresponding experimental data. On the other hand, in Chapter IV and V we show that population dynamics simulations provide an effective tool for investigating the impacts of vibrational coherence on the dynamics of an entire excited state population of Rh.

Our calculation indicates a correlation between the Rh photoisomerization outcome, the degree of consistency with a α/δ_{op} phase relationship at the S_1/S_0 CI (or decay point) and the splitting of the original compact excited state population in different subpopulations moving with distinct dynamics. More specifically, at the decay point an out-of-phase δ_{op} motion, with respect to the counterclockwise α reactive motion, promotes the all-*trans* photoproduct formation while the reconsititution of the 11-*cis* reactant occurs if δ_{op} display an in-phase motion. The quantum yield of a Rh population is thus equivalent to the fraction of excited state molecules decaying to S_0 with a proper α/δ_{op} phase. Such correlation is evidenced by an isotopic effect observed by our collaborators who demonstrated experimentally that the Rh quantum yield is sensitive to the deuterium substitution in the chromophore $HC_{11}=C_{12}H$ moiety. Indeed, as explained in Chapter IV, such sensitivity is easily interpreted as the change of the δ_{op} frequency introduced by the hevier deuterium atoms thus changing the δ_{op} phase at the S_1/S_0 CI.

In Chapter V, we report the details of a possible “splitting-then-decaying” mechanism that would maximize the Rh photoisomerization quantum yield and therefore, its light sensitivity. Our calculation indicates an “organized” decoherence process along the α mode occurring 20 to 30 fs after light absorption. Such process, which we demonstrated to be modulated by the protein environment (in particular by the electrostatic field imposed on the chromophore), introduces various degrees of electronic coupling between the reactive S_1 state and the higher and unreactive S_2 state. Such variable coupling is capable to splits the initially coherent excited state population into subpopulations that approach the S_1/S_0 CI at different times. As the quantum yield of each subpopulation is controlled by the corresponding α/δ_{op} phase relationship at the decay point, the splitting-then-decaying mechanism would maximize the quantum yield by getting each subpopulation to decay when the desired out-of-phase δ_{op} motion, which remains always coherent, occurs.

In summary, my Dissertation provides, for the first time, a rather complete mechanistic view of how vibrationally coherence would impact the excited state kinetics and quantum yield of light-induced Rh photoisomerization. The fact that the protein environment of Rh modulates its photoisomerization efficiency implies a possible connection between the loss of light sensitivity and Rh mutations. Indeed, the work presented in this dissertation could help understanding the mechanism of certain retinal diseases associated with Rh mutations, such as *Retinitis Pigmentosa*. Furthermore, the population dynamics simulation protocol documented in this Dissertation provides an effective approach for investigating and predicting the photochemical properties of rhodopsins in general, specifically for the cases in which the experimental approach is not available due to the difficulties in extraction or purification of the protein.

LIST OF ACRONYMS

ARM	Automatic rhodopsin modeling
ASR	Anabaena sensory rhodopsin
BLA	Bond length alternation
BOA	Born-Oppenheimer approximation
CASPT2	Second order multiconfigurational perturbation theory
CASSCF	Complete active space self-consistent field
CI	Conical intersection
ESPF	Electrostatic potential fitted
FC	Franck Condon
FCI	Full configuration interaction
HF	Hartree-Fock
HOOP	Hydrogen-out-of-plane
MD	Dynamics simulation
Meta II	Metarhodopsin II
PES	Potential energy surface
QM/MM	Quantum mechanics/molecular mechanics
Rh	Bovine rhodopsin
TS	Transition state
bathoRh	Bathorodopsin
photoRh	Photorhodopsin
rPSB	Retinal protonated Schiff base
rPBS11	Retinal protonated Schiff base 11-*cis*

rPSBAT	Retinal protonated Schiff base all-*trans*